Universidad Carlos III de Madrid

Universidad Carlos III de Madrid
School of Engineering

Doctoral Thesis

Advanced capabilities for planar X-ray systems

Author: Claudia de Molina Gómez
Advisors: Mónica Abella García
Manuel Desco Menéndez

Doctoral Program on Mathematical Engineering

Department of Bioengineering and Aerospace Engineering

Leganés, July 2018

Universidad Carlos III de Madrid
Escuela Politécnica Superior

Tesis Doctoral

Capacidades avanzadas para sistemas de imagen plana por rayos X

Autor: Claudia de Molina Gómez
Directores: Mónica Abella García
Manuel Desco Menéndez

Programa de doctorado en Ingeniería Matemática
Departamento de Bioingeniería e Ingeniería Aerospacial
Leganés, Julio 2018

TESIS DOCTORAL

Advanced capabilities for planar X-ray systems

AUTOR:	**Claudia de Molina Gómez**
DIRECTORES:	**Mónica Abella García**
	Manuel Desco Menéndez

TRIBUNAL CALIFICADOR

PRESIDENTE:

VOCAL:

SECRETARIO:

CALIFICACION:

Leganés, a de de 2018

"Individually, changes may be considered of little significance. Nonetheless, the accumulation of many small changes can make the world different." M.C.

Agradecimientos

Es muy díficil expresar todo lo afortunada y agradecida que me siento, creo que podría escribir otra tesis entera pero intentaré ser breve y disculpadme si me olvido de alguien.

Esta tesis es tanto mía como de todos los que han participado activamente, de todos los que me han enseñado tantísimas cosas, así como de todos los que me han apoyado, hecho reír y levantado cuando no era capaz de salir de mi propio agujero.

Por supuesto, en primer lugar, quiero agradecer a mi directora de tesis, Mónica, que ha confiado en mí todo este tiempo y ayudado infinitamente en esta tesis. Gracias por contagiarme tu tesón por hacer las cosas bien y tu pasión tanto por la docencia como por la investigación.

Gracias también a mi director de tesis, Manuel Desco, por sus consejos y por darme la oportunidad de trabajar en un grupo del que siempre estaré orgullosa.

Gracias a Juan Abascal, porque sin tí esta tesis no hubiera sido posible. Por tus grandes lecciones de compressed sensing y body weight! Eres un grande. Merci!

Gracias a los informáticos, Javi y Estefanía, siempre dispuestos a hacer cosas nuevas, porque sin vosotros esta tesis no hubiese sido posible, moláis mucho.

Thanks a lot to Adam Alessio, for beeing so understanding, kind and for giving me the opportunity of working with you and your group.

Gracias a todas las generaciones del equipo CT! Sin duda no voy a encontrar unos compañeros mejores que vosotros, esta tesis es también vuestra. Gracias a mi Pili Inés, mi principal apoyo todo este tiempo, a Alba, con su eterna sonrisa y ganas, a Alvarito, que lo mismo te programa una interfaz que te pide un chupito ;), Ramón, gran corazón, Cristóbal, q me ha ayudado tanto como vacilado así que imaginaos!, apoyo importantísimo para lograr acabar, siempre nos quedará el bim jardening!, Nere, gran amiga y apoyo en este final de etapa, Xiaolin, mucho más que una estudiante de TFG, gracias a Laura, Suzanne, Miguel, Nik, ...

A mis actuales compis que agradan el día a día: Sandrita, Yolanda, María, Tra, Rolín, Esther, Jorge, Marta, Diego, Dani, Marivi, Marisa, Lorena, Elena, Bea, Gorka, Isa, Azucena, etc.

A Luis y Carmencita, a los que tanto echo de menos.

A los exLIMeros, q son muchos pero todos y cada uno han dejado su huella en mí, a la banda buffer (Carlos, Juanjo pequeño, Martín y Aurora), Paula, Álex, Elena, Santi, María, Marco, Mikael, Laura, Ángela y un eterno etc. Con mención especial a las champiñonas, Aurora, encantadora, Vero, única e irrepetible, con la que espero alcanzar muchas más cimas!, Inés, que tanto cariño y sensatez me aporta, Judit, buenísima persona, Elia, fiel y buena amiga.

A los jefes mudados a la UC3M que también me han enseñado mucho, y a mis compis que amenizan mis días allí. Gracias!

Gracias a todo el equipo "Late call", esa gran familia que se ha formado de gente tan guay (mi vecino Mario, María, Deivid, Bego, Joaquín, Moni, Rafa, Rocío, Lanillos, Suzanne, Marina, Blanca, Ana R, Ana V, Nico).

A mis amigos de fuera del curro que afortunadamente son muchos, Lara, fiel amiga, Xiana, mi compi de planes differentes, Raúl y Cristian, compis de locurillas, a mis nenas (Lau, Isa, Sas, Ajito, Ana, Laurita, Mery y Silvia), a mis compis de monte (Patri, Palma, Víctor, Subhra, Errea), a los intrépidos vecinos, a Bea, Valle, Juani, Laura, etc.

Al equipo EA, esos desconocidos que se volvieron amigos para siempre después de esa aventura en Vancouver que comenzó con una buena tortilla... En especial al comite anti-crisis (Marta, Ashley y Paula).

A Gauss, por su cariño incondicional y compañia.

A toda mi gran familia y en especial a mis padres, por su infinita paciencia conmigo, por cuidarme tanto siempre, mil gracias. A mi hermano Dani, con el que da gusto hablar de frikadas varias y siempre quiso entender a qué se dedicaba su hermana pequeña, a mi hermano Mario, ejemplo de sensatez, por cuidarme siempre y descubrirme el LIM, y a Laura, por su cariño desde el primer día.

A Juan, por su cariño, por sus marmitakos sanadores y por cuidarme tantísimo. Ahora comienza otra aventura juntos ;)

Abstract

The past decades have seen a rapid evolution towards the use of digital detectors in radiology and a more flexible robotized movement of the system components, X-ray tube and detector. This evolution opened the possibility for incorporating advanced capabilities in these planar X-ray systems, and for providing new valuable diagnostic information compared to the previous technology. Some of the current challenges for radiography are to obtain more quantitative images and to reduce the inherent superposition of tissues because of the 2D nature of the technique.

Dual energy radiography, based on the acquisition of two images at different source voltages, enables a separate characterization of soft tissue and bone structures. Its benefits over conventional radiography have been proven in different applications, since it improves information content without adding significant extra acquisition time or radiation dose.

In a different direction, a really disruptive advance would be to obtain 3D imaging with systems designed just for planar images. The incorporation of tomographic capabilities into these systems would have to deal with the acquisition of a limited number of projections, with non-standard geometrical configurations.

This thesis presents original contributions in these two directions: dual energy radiography and 3D imaging with X-ray systems designed for planar imaging. The work is framed in a line of research of the Biomedical Imaging and Instrumentation Group from the Bioengineering and Aerospace Department of University Carlos III de Madrid working jointly with the University Hospital Gregorio Marañón, focused on the advance of radiology systems. This research line is carried out in collaboration with the group of Computer Architecture, Communications and Systems (ARCOS), from the same university, the Imaging Research Laboratory (IRL) of the University of Washington and the research center CREATIS, France. The research has a clear focus on technology transfer to the industry through the company Sedecal, a Spanish multinational among the 10 best world companies in the medical imaging field.

The first contribution of this thesis is a complete novel protocol to incorporate dual energy capabilities that enable quantitative planar studies. The proposal is based on the use of a preliminary calibration with a very simple and low-cost phantom formed by two parts that represent soft tissue and bone equivalent materials. This calibration is performed automatically with no strict placement requirements. Compared to current Dual-energy X-ray Absorptiometry (DXA) systems, 1) it provides real mass-thickness values directly, enabling quantitative planar studies instead of relative comparisons, and 2) it is based on an automatic preliminary calibration

without the need of interaction of an experienced technician.

The second contribution is a novel protocol for the incorporation of tomographic capabilities into X-ray systems originally intended for planar imaging. For this purpose, we faced three main challenges.

First, the geometrical trajectory of equipment follows non-standard circular orbits, thus posing severe difficulties for reconstruction. To handle this, the proposed protocol comprises a new geometrical calibration procedure that estimates all the system parameters per-projection.

Second, the reconstruction of a limited number of projections from a reduced angular span leads to severe artifacts when using conventional reconstruction methods. To deal with these limited-view data, the protocol includes a novel advanced reconstruction method that incorporates the surface information of the sample, which can be extracted with a 3D light surface scanner. These data are introduced as an imposed constraint following the Split Bregman formulation. The restriction of the search space by exploiting the surface-based support becomes crucial for a complete recovery of the external contour of the sample and surroundings when the angular span is extremely reduced. The modular, efficient and flexible design followed for its implementation allows for the reconstruction of limited-view data with non-standard trajectories.

Third, the optimization of the acquisition protocols has not yet explored with these systems. This thesis includes a study of the optimum acquisition protocols that allowed us to identify the possibilities and limitations of these planar systems. Using the surface-constrained method, it is possible to reduce the total number of projections up to 33% and the angular span down to 60 degrees.

The contributions of this thesis open the way to provide depth and quantitative information very valuable for the improvement of radiological diagnosis. This could impact considerably the clinical practice, where conventional radiology is still the imaging modality most used, accounting for 80-90% of the total medical imaging exams. These advances open the possibility of new clinical applications in scenarios where 1) the reduction of the radiation dose is key, such as lung cancer screening or Pediatrics, according to the ALARA criteria (As Low As Reasonably Achievable), 2) a CT system is not usable due to movement limitations, such as during surgery or in an ICU and 3) where costs issues complicate the availability of CT systems, such as rural areas or underdeveloped countries.

The results of this thesis has a clear application in the industry, since it is part of a proof of concept of the new generation of planar X-ray systems that will be commercialized worldwide by the company SEDECAL (Madrid, Spain).

Resumen

Los últimos años están viendo un rápido avance de los sistemas de radiología hacia el uso de detectores digitales y a una mayor flexibilidad de movimientos de los principales componentes del sistema, el tubo de rayos X y el detector. Esta evolución abre la posibilidad de incorporar capacidades avanzadas en sistemas de imagen plana por rayos X proporcionando nueva información valiosa para el diagnóstico. Dos retos en radiografía son obtener imágenes cuantitativas y reducir la superposición de tejidos debida a la naturaleza proyectiva de la técnica.

La radiografía de energía dual, basada en la adquisición de dos imágenes a diferente kilovoltaje, permite obtener imágenes de tejido blando y hueso por separado. Los beneficios de esta técnica que aumenta la cantidad de información sin añadir un tiempo de adquisición o de dosis de radiación extra significativos frente al uso de radiografía convencional, han sido demostrados en diferentes aplicaciones.

En otra dirección, un avance realmente disruptivo sería la obtención de imagen 3D con sistemas diseñados únicamente para imagen plana. La incorporación de capacidades tomográficas en estos sistemas tendría que lidiar con la adquisición de un número limitado de proyecciones siguiendo trayectorias no estándar.

Esta tesis presenta contribuciones originales en esas dos direcciones: radiografía de energía dual e imagen 3D con sistemas de rayos X diseñados para imagen plana. El trabajo se encuadra en una línea de investigación del grupo de Imagen Biomédica e Instrumentación del Departamento de Bioingeniería e Ingeniería Aerospacial de la Universidad Carlos III de Madrid junto con el Hospital Universitario Gregorio Marañon, centrada en el avance de sistemas de radiología. Esta línea de investigación se desarollada en colaboración con el grupo *Computer Architecture, Communications and Systems* (ARCOS), de la misma universidad, el grupo *Imaging Research Laboratory* (IRL) de la Universidad de Washington y el centro de investigación CREATIS, de Francia. Se trata de una línea de investigación con un claro enfoque de transferencia tecnológica a la industria a través de la compañía SEDECAL, una multinacional española de entre las 10 líderes del mundo en el campo de la radiología.

La primera contribución de esta tesis es un protocolo completo para incorporar capacidades de energía dual que permitan estudios cuantitativos de imagen plana. La propuesta se basa en una calibración previa con un maniquí simple y de bajo coste formado por dos materiales equivalentes de tejido blando y hueso respectivamente. Comparado con los sistemas actuales DXA (*Dual-energy X-ray Absorptiometry*), 1) proporciona valores reales de tejido atravesado, 2) se basa en una calibración automática que no requiere la interacción de un técnico con gran experiencia.

La segunda contribución es un protocolo nuevo para la incorporación de capacidades tomográficas en sistemas de rayos X originariamente diseñados para imagen plana. Para ello, nos enfrentamos a tres principales dificultades.

En primer lugar, las trayectorias que pueden seguir la fuente y el detector en estos sistemas no constituyen órbitas circulares estándares, lo que plantea retos importantes en la caracterización geométrica. Para solventarlo, el protocolo propuesto incluye una calibración geométrica que estima todos los parámetros geométricos del sistema para cada proyección.

En segundo lugar, la reconstrucción de un número limitado de proyecciones adquiridas en un rango angular reducido da lugar a artefactos graves cuando se reconstruye con algoritmos convencionales. Para lidiar con estos datos de ángulo limitado, el protocolo incluye un nuevo método avanzado de reconstrucción que incorpora la información de superficie de la muestra, que se puede se obtener con un escáner 3D. Esta información se impone como una restricción siguiendo la formulación de Split Bregman, para compensar la falta de datos. La restricción del espacio de búsqueda a través de la explotación del soporte basado en superficie, es crucial para una recuperación completa del contorno externo de la muestra cuando el rango angular es extremadamente pequeño. El diseño modular, eficiente y flexible de la implementación propuesta permite reconstruir datos de ángulo limitado obtenidos con posiciones de fuente y detector no estándar.

En tercer lugar, hasta la fecha, no se ha explorado la optimización del protocolo de adquisición con estos sistemas. Esta tesis incluye un estudio de los protocolos óptimos de adquisición que permitió identificar las posibilidades y limitaciones de estos sistemas de imagen plana. Gracias al método de reconstrucción basado en superficie, es posible reducir el número total de proyecciones hasta el 33% y el rango angular hasta 60 grados.

Las contribuciones de esta tesis abren la posibilidad de proporcionar información de profundidad y cuantitativa muy valiosa para la mejora del diagnóstico radiológico. Esto podría impactar considerablemente en la práctica clínica, donde la radiología convencional es todavía la modalidad de imagen más utilizada, abarcando el 80-90% del total de los exámenes de imagen médica. Estos avances abren la posibilidad de nuevas aplicaciones clínicas en escenarios donde 1) la reducción de la dosis de radiación es clave, como en *screening* de cáncer de pulmón, de acuerdo con el criterio ALARA (*As Low As Reasonably Achievable*), 2) no se puede usar un sistema TAC por limitaciones de movimiento como en cirugía o UCI, o 3) el coste limita la disponibilidad de sistemas TAC, como en zonas rurales o en países subdesarrollados.

Los resultados de esta tesis presentan una clara aplicación industrial, ya que son parte de un prototipo de la nueva generación de sistemas planos de rayos X que serán distribuidos mundialmente por la compañía SEDECAL.

Contents

List of Figures

List of Algorithms

Chapter 1

Introduction

Diagnostic imaging is a widely spread discipline in the medical world. It represents the spatial distribution of one or more physical or chemical properties inside the human body, which facilitates the detection of any anomalies in the clinical picture of a patient. Techniques used in diagnostic imaging, also known as image modalities, are characterized by radiating the patient with some kind of energy. Depending on the symptoms presented, as well as the body part to be treated, doctors may apply one modality or another. Among them stand out the radiology (X-rays), nuclear medicine (γ-rays), magnetic resonance imaging (radio waves), echography (ultrasound) and endoscopy (light).

Radiology is the most used medical imaging modality worldwide. It has numerous advantages such as low cost and speed. This modality employs X-ray energy, which was discovered in 1895 by the German physician Wilhelm Conrad Rontgen who would receive the Physics Nobel Prize a few years after.

The main imaging techniques which apply to this modality are the conventional radiology, the digital radiology, and the computed tomography (CT). All these techniques are ionizing as they use X-rays energy. The X-rays induce chemical reactions over the patient due to the high energy that is being irradiated and which leads to the ionization of diverse molecules. Likewise, spatial high-resolution images are obtained, and detailed information about the anatomy of the subject is extracted according to the density of the tissue traversed by the rays.

Conventional radiology is the technique by which a projective image is obtained when exposing a photographic film to radiation with high energy levels (Fig. 1.1). The film captures the photons radiated by the X-ray source which were neither absorbed nor scattered by the patient, who is placed between the source and the photographic film. These images are said to be projective as each pixel represents the integral of the physical properties of an object along a ray being projected onto a screen.

Digital radiology is very similar to the conventional one. Its working mechanism differs only in the utilization of a digital detector instead of the film screen, which it is more sensitive and allows the reduction of the ionizing radiation dose to the patient. On the other hand, and thanks to the image digitalization, it is possible to recover certain valid information by applying image processing even when the performing conditions of the scan were not the optimal ones. Scan repetitions may be avoided when applying this technique.

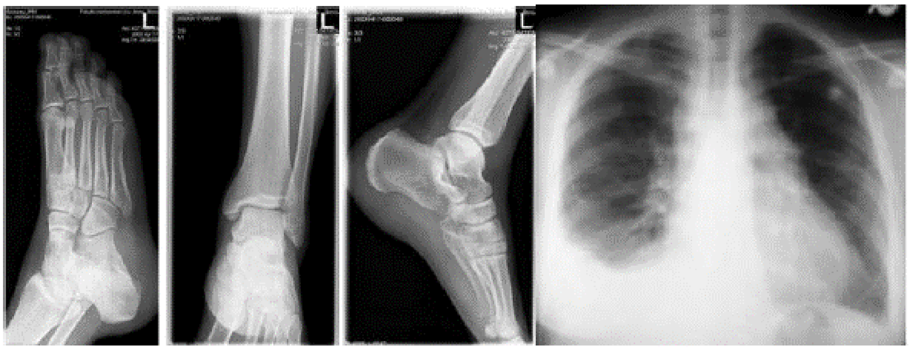

Figure 1.1: *Human radiological studies. Source: [Jan, 2005].*

Computed tomography (CT), unlike its two predecessors, is able to separate each of the different planes of the sample (Fig. 1.2), and to represent them into a two-dimensional image. Tomographic slices facilitate the visualization of a body section and its interpretation without interferences from other regions. It is possible to measure the attenuation characteristics of a sample by transmitting a collection of X-ray photons through the sample along different trajectories.

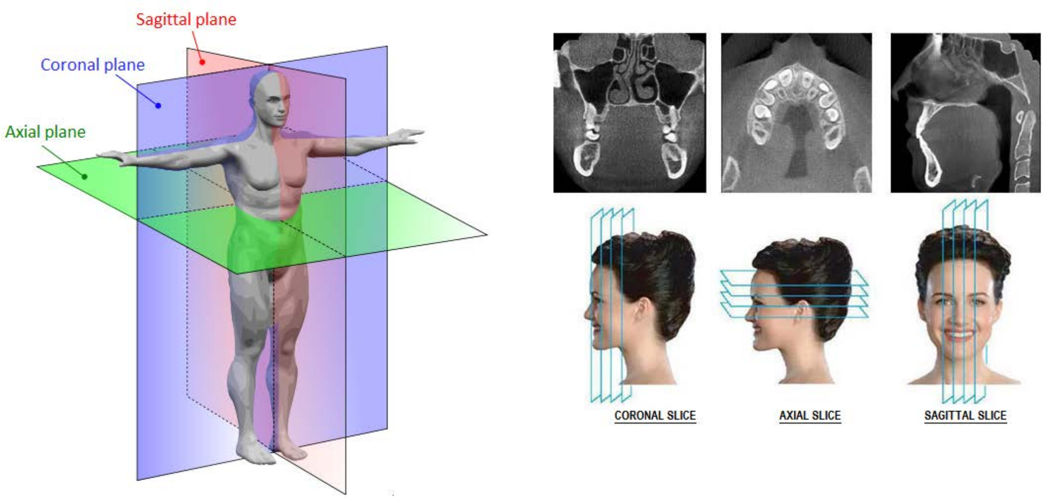

Figure 1.2: *Representation of the three planes formed by tomographic slices (left), and coronal, axial and sagittal slices from a maxillofacial CT (right).*

1.1 Generation of X-rays

X-ray radiation was discovered by chance in November 1895 by Wilhelm C. Rontgen while working with a cathode ray tube. Rontgen saw that this radiation was capable of going through certain materials but not without suffering some attenuation and that it could be captured on a photographic plate similarly to light. These characteristics allowed X-rays to be utilised in medicine: the first Rontgen image was made soon after the discovery of X-rays and, a few months later, radiographs were commonplace in clinical practice.

The nature of X-rays was described by Max von Laue in 1912. X-rays are a form of electromagnetic radiation. As such, they are composed of photons whose energy E is determined by their frequency f and wavelength λ:

$$E = \frac{hc}{\lambda} = h\mu \tag{1.1}$$

where h is Planck constant $(4.135 \cdot 10^{-15} eV \cdot s)$ and c is the speed of light. X-ray energy ranges from $5 \cdot 10^4$ to $10^6 eV$, which places X-ray radiation between ultraviolet radiation and γ rays in the electromagnetic spectrum (Fig. 1.3). In medical imaging, X-ray photons usually have an energy between 10 keV and 150 keV. X-rays with energies between 10 eV and 30 keV, referred to as soft, are used in microscopy.

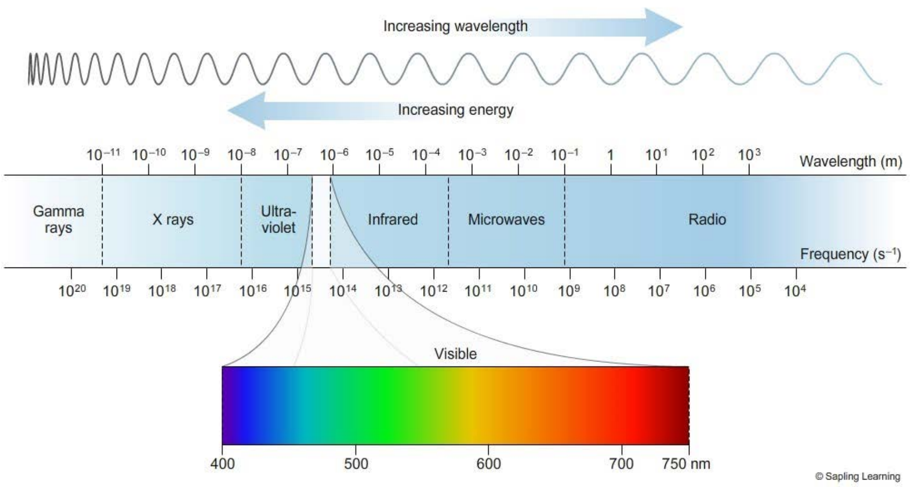

Figure 1.3: *Electromagnetic spectrum. Source: Sapling learning .*

X-rays are produced in a vacuum tube with a cathode and an anode, known as an X-ray tube (Fig. 1.4). An electric current is made to flow through a filament in the cathode causing electrons to be released through thermal excitation. A high voltage applied between the cathode and the anode accelerates the electrons toward the anode. Accelerated electrons hit the metal target (usually tungsten) in the anode, losing their energy mainly as heat and around 4% as X-ray photons.

When electrons impact on the anode, X-ray photons can be produced by two different processes (Fig. 1.5):

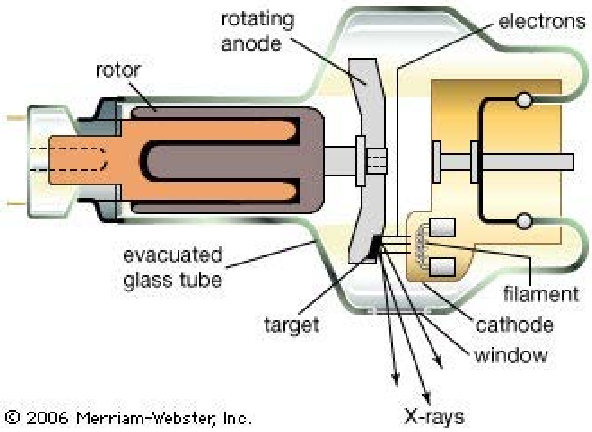

Figure 1.4: *Sketch of an X-ray tube. Source: Radiography enclclyclopedia.*

- Bremsstrahlung or braking radiation: it is produced when an electron passes close to an atom nucleus. Due to the positive charge of the nucleus, the incident electron changes its trajectory and slows down emitting part of its kinetic energy as an X-ray photon. This process yields a continuous X-ray spectrum. The number of photons obtained is inversely proportional to their energy.

- Characteristic radiation: this radiation is produced when an electron ionizes one of the atoms in the target material, extracting one electron from an inner layer (i.e. layer K). To fill the vacancy left by the extracted electron, an electron from an outer layer jumps to the inner one releasing part of its energy as an X-ray photon. The energy of this photon is equal to the energy difference between these two layers. Therefore, this process produces peaks in the X-ray spectrum.

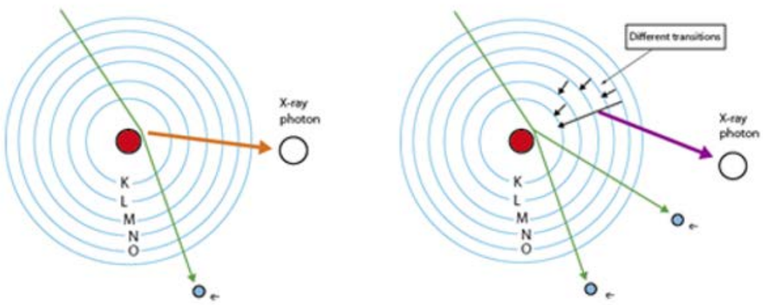

Figure 1.5: *Sketch of the processes involved in X-ray generation: (left) Bremsstrahlung and (right) characteristic radiation. Source: [Abella, 2010]*

Low energy photons produced are absorbed within the X-ray tube, affecting the spectral distribution at low energies. The X-ray emission spectrum is displayed in Fig. 1.6.

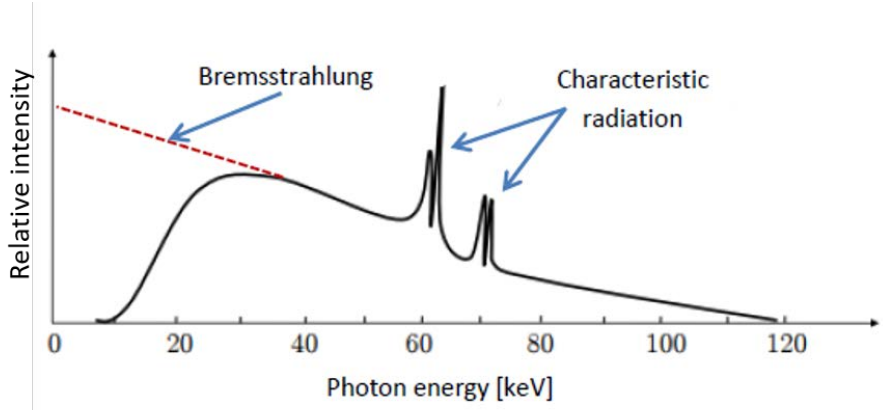

Figure 1.6: *Characteristic form of the X-ray emission spectrum due to the typical phenomena that occur in the Xray tube. Source: [Molina Gómez et al., 2012].*

The cathode current and the time (mAs) determine the amount of electrons shot at the anode and, consequently, the amount of photons produced. The voltage applied between the cathode and the anode (kVp). It determines the energy of the electrons when hitting the anode and, consequently, the energy of the emitted photons.

1.2 X-ray interaction with matter

X-ray photons can interact with soft tissue in three different ways due to the energy range used in diagnostic imaging (10 to 150 keV), as shown in Fig. 1.8. These interactions are: Rayleigh scattering, Compton scattering and photoelectric absorption (Fig. 1.7).

- Rayleigh or coherent scattering: a photon is absorbed by an atom and immediately released in the form of a new photon with the same energy but travelling in a slightly different direction. It occurs mainly at low energies ($< 30\ keV$).
- Photoelectric effect: an X-ray photon is absorbed, yielding its energy to an electron, which escapes from its nucleus in the same direction as the incoming photon (ionization).
- Compton scattering: an X-ray photon collides with an electron orbiting the atom, transferring only part of it energy to the electron. The electron is ejected from the atom with a certain kinetic energy, while the photon, now with lower energy, has its direction deviated.

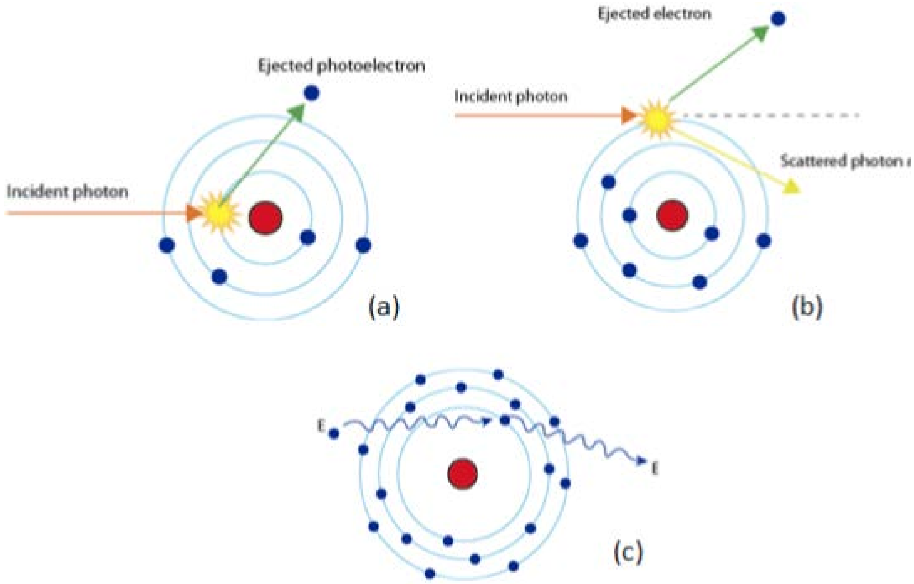

Figure 1.7: *Diagrams of the processes that occur when X-ray photons interact with matter: (a) Photoelectric effect, (b) Compton effect and (c) Rayleigh effect. Source: [Molina Gómez et al., 2012].*

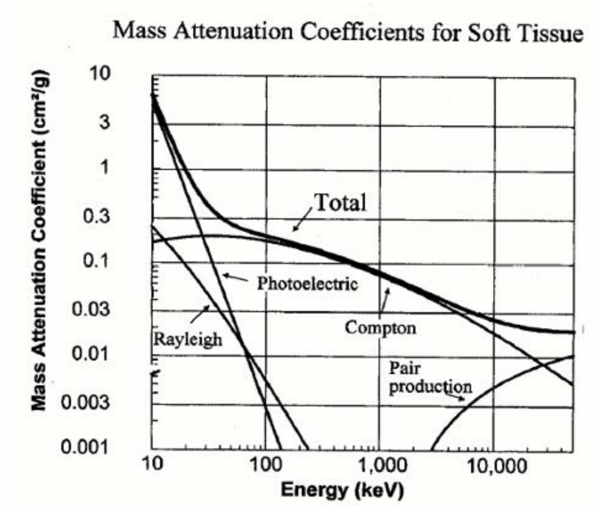

Figure 1.8: *Diagram of the different phenomena produced by the interacting X-ray photons with soft tissue (photoelectric effect, Compton, Rayleigh and pair production) as a function of the energy of these photons. The red box shows the energy range (keV) used in medical imaging where photoelectric effect, Rayleigh and Compton are present. Source: [Bushberg, 2002].*

1.3 Evolution of detection process

Initial X-ray detectors made use of photographic films covered by a silver emulsion. Since the film is more sensitive to light photons than to X-ray photons, high doses were required to obtain an image with a reasonable quality. To overcome this problem, an intensifying screen was placed in contact with the film (Fig. 1.9). X-ray photons would interact with this screen producing light photons which would then be collected by the photographic film thus reducing the amount of dose required to obtain a good quality image.

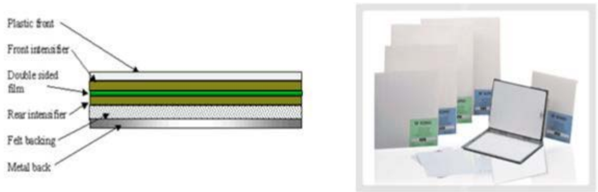

Figure 1.9: *Cross section representation of a film covered on both sides by a fluorescent screen (left). Example of commercial intensifier screen by Soyee Product Inc. (right). Source: [Korner et al., 2007].*

The first digital systems were used in the 1980s. These systems were known as Computed Radiography (CR). The image was generated in two steps. First, the X-ray photons excite electrons in a phosphor crystal layer, temporarily storing the photon energy. This is followed by a reading step: the crystal layer is forced to release the stored energy as light by exciting it with a laser. The produced light is then collected in a photomultiplier array converting it into an analogue signal which is then amplified. Finally, an analogue to digital conversion is performed. This process is summarised in Fig. 1.10.

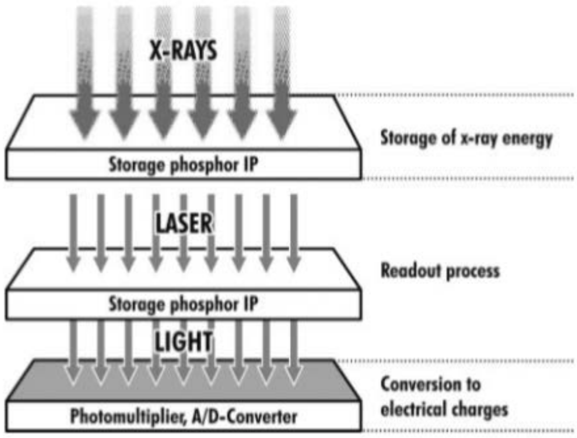

Figure 1.10: *Composition diagram of a CR digital detection system. Source: [Korner et al., 2007] .*

The reading and conversion steps require a separate system. The incorporation of CR systems, however, was really simple as it only needed the replacement of the photographic plate by the new detector panel in the same rack.

In the 1990s, the first Direct Radiography (DR) systems appeared. These systems convert X-ray photons directly into digital signals.

DR systems can be classified as direct or indirect depending on the conversion process followed (Fig. 1.11). Direct conversion systems convert X-ray photons into electric signals in a single step using a photoconductor material. Indirect conversion systems first convert X-ray photons into visible light using a scintillator; these light photons are then converted into electrical signals using a photodiode array.

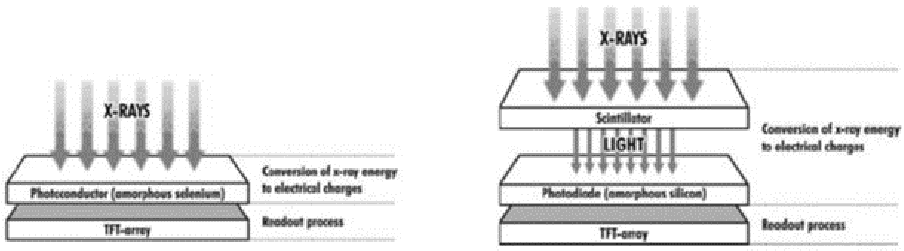

Figure 1.11: *Composition diagram of a direct conversion DR digital detection system (left). Composition diagram of an indirect conversion DR digital detection, flat panel (right). Source: [Korner et al., 2007].*

Flat panel detectors are one of the most common DR systems with indirect conversion. Flat panel detectors present a small size and are lighter and far more durable than other digital detectors.

Other type of X-ray detector is the image intensifier (Fig. 1.12). It is a large image tube that converts a low intensity X-ray image into a visible image. X-rays incident on an image intensifier are transmitted through an aluminum metal input window with high X-ray transmittance and less scattering. They are then absorbed by an input phosphor screen (cesium iodide crystal) and converted into a light image. On the inner surface of the input phosphor screen, a photocathode is formed, where the light image is converted into a photoelectron image. The photoelectron image is then accelerated and focused by an electric lens (electric field) consisting of an input window, focusing electrodes and an anode to collide with an output phosphor screen. The output phosphor screen then, again, converts this photoelectron into a visible light image. Since the photoelectron image is condensed by the electric lens to increase the density of electrons and simultaneously accelerated by a high electric field to collide with the output phosphor screen, the output image is approximately ten thousand times brighter than it would be obtained when the phosphor screen is placed at the input surface position of the X-ray image intensifier. These parts are all mounted in a high vacuum environment within glass or more recently, metal/ceramic.

Once the output image is obtained, viewing of the data was via mirrors and optical systems until the adaptation of television systems in the 1960s. The output can now be captured on a camera using pulsed outputs from an X-ray tube similar to a normal radiographic exposure. CR still requires multiple steps for the technologist, so other approaches have come up. Flat panel detector digital systems (DR) have eliminated cassettes and have reduced the number of steps to perform exams. DR systems use either direct or indirect detector:

- Direct detectors directly covert incoming X-ray photons to an electronic digital

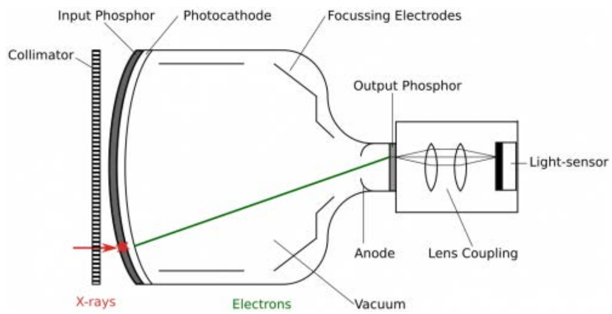

Figure 1.12: *Composition diagram of a CR digital detection system.*

signal.

- In indirect conversion (e.g. flat panel detectors), X-ray photons are first converted into visible light proportionally to the detected photons and then these light photons are converted into electrical charges by a photodiode array.

1.4 Radiology

The complete arrangement of an standard planar X-ray system is shown in Fig. 1.13. Apart from the main components, X-ray source and detector, the conventional X-ray rooms include a primary collimator close to the source, a pre-patient filter, an anti-scatter grid and automatic exposure cameras in some cases. The primary collimator limits the rays focusing them to the area of interest, thus, the surrounding parts are not radiated. A light source is used to help the radiographer center the x-ray beam. Automatic collimators are electronically interlocked with the Bucky tray so the x-ray beam is automatically restricted to the size of the cassette.

The pre-patient filter hardens the beam and absorbs the soft X-rays that are not useful for imaging and only could contribute as more radiation dose.

To reduce the effect of scatter in the images, anti-scatter grids are commonly used. These grids remove about 80-90% of the scatter but increases radiation exposure to the patient by a factor of 2-3×. The grid strips are made of lead and aluminum is used as the inner space material. The grid frequency will range from 24 to 44 lines/cm.

1.4.1 Dual-energy X-ray absorptiometry (DXA)

The Dual-Energy X-Ray Absorptiometry (DXA) technique is based on the acquisition of two radiographies at different source voltages [Bazzocchi et al., 2016]. They are based on the combination of both radiographies to obtain two images with soft tissue and bony structures respectively. Those maps have to be tuned manually by a radiologic technician with high expertise in the protocol.

The first DXA systems were based on a pencil-beam geometry obtained with a highly collimated source and a small detector. The acquisition time with these

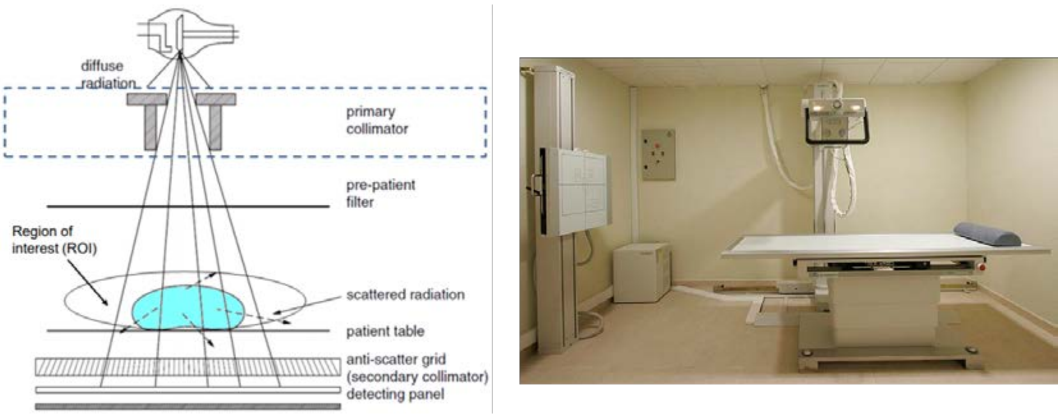

Figure 1.13: *Scheme (left) and picture (right) of a standard radiology system. Source: http : //www.clinicadelrio.com/*

systems was very long, around 30-40 minutes for the whole body [Adams, 2013]. Nowadays, most DXA systems are based on fan beam geometries resulting in a faster acquisition, around 30 seconds and a better image quality [Crabtree et al., 2007]. Fig. 1.14 shows an example of a DXA system and a spine exam.

Figure 1.14: *Lunar iDxa scanner GE (left) and DXA image of the spine (right), source: [Adams, 2013].*

Commonly, the bone mineral content (in gr) and the bone mineral area (in cm^2) are measured [Adams, 2013] and compared through a statistical test with tabulated measurements of a representative population sample differentiated by age and gender. The radiologic technician measures the bone mineral area with a semiautomatic tool based on edges detection. Then, the bone mineral content is given by multiplying the bone area wih the bone mineral density.

In the soft tissue image, the technician measures the fat mass and non-bone lean mass in the pixels with absence of bone. In this process, it is necessary to refine the soft tissue map manually.

Fig. 1.15 shows an example of DXA study of whole body where the different body areas are represented with different colours.

These DXA exams present some limitations: 1) the images are usually based on a weighted subtraction of the low- and high-energy radiographies resulting in non direct quantitative values, 2) soft tissue measurements are affected by the bone parts

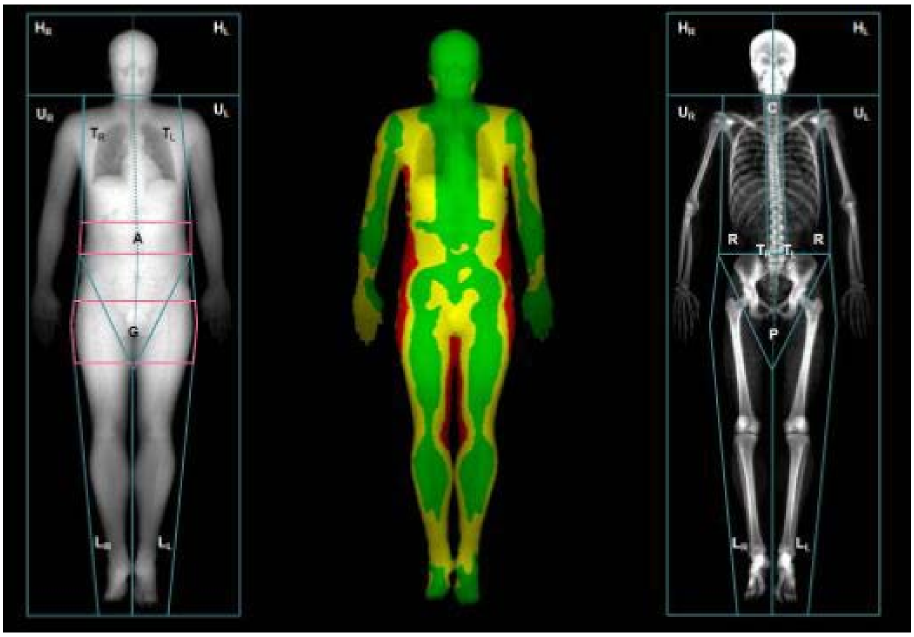

Figure 1.15: *Whole body DXA study with the corresponding soft tissue image (left), the image with different colour depending on the fat content, red, high fat percentage; yellow, medium fat percentage; and green, low fat percentage (center) and the corresponding bone image (right) [Bazzocchi et al., 2016].*

that are not really subtracted, 3) both the images obtained and the edge detection have to bee refined by an expert technician in the protocol.

1.4.2 Fluoroscopy

Fluoroscopy is an imaging modality that provides real-time X-ray images. This technique is especially useful for guiding a variety of diagnostic and interventional procedures. A fluoroscope consists on an X-ray source and a detector. Modern fluoroscopes use an image intensifier or a CCD video camera as a detector, which allows the image to be recorded and visualized in a monitor. The ability of fluoroscopy to display motion is provided by a continuous series of images produced at a maximum rate of 25-30 complete images per second, similar to a normal television rate.

While the X-ray exposure needed to produce one fluoroscopic image is low (compared to radiography), high exposures to patients can result from the large series of images that are encountered in fluoroscopic procedures. Therefore, the total fluoroscopic time is one of the major factors that determine the exposure to the patient from fluoroscopy. Personnel working with fluoroscopy equipment must wear proper protection as being exposed to radiation for long periods of time. As seen in Fig. 1.16, personnel handling fluoroscopy systems wore minimum protection and worked very close to the device. Nowadays controlling is done remote control and protection is safer.

The sensitivity of a fluoroscopic system makes reference to the amount of ex-

Figure 1.16: *Primitive fluoroscopy procedure in which medical personnel use minimum protection (left) and a photograph of us while working with the C-arm with remote control devices and better protections such as thyroid protection collar (right).*

posure required to produce images. This will depend on the characteristics of the detector used. The aim is to obtain good quality images that give the specific information required with the less patient exposure possible.

C-arm systems

A C-arm is a fluoroscopic system comprising two units, an X-ray generator and a detector (image intensifier or flat panel) mounted in an arc-shaped gantry, together with a workstation used to visualize, store, and manipulate the images. Designed to acquire real-time planar images, C-arms have demonstrated to be a useful qualitative assessment tool to guide surgical procedures thanks to their open design, compactness and portability, which allow to set the C-shape around the patient lying in the bed.

The mobile fluoroscopic system is known as C-arm (Fig. 1.17). It consists of two units, the X-ray generator and the detector (image intensifier or flat panel) mounted in an arc-shaped wheeled structure and the workstation unit used to visualize, store, and manipulate the images. The C-arm allows a great variety of movements, and its characteristic structure makes it possible its use in intraoperative cases, as the arc can be situated around the patient while lying in bed. It is used in different surgical procedures such as cardiology, orthopedics, and urology. The C-arm should be compact and lightweight to allow easy positioning with adequate space to work around and a wide range of motion while yet remaining inflexible enough so as to minimize misalignments due to flexion caused by the weight of the X-ray tube or the image system assemblies.

Figure 1.17: *C-arm equipment with its storage unit and monitoring cart. Model: GE OEC 9800 Plus C-Arm.*

1.5 Towards 3D imaging: tomosynthesis

Tomosynthesis stands as a middle step between planar X-ray radiography and computed tomography. Despite being a tomographic technique like CT, it is unable to completely remove the shadow of out-of-plane structures from the plane being visualised. However, this partial removal of out-of-plane structures may prove to be enough to properly diagnose the patient. It is based on acquiring a few number of radiographies from different views through restricted movements of the source/detector.

Several authors have studied the existing differences among tomosynthesis, CT and planar radiography in different applications, mostly on mammography [Conant et al., 2016] and chest studies [Gomi et al., 2012]. Vikgren et al [Vikgren et al., 2008], for instance, tried comparing these modalities for chest nodule detection (Fig. 1.18).

Figure 1.18: *Results presented by Vikgren et al. From left to right: CT, radiography and tomosynthesis. Pulmonary nodules are marked in red. Source: [Vikgren et al., 2008].*

Tomosynthesis greatly reduces the dose received by the patient when compared with CT; however, the quality of the images obtained is not as high. Thus, tomosynthesis is regarded in these studies as a promising imaging modality due to its good dose-quality ratio.

Digital Tomosynthesis

Digital tomosynthesis is an evolved form of traditional geometric tomography, which started appearing during the 1920s. One of its pioneers was A.E.M. Bocage, who described in 1921 a device capable of blurring out structures out of a plane of interest. This apparatus consisted on three main components: an X-ray source, an X-ray film and a mechanical connection between them that allowed for synchronous movement between them. The principle of conventional tomography is illustrated in Fig. 1.19. To obtain the While traditional tomography allowed successfully producing

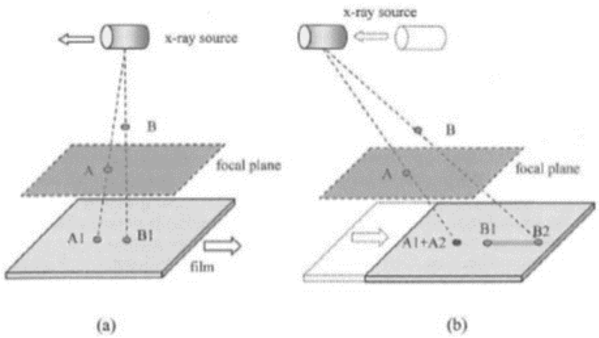

Figure 1.19: *Conventional tomography principle. (a) X-ray source projects points A and B onto A1 and B1. (b) X-ray source and film are moved in such a way that shadow A2 of point A overlaps A1, but shadow B2 of point B does not overlap B1. Source: [Hsieh et al., 2009].*

images at the plane of interest, it presented two main limitations:

- Dose given to the patient: a single acquisition produced an image of a single plane; therefore, in order to image a different plane, the whole process had to be repeated, greatly increasing the dose received by the patient.
- Inability to completely remove structures outside the focal plane: since the whole procedure only manages to blur out-of-focus structures, the contrast of the imaged focal plane is reduced.

In spite of these limitations, this technique enjoyed clinical utilization and was researched on during the following decades, earning the name tomosynthesis in the 1970s. During the 1980s, the advent of spiral CT halted much of the research in tomosynthesis. Interest in tomosynthesis was renewed a decade later, at the end of the 1990s, due to the development of digital flat panel detectors. This new technology allowed for the reconstruction of any given number of planes from a limited number of projection images.

The advent of digital detectors also made the technique more flexible: allowing for a wider variety of possible geometries as well as a wide range of different reconstruction techniques.

In the simplest tomosynthesis geometry, the X-ray tube moves along a straight path parallel to the plane containing the receptor. The receptor may move in synchrony with the tube or remain steady depending on how close it is to the focal plane [Dobbins III and Godfrey, 2003] (Fig. 1.20). These two geometries, denoted parallel path geometries, are used mostly in acquisitions done on a table or in front of a wall stand to image different anatomical sites such as the skull, shoulder, foot [Machida et al., 2010], or the chest [Dobbins and McAdams, 2009].

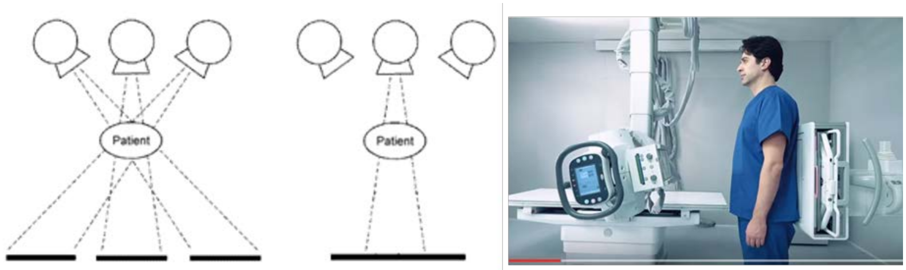

Figure 1.20: *Parallel path geometries. Source: [Dobbins III and Godfrey, 2003]. GE tomosynthesis system.*

Another geometry commonly used in mamography is shown in Fig. 1.21 where the detector is fixed and the source rotates following an arc shape.

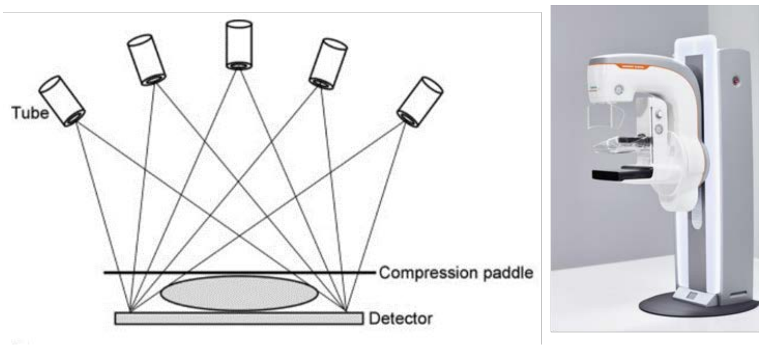

Figure 1.21: *Scheme of a mammography system [Park et al., 2007] and Mammography system from Siemens.*

The images can be reconstructed using a simple algorithm, the Shift-and-Add [Dobbins III and Godfrey, 2003] that implies simple combinations of the shifted projections. Knowing the focal plane, it is possible to find how each plane is projected onto the detector in each acquisition. This principle of this algorithm is illustrated in Fig. 1.22.

It must be noted that the choice of geometry will have an impact on image quality. Issues arise when the detector remains stationary or moves linearly, as oblique angle incident X-ray beams on the detector will increase blurring in the image [Mainprize et al., 2006].

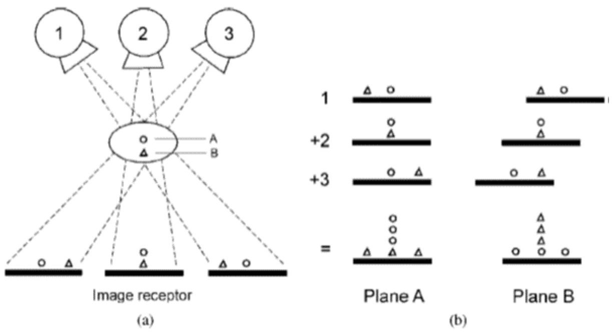

Figure 1.22: *Principle of SAA algorithm. (a) Three positions of the X-ray source and the projected locations of two structures (a circle and a triangle) located in separate planes (A and B). (b) The structures in either plane can be brought into focus by shifting and adding them accordingly. Source: [Dobbins III and Godfrey, 2003].*

1.6 Computed Tomography

CT imaging systems allow us to produce cross-sectional images (slices) of the sample, facilitating the visualization of a certain body part without disturbance of surrounding structures. In tomography, the source and the detector rotate around the patient making several acquisitions called projections.

The most common tomography system used nowadays for clinical applications is the helical one (Fig. 1.23), in which the source and the detector rotate around the patient while this one is longitudinally displaced, so that the X-rays describe a helical trajectory. Its advantages include a short scan time and the consequent minimization of the patient motion artifact [Sisniega Crespo, 2013]. Modern systems can scan the complete human body within a few seconds, which keeps the patient comfort and meets clinical demands with respect to time and dose.

Figure 1.23: *Philips Brilliance 16-Slice CT Scanner.*

Cone-beam CT (CBCT) scanners are also widely used for specific applications, since it allows acquiring the volume without the translation of the object being scanned in a single rotation of the system, adopting the X-ray beam a cone-shape. The maximum resolution is achieved in the center of the field of view; as you move away from the center, details are lost: the same point of the object will be projected onto different detector elements for different projection angles. This problem gets worse as the beam angle becomes higher. In addition, scan times are longer than helical ones.

Although CBCT is not the standard system, it is a very common scanner for some clinical applications such as, C-arm fluoroscopy imaging, breast imaging and radiotherapy [Siewerdsen et al., 2005, Schafer et al., 2012, Boone et al., 2001, Yang et al., 2007, Grills et al., 2008, Jaffray et al., 2002]. Another application for cone-beam geometry is the micro-CT (μCBCT), which provides high resolution images for small objects, such as small animals.

As in the case of humans, the scope of small-animal X-ray imaging is to obtain high quality images delivering the smaller possible dose to the animal. In addition, for the in-vivo studies it is crucial to make the acquisition time as short as possible so that the animal movement does not produce inconsistent projection data. Even if the animal is anaesthetized, the equipment must be placed in the proper way, to avoid problems in the rotation.

1.7 X-ray tomography reconstruction

In CT, the quantity of interest is the attenuation map, denoted as $\mu(\vec{p})$ where $\vec{p} = (x, y, z)$ corresponds to the spatial position. Ideally, the measurements at each detector element can be approximated through the Beer-Lambert′s law:

$$Y = \int_{\epsilon} I_0(\epsilon_0) e^{-\sum_{s=1}^{S} \int_L m_s(\epsilon_0)\rho_s dl} \tag{1.2}$$

where I_0 corresponds to the transmitted intensity, m_s to the mass attenuation coefficient of material s, which is the response dependent on the photons energy (ϵ_0) and ρ_s the material density. From this relation, it is possible to obtain the total attenuation measured, which corresponds to the line integral of the attenuation map along each ray trajectory:

$$-Ln\left(\frac{Y}{\int_{\epsilon} I_0(\epsilon_0)}\right) = \int_L \sum_{s=1}^{S} m_s(\epsilon_0)\rho_s dl = \int_L \mu dl \sim f \tag{1.3}$$

For scans where parallel rays traverse the sample (assumed as 2D) within different angle positions, the total attenuation corresponds to the Radon transform of the attenuation map [Kak and Slaney, 1988]:

$$R(t, \theta) = \int_{-\infty}^{\infty} \mu(x, y)\delta(xcos(\theta) + ysin(\theta) - t)dxdy \tag{1.4}$$

where t corresponds to each ray and θ to the projection angle as it can be shown in Fig. 1.24. The tomographic reconstruction problem consists on estimating $\mu(\vec{p})$ from

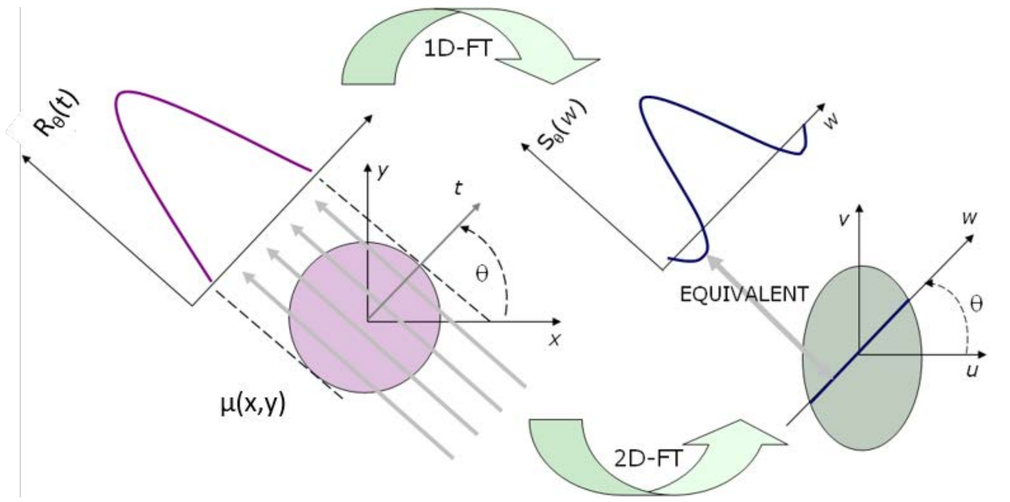

Figure 1.24: *Central slice theorem. Source: [Abella, 2010].*

the measurements f. There are several ways to face this problem, which result in the different tomographic reconstruction methods summed up in Fig. 1.25. Analytical

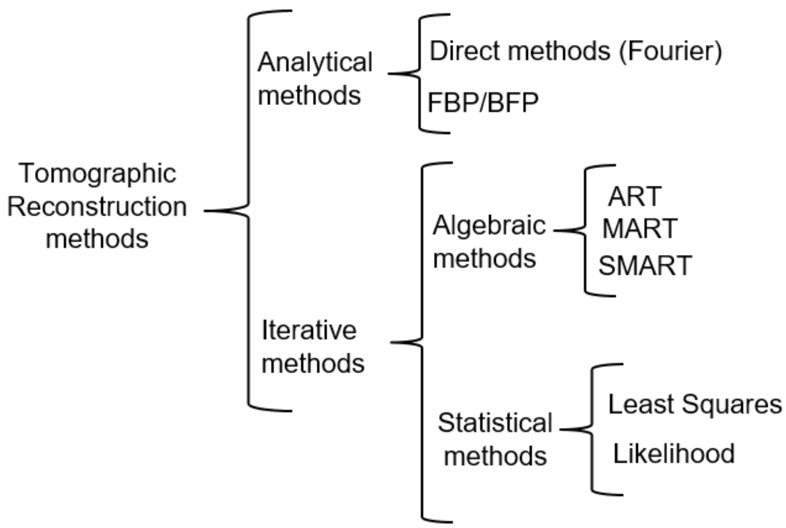

Figure 1.25: *Classification of image reconstruction algorithms. Source: [Fessler and Tutorial, 2006]*

methods calculate the inverse formula of the Radon transform, based on the central slice theorem. This theorem, represented for the 2D case in Fig. 1.24, states that the Fourier transform of a parallel projection of an image μ taken at angle θ gives a line of the two-dimensional Fourier transform, subtending the same angle θ with the u-axis, the horizontal frequency axis [Kak and Slaney, 1988]. In these methods, the solution is given directly calculating the inverse 2D Fourier transform of the sample. Due to the 2D Fourier transform of the sample presents less samples far away the central frequency, more points will be calculated by interpolation resulting in artifacts on edges and details in the final image. Another option is to rewrite the inverse Fourier transform in polar coordinates leading to the filtered back-projection (FBP) formula:

$$\mu(x,y) = \int_0^{\pi} \left[\int_{-\infty}^{\infty} S_\theta(w)|w|e^{j2\pi wt} dw \right] d\theta \tag{1.5}$$

where $S_\theta(w)$ corresponds to the Fourier transform of the radon transform $R_{\theta(t)}$, which is filtered with $|w|$, a ramp filter that enhances the high frequencies (details and edges of the image). Finally each value is backprojected by adding the contribution of at each trajectory (t, θ) at each point (x, y). More details of this process can be found in [Kak and Slaney, 1988].

For the computational implementation of the FBP formula, Eq. 1.5 is discretized and the attenuation map is modeled as a finite discrete approximation through a linear series expansion:

$$\vec{u} \sim \sum_{j=1}^{n} \mu(\vec{x})_j b_j \tag{1.6}$$

where b_j corresponds to basis functions such as pixels/voxels basis where $b_j = 1$ inside the pixel/voxel, and 0 everywhere else. This approach is simple and perfectly matches with digital displays. More approaches have been proposed such as the ones that use blobs (Kaiser-Bessel window functions) as basis function [Lewitt, 1992].

Alternatively, we can approximate the problem as a linear equations system:

$$\begin{pmatrix} A_{11} & A_{12} & \cdots & A_{1n} \\ A_{21} & A_{22} & \cdots & x_{2n} \\ \vdots & \vdots & \ddots & \vdots \\ A_{m1} & A_{m2} & \cdots & A_{mn} \end{pmatrix} \begin{pmatrix} u_1 \\ u_2 \\ \vdots \\ u_n \end{pmatrix} = \begin{pmatrix} f_1 & f_2 & \cdots & f_m \end{pmatrix} + \xi \tag{1.7}$$

where the total measured attenuation (denoted as $f \in \mathbb{R}^m$) is given by applying the system matrix ($A \in \mathbb{R}^{mxn}$) where each element corresponds to the contribution of pixel/voxel i to the line integral of $u \in \mathbb{R}^n$ along each ray path L, and ξ corresponds to errors in the measurements.

The system matrix, A, can be implemented in different ways: considering the ray path as a line and calculating the length of its intersection with each pixel u_j or considering the ray path as a strip and measuring the intersected area with each pixel, etc.

To solve for u in Eq. 1.7, one option is to calculate the inverse of the system matrix, which can be not feasible when the equations system is not well conditioned due to uncertainties in the measurements such as low number of photons, or low number of angle positions, etc.

1.7.1 General scheme of iterative reconstruction methods

Instead of calculating the inverse matrix, the algebraic methods (ART) solve Eq. 1.7 sequencially equation by equation following the Kaczmarz's method [Tanabe, 1971] where the solution is updated iteratively based on the intersection of the hyperplanes obtained projecting the estimations (Fig. 1.26). However, neither these algebraic iterative methods nor the analytical methods work properly when the reconstruction problem is not well conditioned, due to uncertainties in the measurements such as low number of photons, or low number of angle positions, etc.

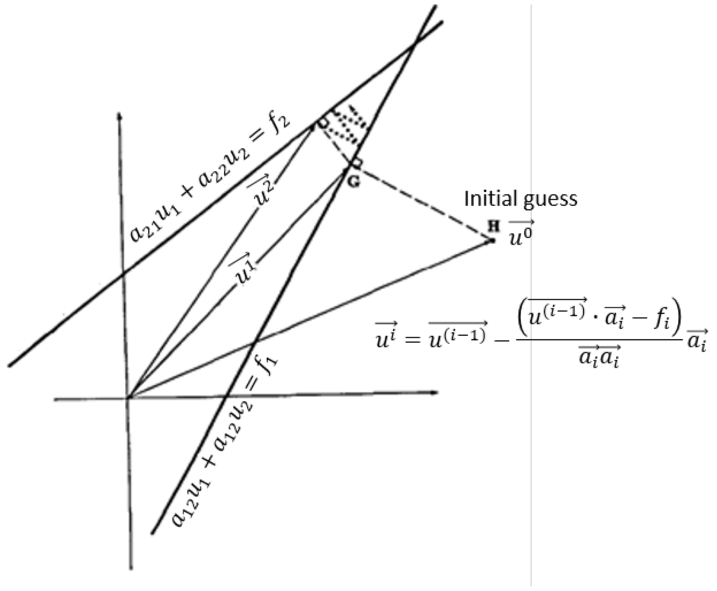

Figure 1.26: *Graphical representation of Kaczmarz's method. Source: [Kak and Slaney, 1988]*

Besides the system geometry, a more realistic model of the system include the physics involved in the image generation such as X-ray photons production or its interaction with matter or the detector efficiency, etc. This allows to reduce possible artifacts presented in the image such as beam hardening, scatter artifacts, etc. For most radiography systems where polychromatic spectra and integrating detectors are used, the measurements model (Eq. 1.2) can be modified as:

$$Y = \sum_{\epsilon} I_0(\epsilon) e^{-\sum_{s=1}^{S} m_s(\epsilon)\rho_s[Au]} \tag{1.8}$$

where the I_0 corresponds to the transmitted polyenergetic spectrum formed of X-ray photons of different energy ϵ. The energy dependency is reflected in the mass attenuation coefficient which is different also for each material.

The iterative method is based on the general optimization problem that minimizes/maximizes a cost function that depends on the solution u. The cost function corresponds to the objective function that usually contains a data-mismatch term, which expresses the differences between the data and its estimation $[Au]$.

When the reconstruction problem is not well-conditioned, the cost function can also include prior assumptions to restrict the possible solutions and help the algorithm to find a solution.

Both data mismatch and prior assumption terms can be expressed as quadratic functions using the L_2 norm or using the L_1 norm as in the case of the Total Variation (TV) function [Rudin et al., 1992].

Thanks to the flexible structure of these advanced iterative reconstruction methods, shown in Fig. 1.27, lots of different advanced iterative methods have been proposed in the literature. They have in common that the solution is updated after each iteration where a cost function that can include the geometrical, physics and/or statistical models is optimized. With this general scheme the physics modeling such as

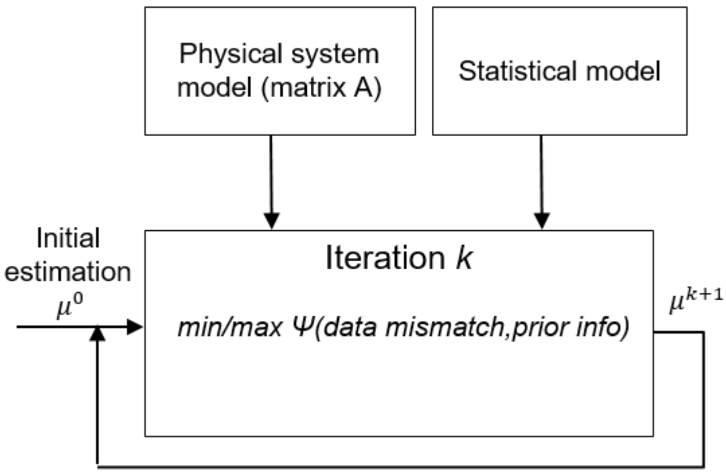

Figure 1.27: *Scheme of an advanced iterative reconstruction method*

collimator, attenuation physics, scattering, detector efficiency, etc. can be included in the system matrix giving a more realistic model of the scan measurements.

Statistical model

Statistical modeling can be included in the general iterative scheme to simulate more accurately the physics phenomena involved in image generation. Generally, this implies the modification of the cost function, what influences the adequate optimization algorithm.

A classic approach is to model the X-ray measurements as random processes that follow independent Poisson distributions [Whiting et al., 2006, Erdogan and Fessler, 1999, Rockmore and Macovski, 1977, Lange et al., 1984] where the mean corresponds to the total number of photons of all energies measured (Eq. 1.8), described by the Beer-Lambert's law [Hsieh, 2003]. Other works modified this model and proposed a shifted Poisson approximation:

$$Y_i \sim Poisson\left\{I_0(\epsilon)e^{-[A\mu]_i} + r_i\right\} \tag{1.9}$$

where r_i corresponds to the background events such as random coincidences, scatter and crosstalk. However, this model ignores some events such as electronic noise and more sophisticated statistical models have been proposed. In [Snyder et al., 1993, Snyder et al., 1995], authors proposed a combination of Poisson and Gaussian model that includes the simulation of photon variability and electronic readout noise. More complex models were also proposed such as the compound Poisson model

[Whiting, 2002, Whiting et al., 2001].

All these proposed statistical models imply the modification of the cost function, therefore it should be optimized in a different way and because of that lots of different algorithms have been proposed. One important line of methods are the ones based on the the maximum-likelihood (ML) estimation, proposed at first time by Rockmore and Macovski [Rockmore and Macovski, 1977]. This method maximizes the probability of having the observed the particular measurements [Fessler and Tutorial, 2006].

Optimization algorithms

When the cost function is differentiable and in the absence of constraints, its optimization can be done solving:

$$\nabla\Psi(u) = 0 \tag{1.10}$$

However, for most image reconstruction problems there are no closed-form solutions to the system of equations [Fessler, 2008], thus an iterative optimization algorithm is required. When choosing the appropriate algorithm, it should be taken into account aspects of the algorithm itself such as convergence rate, robustness, parallelization possibilities, memory requirements, and aspects of the cost function such as if its constrained, unconstrained, convex or non-convex, differentiable or not, etc.

Most of the classic optimization algorithms are based on updating the intermediate solution iteratively varying it an specific quantity in a certain direction until find the optimum:

$$u^k = u^{k-1} + \alpha d^k \tag{1.11}$$

where α^k corresponds to the movement or variation of the intermediate solution u^k in the selected search direction d^k. This algorithm consists on two main steps. One step is the calculation of the search direction, d^k. The other step consists on the optimal finding of the step size α^k.

The gradient-based algorithms differ mostly in the way to determine the search direction. In Algorithms 1,2,3 we detail the steps of three of them: gradient descent, steepest descent and conjugate gradient, which can be considered as starting points to other more sophisticated algorithms.

Algorithm 1 Gradient descent.

1: $Solution\,update : u^{k+1} = u^k - \alpha\nabla\Psi(u^k)$
2: **return** u

where γ^k corresponds to the Polak-Ribiere function [Fessler, 2008].

Newton's methods are based on using the Hessian information for the search direction. They are derived from the second-order Taylor series expansion of the

Algorithm 2 Steepest descent.

1: $Direction : d^k = -\nabla\Psi(u^k)$
2: $Step\,size : \alpha^k = \min_{\alpha\in[0,\infty)} \Psi(u^k + \alpha d^k)$
3: $Solution\,update : u^{k+1} = u^k + \alpha_k d^k$
4: **return** u

Algorithm 3 Conjugate gradient.

1: $Direction : d^k = \gamma^k d^{k-1}$
2: $Step\,size : \alpha^k = \min_{\alpha\in[0,\infty)} \Psi(u^k + \alpha d^k)$
3: $Solution\,update : u^{k+1} = u^k + \alpha^k d^k$
4: **return** u

cost function at initial solution (u^0):

$$\Psi(u) \sim \Psi(u^0) + \nabla\Psi(u^0)^T(u - u^0) + \frac{1}{2}(u - u^0)^T H(u^0)(u - u^0) \tag{1.12}$$

After derivating and setting the result equal to zero, we obtain the following updating formula [Venter, 2010]:

$$u = u^0 - H(u^0)^{-1}\nabla\Psi(u^0) \tag{1.13}$$

With large amount of data, these methods become unpractical because of the computational cost associated with the Hessian matrix. The quasi-Newton methods such as the one proposed by Broyden, Fletcher, Goldfarb and Shanno (BFGS) [Fletcher, 2013], reduced this cost because it calculates an approximation of the inverse of the Hessian matrix only once, and then it is just updated in each iteration with the first-order gradient information [Venter, 2010].

Regarding constrained optimization, there are two main lines of methods, the Sequential Unconstrained Minimization Techniques (SUMT) [Fiacco and McCormick, 1990] and the direct constraint methods. The SUMT methods are based on converting the problem to unconstrained by penalizing the original cost function.

$$\Psi_p = \Psi(u) + \mu H(u) \tag{1.14}$$

where μ corresponds to the penalty parameter of the penalty term $H(u)$. The main difficulties of these methods is the value of the penalty parameter because it affects significantly the convergence of the algorithm and usually must be set extremely large, which may lead to numerical ill-conditioning. Some works calculated the optimum penalty parameter trough the L-curve or similar method [Hansen and O'Leary, 1993, Abascal et al., 2008].

Regarding the direct constraint methods, the most popular lines are Sequential Linear Programming (SLP), Modified Method of Feasible Directions (MMFD) [Vanderplaats and Moses, 1973] or Sequential Quadratic Programming (SQP) [Nocedal and Wright, 2006]. In SLP methods, the problem is converted to linear and then solved, in MMFD methods the search direction is modified in order to follow the constraint bounds and in SQP methods the cost function is approximated with a quadratic function and the constraint functions with a linear approximation.

Chapter 2

Motivation and objectives

Planar X-ray imaging is still the imaging modality most used in medicine covering between 80-90% of the total medical imaging exams. The past decades have seen a rapid evolution towards the use of digital detectors in radiology and a more flexible robotized movement of the system components. Those advances opened the possibility of the development of new functionalities adding new valuable diagnostic information compared with the previous technology.

Some of the current challenges for radiography are to obtain more quantitative images and to reduce the inherent overlap between tissues. In this line, dual energy radiography, based on the acquisition of two radiographies at different source voltages, enables the characterization of soft tissue and bone structures, without adding significant extra acquisition time or radiation dose. Its benefits over conventional radiography have been proven in chest imaging for the differentiation of lung nodules versus calcified lesions (Fig. 2.1) or the identification of tracheal and airway abnormalities [Kuhlman et al., 2006], in abdominal studies for the determination of fat content to predict metabolic syndrome [Rosety-Rodríguez et al., 2013] and in extremities studies, for the assessment of bone mineral density and bone mineral content [Sievänen et al., 1993].

A really disruptive advance would be to obtain 3D imaging with these systems, initially designed just for planar imaging, by taking advantage of the availability of digital detectors and the new more flexible movements of the system mechanics. Incorporating tomographic capabilities into these systems would rely on the acquisition of a limited number of projections, perhaps with non-standard geometrical configurations, which would imply a reduction of the radiation dose delivered to the patient compared to a CT scan. This would be in resonance with the ALARA criteria (As Low As Reasonably Achievable). The versatility of these techniques is enormous, enabling the introduction of tomography in situations where a CT system is not available, such as during surgery or in an ICU, or in which a reduction

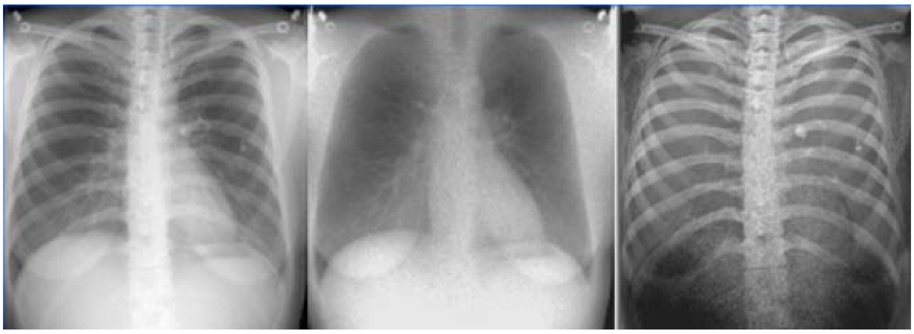

Figure 2.1: *Conventional radiography (left), soft-tissue image (center) and bone image (right). Thanks to the DER technique, it is possible to clasify the lesion seen in the radiography as a calficication in the bone image. Source: State University of New York.*

of radiation dose is key, as in Pediatrics.

The incorporation of tomographic capabilities in radiology systems presents three main challenges. First, due to physical movement limitations, only a few projections can be acquired, typically covering a much smaller angular span than that used in conventional cone beam CT (Fig. 2.2. The 3D reconstruction of these limited data with conventional reconstruction methods such as the proposed by Feldkamp, Davis and Kress (FDK) [Feldkamp et al., 1984] results in severe artifacts. More advanced methods are needed to compensate the lack of data by including additional prior information. These methods generally imply a high computational burden and memory consumption, so acceleration strategies are required to keep the real-time condition. Second, calibration algorithms designed for CT systems [Noo et al., 2000, Johnston et al., 2008] cannot be directly applied to systems with non-standard trajectories, where the relative positions of each component may vary significantly at each projection position and may be subjected to high mechanical tolerance. Third, the optimum number of projections and view angles for these non-standard trajectories have not been studied.

In this context, computer simulations are a valuable tool to explore the possibilities before their actual implementation on real systems. Existing simulation tools for X-ray imaging [Maier et al., 2013, Gallio et al., 2015] generally enable the simulation of only standard acquisition protocols, such as cone-beam with circular trajectory, with strict restrictions regarding source and detector positioning, thus limiting significantly the exploration of new geometries.

The work of this thesis is framed on a research line focused on the advance of radiology systems of the Biomedical Imaging and Instrumentation Group from the Bioengineering and Aerospace Department of Universidad Carlos III de Madrid working jointly with the Gregorio Maran Hospital. This line is carried out in collaboration with the industry, through the company Sedecal, an Spanish multinational among the 10 best world companies in the medical imaging field, and with the Imaging Research Laboratory (IRL) of the University of Washington.

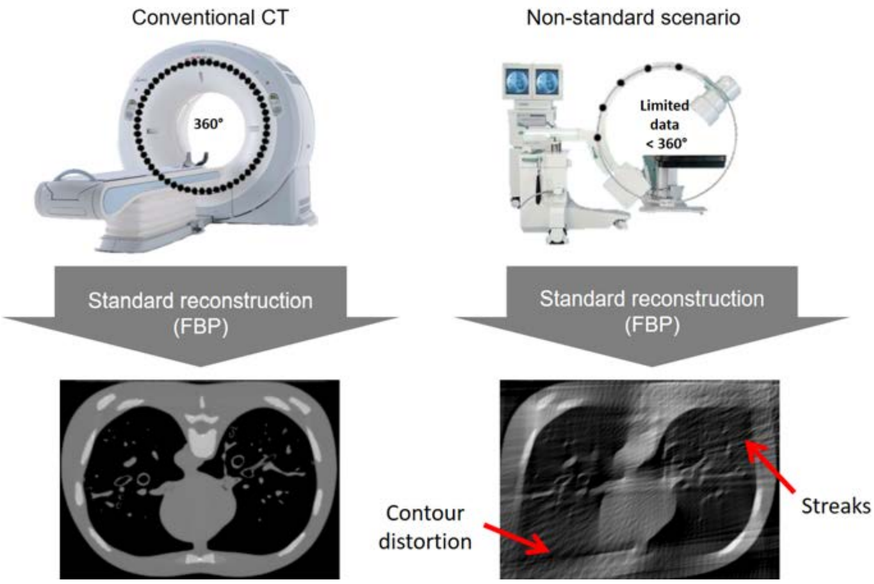

Figure 2.2: *Conventional reconstruction (FBP) of an anthropomorphic phantom from complete data of a conventional CT (left) and from limited data (right).*

2.1 Objectives

The general objective of this thesis is the development of new functionalities for advanced radiology systems. The specific objectives are:

- Research and development of quantitative characterization of different structures through the dual energy technique in radiology systems.
- Research and development of 3D imaging with planar X-ray systems, including image reconstruction algorithms for limited-data tomography.
- Validation of the developed techniques on real systems.

2.2 Thesis outline

The present document is organized into eight chapters:

- Chapter 1 presents an introduction to X-ray imaging and image reconstruction techniques.
- Chapter 2 presents the motivation and objectives of this thesis, and the outline of the document.
- Chapter 3 presents an optimization of dual energy radiography to obtain quantitative studies, including a comprehensive study by simulations and an evaluation on a real system.

- Chapters 4, 5 and 6 present a protocol for obtaining 3D imaging with X-ray planar systems. Chapter 4 describes the geometrical calibration for systems designed for planar imaging[1]. Chapter 5 describes the advanced iterative reconstruction methods proposed for limited-data scenarios, evaluating its performance with simulations[2]. Chapter 6 shows the evaluation of the whole protocol to incorporate 3D capabilities in real systems using anthropomorphic phantoms.
- Chapter 7 presents the general discussion, conclusions and future lines of the thesis.
- Chapter 8 presents the scientific contributions derived from this thesis.

[1] Part of this chapter was extracted from [De Molina et al., 2014]
[2] Part of this chapter was extracted from [de Molina et al., 2018, Abella et al., 2017]

Chapter 3

Dual energy capabilities

3.1 Introduction

Dual energy radiography (DER), based on the differences in attenuation properties of the body tissues for low- and high-energy X-ray photons, enables obtaining separate images for soft-tissue and bony structures. Its benefits over conventional radiography have been proven in chest imaging for the differentiation of lung nodules versus calcified lesions or the identification of tracheal and airway abnormalities [Kuhlman et al., 2006]; in abdominal studies for the determination of fat content to predict metabolic syndrome [Rosety-Rodríguez et al., 2013]; and in limb studies, for the assessment of bone mineral density and bone mineral content [Sievänen et al., 1993].

A DER study comprises the acquisition of radiographies at two different energies, i.e. two different source kilovoltage peak values (kV_p). These measurements in most radiography systems, where polychromatic spectra and integrating detectors are used, can be modeled as:

$$I_{kV_p} = \int_{\epsilon} N_{kV_p}(\epsilon) e^{-\sum_i \int_P \mu_i(\epsilon) dp} d\epsilon, \int_P \mu_i(\epsilon) dp = t_i m_i(\epsilon), t_i = \int_P \rho_i dp \tag{3.1}$$

where I_{kV_p} is the measurement at the detector, $N_{kV_p}(\epsilon)$ corresponds to the emitted photons of each energy ϵ; μ, m, and ρ are the attenuation coefficient, the mass attenuation coefficient, and the physical density of material i, which corresponds to soft tissue (s) and bone (b) along the path P followed by the beam.

From these acquired data, we can obtain the images corresponding to the mass thickness of each tissue, t_s and t_b , referred to as tissue maps along the paper. One common approach, called weighted subtraction, estimates equivalent tissue maps for soft tissue and bone by combining the low- and high-energy measurements with two different global weighting parameters for the whole image [Sawyer, 2007, Shkumat et al., 2007]. In [Sawyer, 2007] the weighting parameters were empirically chosen, by requiring the user to select different regions in the image. The user interaction was reduced in [Shkumat et al., 2007] by estimating an initial approximation of the weightings based on the knowledge of the spectra. In [Ergun et al., 1990, Bellers et al., 2004], instead of a global parameter, authors calculated different weighting parameters depending on the traversed tissue in a previous calibration step. The main disadvantage of these approaches is that results strongly depend on the expertise of the operator.

Following the same idea, other works used higher-order models to relate the tissue maps corresponding to soft tissue and bone, t_s and t_b with their log-measurements, d_L and d_H (second order [Lehmann et al., 1981, Heinzerling and Schlindwein, 1980, Chuang and Huang, 1988], third order [Alvarez and Macovski, 1976, Brody et al., 1981], or other models such as hyperboloid with eighteen terms [Cardinal and Fenster, 1990]):

$$t_s = \sum_{m,n=0}^{M,N} q_{mn} d_L^m d_H^m, t_b = \sum_{m,n=0}^{M,N} r_{mn} d_L^m d_H^n; d_{kV_p}^{2D} = (t_s, t_b) = Ln\left(\frac{I_{kV_p}}{\int_\epsilon N(\epsilon)d\epsilon}\right) \quad (3.2)$$

where the model parameters, q_{mn}, and r_{mn}, can be obtained from a calibration step, by acquiring different known combinations of t_s and t_b at low and high energies that corresponds to d_L and d_H. The equivalent materials used for the calibration need to resemble the attenuation to X-rays of soft-tissue and bone for different energies, which can be represented by the dual-material dependency with the energy, $d_{L,H}^{2D}(t_s, t_b)$, shown in Fig.3.1.

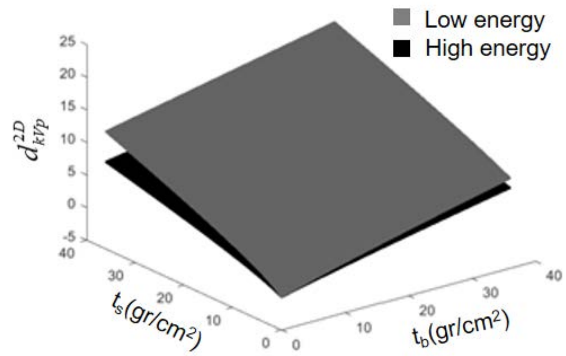

Figure 3.1: *Dual-material dependency of the system: dependency between the log-measurements, d_{kVp}^{2D}, and different combinations of traversed soft tissue (t_s) and bone (t_b).*

Regarding soft-tissue equivalent material, we found in the literature that PMMA [Lehmann et al., 1981, Heinzerling and Schlindwein, 1980, Cardinal and Fenster, 1990], water [Brody et al., 1981] and plastic [Chuang and Huang, 1988] were used. For bone equivalent material, we found aluminum in most works [Lehmann et al., 1981, Chuang and Huang, 1988, Brody et al., 1981, Cardinal and Fenster, 1990], and also calcium sulfate powder [Heinzerling and Schlindwein, 1980]. Nevertheless, no previous works have presented a thorough study of the material properties needed to select the optimum substitute materials that best characterize the X-ray system.

This calibration can be eased by using a calibration phantom of a specific shape that enables the measurement of all possible combinations of soft tissue and bone found in clinical studies, needed for an accurate characterization of a real system, at once. Little information is found in the literature on the optimal shape and size of this phantom. The works in [Heinzerling and Schlindwein, 1980, Chuang and Huang, 1988, Cardinal and Fenster, 1990] are based on numerical simulations of different thicknesses with very small step, of ideal materials difficult to achieve in a real experiment. In [Brody et al., 1981], a phantom formed by two wedges was suggested to acquire at the same time multiple combinations of the two materials. The estimation of the traversed mass thicknesses, t_s and t_b in Eq. 3.2, corresponding to each measurement can be easily obtained in the case of CT systems, by segmenting both materials in the 3D reconstruction of the calibration phantom [14, 15]. Nevertheless, it becomes a more complex process in planar systems due to the lack of tomographic data. In these scenarios, the traversed thicknesses can be obtained from a simulation of the phantom placed in the system during the acquisition, provided we have the complete geometric characterization. In this work, we use simulations to study the optimum design of the calibration phantom regarding material and size and to evaluate the effect of errors in the estimation of the geometry needed to calculate the traversed mass thicknesses corresponding to each measurement. From the results of the simulation study, we selected four designs and tested them in practice using a NOVA FA X-ray system from SEDECAL.

3.2 Dual energy calibration: simulation study

Simulations were carried out using FUX-SIM [Abella et al., 2017], a simulation framework for X-ray systems. 70 kVp and 140 kVp spectra were generated with Spektr [Siewerdsen et al., 2004] and physical properties of materials were extracted from National Institute of Standards and Technology (NIST) [Hubbell and Seltzer, 1995]. A chest CT of the antromorphic phantom PBU-60 (Kyoto Kagaku) was obtained with the Toshiba Aquilion/LB scanner with a voxel size of 0.931 mm $\times$ 0.931 mm $\times$ 0.5 mm, segmented into soft tissue and bone volumes by thresholding and converted from Hounsfield Units to ideal density values by a linear transformation. This transformation was obtained by measuring the mean value on homogeneous regions of air and soft tissue and assigning them to ideal density values of 0 and 1.06 gr/cm^3 respectively, as described in Report 44 from the International Commission on Radiation Units and Measurements (ICRU). We simulated two spherical lesions smaller than 10 mm, which is a size limit reported to show a low rate of detection using conventional chest radiography [Diederich and Wormanns, 2004]. One is a nodule, with $\rho = 1.1$ gr/cm^3 and a diameter of 8 mm, was placed behind ribs and the other one is a calcification, with $\rho = 1.4$ gr/cm^3 and a diameter of 6 mm, was placed behind the heart (Fig. 3.2, top). None of them can be seen in the simulated low and high-energy radiographies (bottom panel of Fig. 3.2). The ideal tissue maps were calculated by projecting separately the soft tissue and bone volumes and used as the references images for the dual energy subtraction.

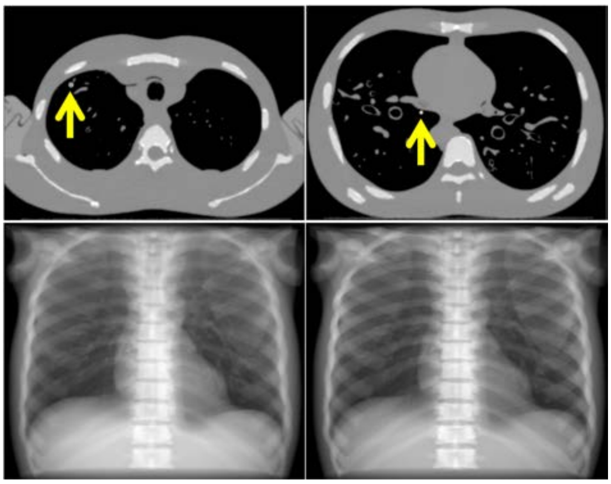

Figure 3.2: *Top: axial slices of the chest CT of the antropomorphic phantom PBU-60 (Kyoto Kagaku) with a soft tissue nodule (left) and a calcificaton (right). Bottom: Simulated low-energy (left) and high-energy (right) chest radiographies.*

We simulated a calibration phantom made of two wedges of equivalent soft tissue and bone materials, as suggested in [Alvarez and Macovski, 1976]. The geometry used for the simulations is shown in Fig. 3.3, with the soft-tissue equivalent wedge closer to the X-ray source, so we can obtain measurements of soft-tissue only.

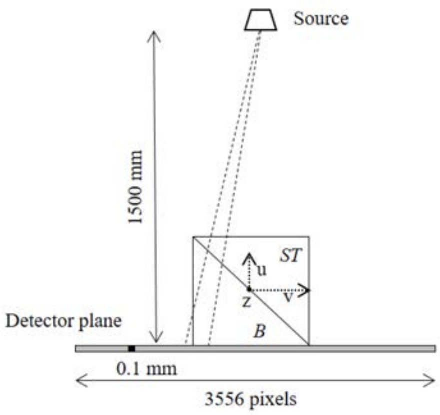

Figure 3.3: *Geometry used for simulations. ST and B refers to the equivalent soft tissue and bone materials, respectively.*

The whole workflow followed for the simulation study is summarized in Fig. 3.4. We first study the candidate materials for each tissue regarding its physical properties, manufacturability, cost and energy dependency. Considering the previous results for each material, we selected the optimum pair of soft-tissue and bone equivalent materials and performed simulations with five phantom sizes. Finally, with the phantom selected we evaluated the impact of errors in the positioning of the phantom using ten simulations with different positioning errors along u-axis and v-axis (Fig. 3.3).

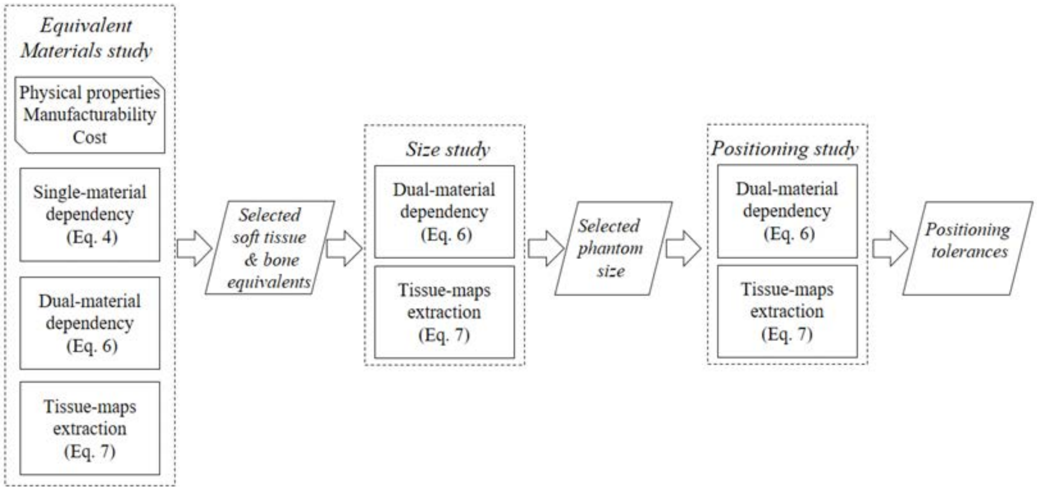

Figure 3.4: *Workflow of the simulation study.*

Fig. 3.5 shows the materials studied for soft tissue and bone wedges of the phantom, most of them previously proposed in the literature as bone and soft-tissue substitutes. Since it is not possible to have a phantom made of water, we tested a hollow prism of PMMA with a wall thickness of 5.6 mm filled with water (we will refer to this phantom to as "water in PMMA". Similarly, since the manufacturing of a pure aluminum phantom is not possible, due to its low machinability, we evaluated available alloys from [20] with few impurities of metals with low atomic number and good machinability. Alloy AL6082 was found to be very similar to the pure aluminum one ($Z = 13$) containing very low concentration of heavy metals (only iron).

A simulation was run to evaluate each candidate material in Fig. 3.5, using a calibration phantom composed of the evaluated material in the corresponding wedge and the ideal material in the other wedge.

For each simulation, besides evaluating physical density, mean ratio of atomic number-to-mass (Z/A), manufacturability, and cost, we studied the theoretical dependency with the energy. We will refer to the latter as the *single-material dependency*, $d^{1D}_{kVp}(t_{candidate})$, calculated as:

$$d^{1D}_{kVp}(t_{candidate}) = Ln\left(\frac{\int_{\epsilon} N_{kVp}(\epsilon) e^{-t_{candidate} m_{candidate}(\epsilon) d\epsilon}}{\int_{\epsilon} N_{kVp}(\epsilon) d\epsilon}\right) \tag{3.3}$$

$d^{1D}_{kVp}(t_{candidate})$ was calculated for mass thicknesses values up to 27 gr/cm^2 and 12 gr/cm^2 for soft tissue and bone respectively (these limits were obtained from a standard chest study [Shkumat et al., 2007] in steps of 0.2 gr/cm^2). Fig. 3.6 shows this single-material dependency , which can be modeled with a perfect fit ($R^2 = 1$) with a second and a fourth order power series for the log-measurements of soft tissue and bone, respectively.

Material	*Soft Tissue equivalent*				
	Ideal Soft Tissue (ICRU-44)	**Water**	**PMMA**	**Plastic A-150**	**Water in PMMA**
Density (gr/cm³)	1.06	1	1.18	1.127	n/a
Z/A ratio	0.55	0.555	0.539	0.549	n/a
Manufacturability	n/a	Difficult	Easy	Difficult	Easy
Cost	n/a	Low	Low	High	Low

Material	*Bone equivalent*				
	Ideal Cortical Bone (ICRU-44)	**Teflon**	**B-100**	**Pure Al**	**AL6082**
Density (gr/cm³)	1.92	2.25	1.45	2.7	2.7
Z/A ratio	0.515	0.48	0.527	0.482	*
Manufacturability	n/a	Easy	Easy	Impossible	Easy
Cost	n/a	Low	High	Low	Low

Figure 3.5: *Materials evaluated for soft tissue and bone substitutes. * Information from manufacturer is not available.*

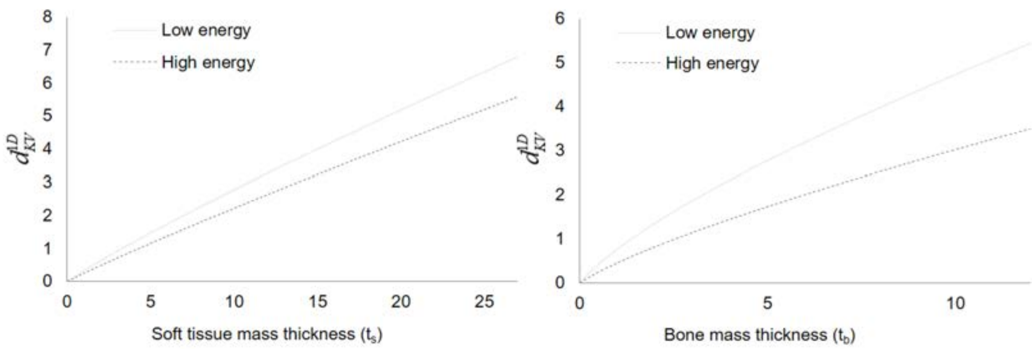

Figure 3.6: *Single-material dependency of ideal soft tissue (left) and cortical bone (right) for low and high-energy spectrums.*

We calculated the single-material dependency error (SME) as:

$$SME = |d_{kVp}^{1D}(t_{candidate}) - d_{kVp}^{1D}(t_{ideal})| \tag{3.4}$$

where $t_{candidate}$ and t_{ideal} correspond with the mass thicknesses of the candidate and ideal materials respectively.

Additionally, we obtained the *dual-material dependency*, $d_{kVp}^{2D}(t_s, t_b)$, by simulating the volume corresponding to each material (size 280 mm, 0.07 mm isotropic voxel) with density values corresponding to the soft-tissue and bone materials for each experiment. The traversed mass thickness of each material (t_s and t_b in Eq. 3.1) was obtained by projecting these volumes and used to simulate the 2D low and high-energy log-measurements applying Eq. 3.2. The whole process is depicted in Fig. 3.7.

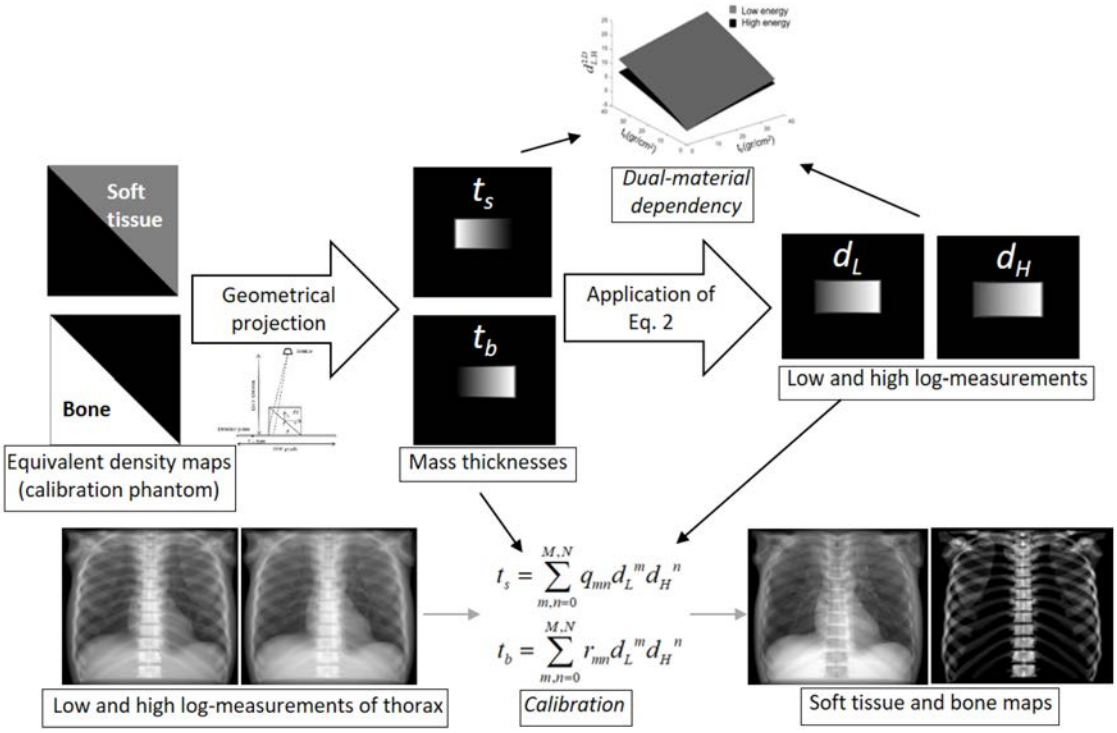

Figure 3.7: *Workflow of the simulation study.*

Taking into account the order of the power series with the best fit for the *single-material dependency* of ideal soft tissue and bone mentioned previously, the *dual-material dependency* of the system was fitted with a power series of M=2 and N=4 orders with 12 coefficients:

$$d_{kVp}^{2D}(t_s, t_b) = \sum_{m,n=0}^{M,N} a_{mn} t_s^m t_b^n \tag{3.5}$$

The dual-material dependency error, *DME*, was calculated as the percentage of the root mean squared error between the values of d_{kVp}^{2D} obtained with the tested phantom and those obtained with the ideal phantom:

$$DME(\%) = \frac{\sqrt{\frac{1}{n}\sum_{i=1}^{n}\left(d_{kVp}^{2D}(t_{s_{tested}}, t_{b_{tested}}) - d_{kVp}^{2D}(t_{s_{ideal}}, t_{b_{ideal}})\right)^2}}{\left(\frac{1}{n}\sum_{i=1}^{n} d_{kVp}^{2D}(t_{s_{ideal}}, t_{b_{ideal}})\right)} \times 100 \tag{3.6}$$

Dual-material dependency, d_{kVp}^{2D}, was calculated for the same mass-thicknesses range and step as the ones used for single-material dependency. Finally, the calibration parameters q_{mn}, and r_{mn} in Eq. 3.2 were obtained using the mass thicknesses combinations and the corresponding log-measurements, as shown in Fig. 3.4. Since we expect a relation between mass thicknesses and log-measurements equivalent to that of the dual material dependency, same order power series were used (M=2 and N=4). We used this calibration to obtain the tissue-maps on the simulated DER chest study of the anthropomorphic phantom PBU-60 (Kyoto Kagaku). The quality of the tissue-maps was assessed in terms of the Tissue Maps Error (*TME*) calculated as the difference between ideal tissue-maps and the tissue-maps obtained:

$$TME(\%) = \frac{\sqrt{\frac{1}{n}\sum_{i=1}^{n}\left(t_{s_{tested}}, t_{b_{tested}} - t_{s_{ideal}}, t_{b_{ideal}}\right)^2}}{\left(\frac{1}{n}\sum_{i=1}^{n} t_{s_{ideal}}, t_{b_{ideal}}\right)} \times 100 \tag{3.7}$$

3.2.1 Study of equivalent materials

Soft-tissue equivalent

To study the best candidate material for soft tissue mimicking, we set one wedge of ideal cortical bone (ICRU-44) and made the other wedge of PMMA, water, plastic A-150, and a prism with a wall thickness of 5.6 mm filled with water (water in PMMA). All candidates have a relative difference with ideal soft tissue below 12% in density and below 2% in Z/A ratio, respectively. Water and plastic A-150 showed the smallest difference (Fig. 3.5). Left panel of Fig. 3.8 shows the *single material dependency error (SME)* corresponding to different mass thicknesses for the case of the low-energy spectrum, which resulted in higher errors. We obtained higher *SME* for PMMA, increasing proportionally to the amount of traversed material, while water showed the smallest *SME*. This behavior is also reflected in the *dual-material dependency error (DME)*, where water showed a *DME* below 0.5% followed by water in PMMA (0.69%) and by Plastic A-150 (below 1%) as shown in Fig. 3.8, right.

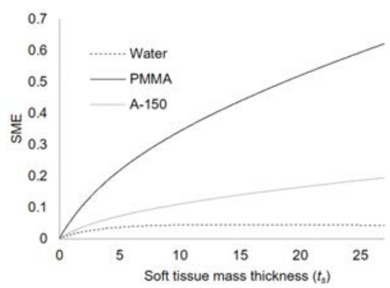

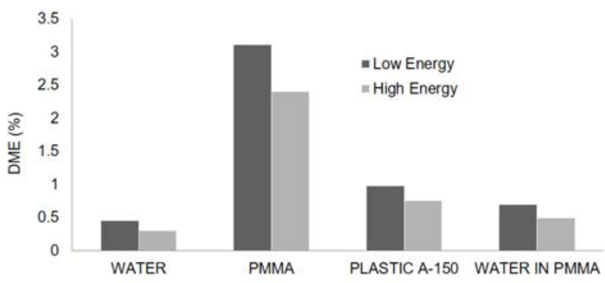

Figure 3.8: *Single-material error (SME) and dual-material dependency error (DME) for all soft tissue candidate materials.*

Fig. 3.9 shows the results for the tissue-maps. All candidate materials led to soft-tissue maps with *TME* under 6%; bone maps present higher error, especially for PMMA with a *TME* of 51%.

Fig. 3.10 shows the bone maps, with the calcification located behind the heart

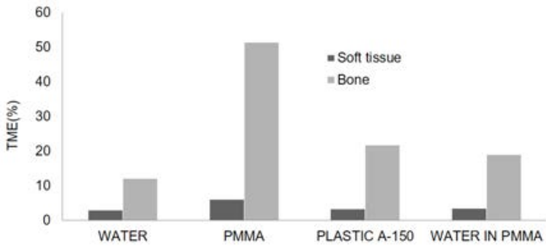

Figure 3.9: *Tissue Map Error (TME) for all soft tissue candidate materials.*

clearly visible in the three cases. The contrast, measured as the ratio between the mean value in the nodule and the mean value in the background (Fig. 3.10), resulted in a lower value (1.3) in the map obtained with the PMMA phantom compared with plastic A-150 (2.06), water (2.99) and the water in PMMA (1.84). The soft tissue in the stomach area was also not completely removed with the solid PMMA phantom.

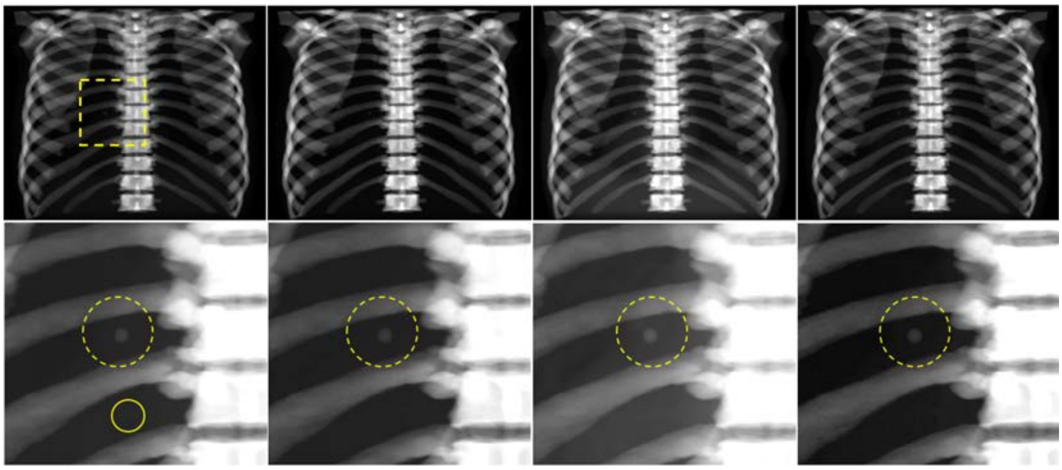

Figure 3.10: *Top: bone maps obtained with the different candidate materials, plastic A-150, water, PMMA and water in PMMA, with same window width and level. Bottom: zoom of the area within the yellow square with dashed line shown in top-left panel for the three cases. Solid-line circle in left panel indicates the area used as background for the calculation of the contrast. Dashed-line circles indicate the calcification in each image.*

From these results, water would be the optimum material for soft-tissue equivalent. A more realistic option is the hollow PMMA prism filled with water, which provides similar results, but entails some practical issues such as the need of avoiding bubbles formation during the filling, possible evaporation over time and waterproofness.

Considering solid materials, the second candidate with closer physical density, Z/A ratio and smaller errors for both single- and dual-material dependency and tissue-maps is plastic A-150. However, it is mostly constituted by carbon, which complicates its structural integrity during machinability and also by nylon and polyethylene, with very different melting temperature. This makes its construction very difficult and requires specialized companies at a very high cost [Braby et al., 1995, Collums, 2012].

Although PMMA presents high values both for *SME*, *DME* and *TME* compared with the other candidates, these errors mainly affect the stomach area of the bone map while it allowed the correct identification of the calcification (Fig. 3.10, bottom).

Bone equivalent

To evaluate candidate materials for bone mimicking, we set one wedge of ideal soft tissue ICRU-44 and tested Teflon, B-100, pure aluminum and alloy AL6082 in the other wedge.

Fig. 3.5 shows that all candidates are similar to ideal bone regarding Z/A. Teflon and B-100 are the materials with more similar density to ideal bone, with relative differences of 17% and 24% respectively, compared to aluminum, with a difference of 40%. However, in the left panel of Figure 10 we can see that Teflon presents the highest *SME*, 1300 times compared with the alloy of aluminum, increasing proportionally with the amount of traversed tissue. The phantom made of alloy of AL6082 shows a clear independence of the *SME* with the traversed tissue, which ensures low error for large amounts of traversed bone. Regarding *DME* (Fig. 3.11, right), the alloy AL6082 presents the smallest *DME* (lower than 1.5%) for low and high-energy spectrums, while the highest error was obtained with Teflon (25%).

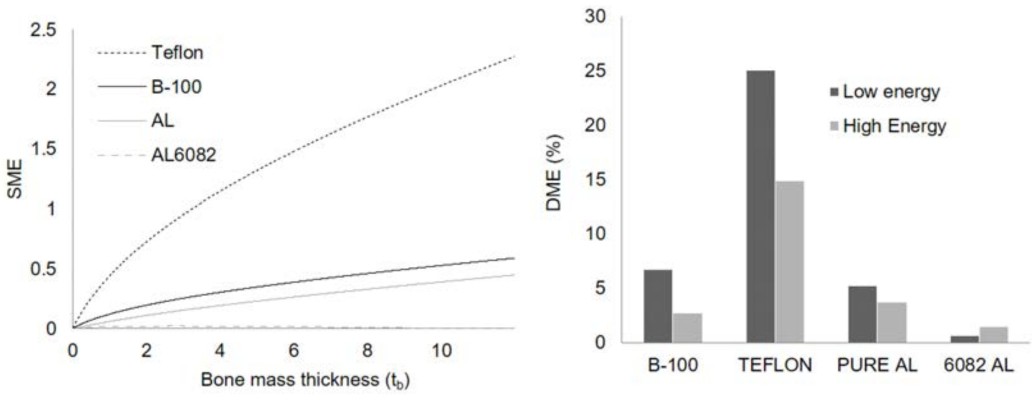

Figure 3.11: *SME (left) and DME (right) for all soft tissue candidate materials.*

Regarding the two tissue-maps, higher TME values were obtained for the bone. AL6082 presented the lowest error, 2% for soft tissue-map and 7% for bone map, compared with the rest of materials (Fig. 3.12).

We can see in Fig. 3.13 that the soft-tissue map allows the differentiation of the soft-tissue nodule behind the rib, with all candidates except for Teflon.

Quantitatively, the alloy AL6082 presents the best results and together with its good machinability, availability and cost (around 2 €/kg) makes this material an appropriate option for substituting cortical bone during calibration.

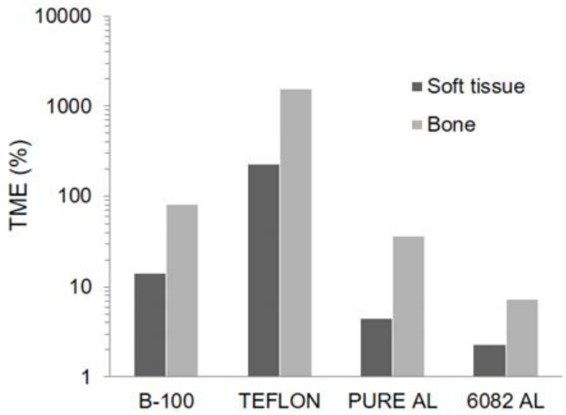

Figure 3.12: *TME (logaritmic scale) of obtained tissue-maps for all bone candidates.*

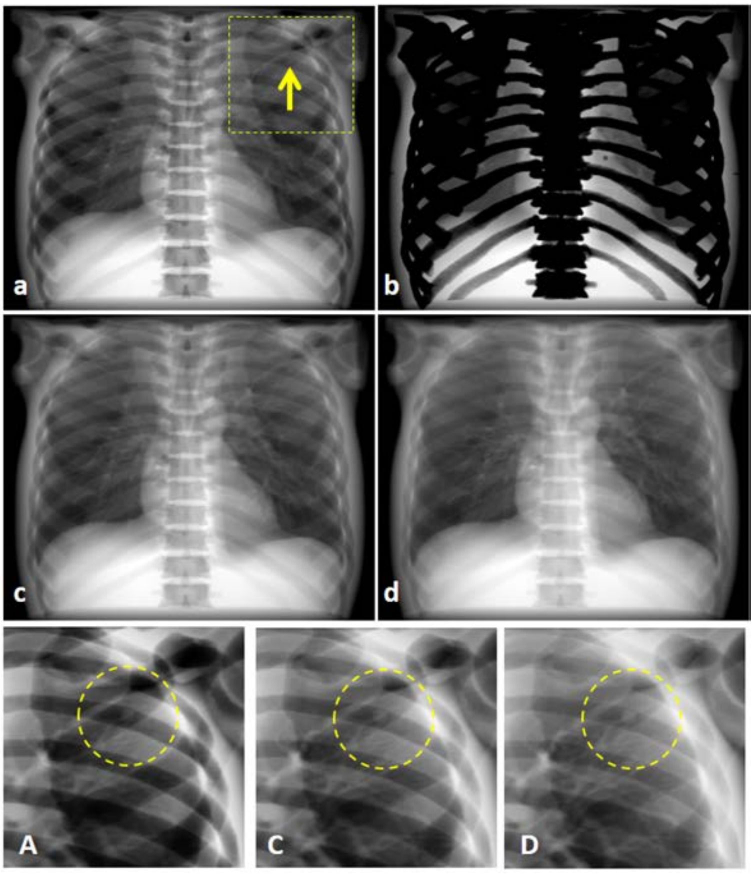

Figure 3.13: *Soft tissue map obtained with plastic B-100 (a), Teflon (b), pure aluminum (c) and AL6082 (d) with same window and level. Zoom of the area within the yellow square (a) for the plastic B-100 map (A), pure aluminum map (C) and AL6082 map (D). Yellow circles indicate the location of the soft-tissue nodule.*

3.2.2 Phantom size

To study the optimum size to cover enough mass thickness combinations of soft tissue and bone, we simulated five wedge phantoms made of the optimum materials found in the previous section, i.e., PMMA and AL6082. Simulations followed the geometry in Fig. 3.3 for phantom sizes of 50, 100, 150, 200 and 250 mm, with a voxel size of 0.07 mm.

Plots of the mass thickness combinations obtained with the different phantoms (Fig. 3.14) show a lack of values corresponding to small amount of soft tissue and large amount of bone, which increases with the phantom size. Nevertheless, the missing data would be not present in a standard chest study, as it can be seen in the case of the anthropomorphic phantom PBU (right panel of Fig. 3.14).

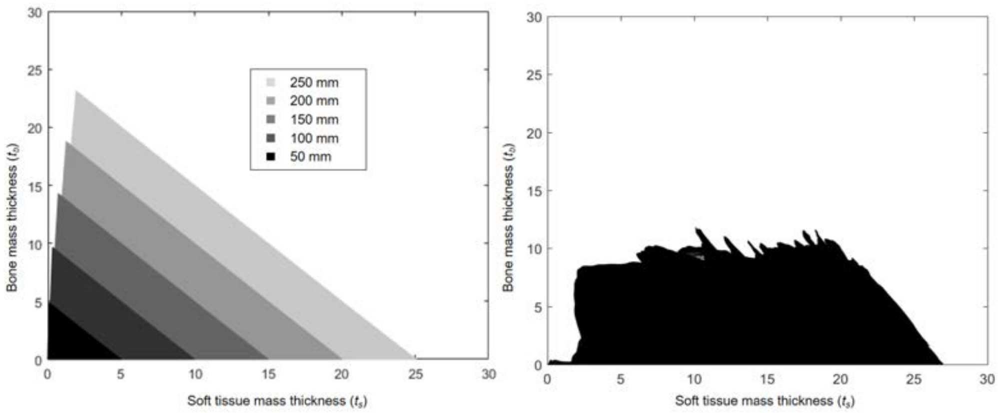

Figure 3.14: *Left: Thickness combinations of soft tissue and bone provided with phantom sizes of 50, 100, 150, 200 and 250 mm (left). Right: thicknesses obtained with the anthropomorphic thorax phantom (right).*

Left panel of Fig. 3.15 shows that *DME* decreases to 3% for the phantom size of 150 mm and stays constant for larger phantoms. The effect in the tissue maps (*TME*, Fig. 3.15 , right) follows a similar pattern. From these results, we can conclude that a phantom size of 150 mm is large enough for a proper calibration, with larger phantoms not resulting in lower *DME* or *TME* values.

Fig. 3.16 shows the soft tissue and bone maps obtained with the 50 mm and 150 mm phantoms.

3.2.3 Phantom positioning

We studied how errors in the estimation of the acquisition geometry along u and v axis in Fig. 3.3 affect both the *DME* and *TME* values. The effect of z-axis error was not considered, since the phantom does not change along that axis. We carried out ten experiments simulating errors of 1, 2, 3, 4 and 5 mm along each axis using a phantom with size of 150 mm, voxel size of 0.07 mm and made of PMMA and AL6082.

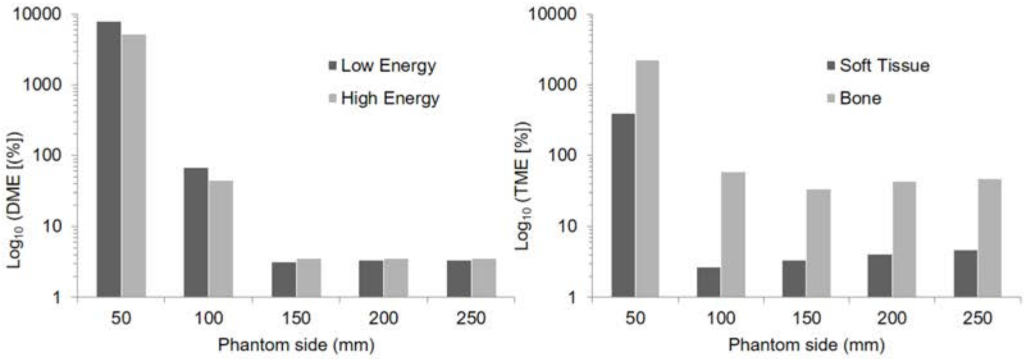

Figure 3.15: *DME (logaritmic scale) (left) and TME (right) between the ideal and different phantom sides.*

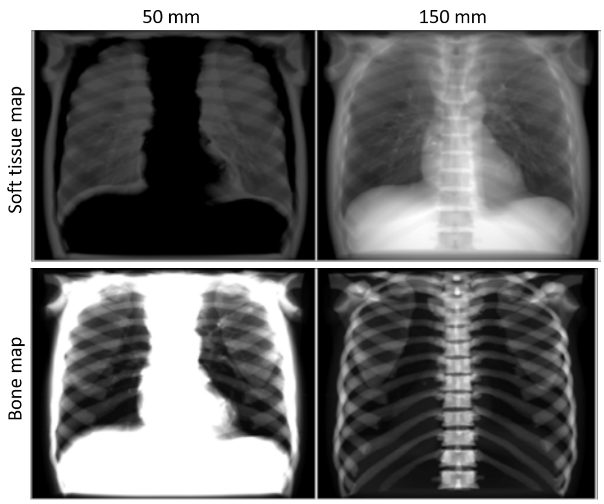

Figure 3.16: *Soft tissue and bone maps obtained with the 50 mm and 150 mm phantoms composed by PMMA and AL6082.*

Fig. 3.17 shows that errors along the u axis do not affect *DME* nor *TME* values. Fig. 3.17 shows that u-axis errors do not affect *DME* nor *TME* values. For errors along the v axis, *DME* increases linearly and only the bone map is affected.

v-axis errors larger than 4 mm result in an incomplete subtraction of ribs and spine from the soft-tissue map and a contrast reduction that hinders the identification of the small lesions (left panel of Fig. 3.18). Errors along v-axis of about 1 mm result in an incomplete subtraction of the abdomen in the bone map (Fig. 3.18, right).

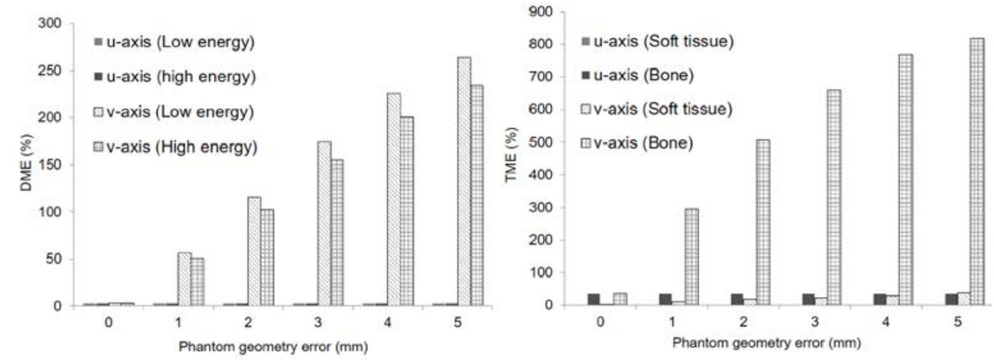

Figure 3.17: *DME (left) and TME (right) for different geometry errors along the u and v axis.*

Figure 3.18: *Soft tissue map (left) and bone map (right) obtained with 4 mm and 1 mm respectively of error along v-axis.*

3.3 Dual energy calibration: real data study

The study on real data was done using a clinical NOVA FA system from SEDECAL (Fig. 3.19). The images were acquired with a flat panel detector Perkin Elmer XRpad 4320x3556 with a pixel size of 100 μm and an anti-scatter grid with grid ratio of 10:1. The source parameters were 70 kVp and 140 kVp for low and high-energy acquisitions respectively, selecting the mAs using the automatic exposure control (AEC) of the system to ensure similar SNR in all images.

We acquired a dual energy chest study of the PBU-60 (Kyoto Kagaku) phantom at 70 kVp and 140 kVp, with an exposure of 10.24 mAs and 1.5 mAs respectively, chosen using the AEC located in the spine (Fig. 3.19). Projection images were filtered with a 2D Gaussian smoothing kernel with standard deviation of 2 pixels (0.2 mm) to reduce the Moiré effect caused by the anti-scatter grid.

We tested the calibration phantoms constructed, shown in the left panel of Fig. fig:RealPhantoms: PMMA-AL6082 phantoms with sizes 50x50x200 mm (1), 100x100x50 mm (2), 150x150x50 mm (3) and water in a case of 3 mm together with AL6082 with size of 150x150x50 mm (4).

Low- and high-energy projections were obtained with the phantom placed approximately in the center guided by the cross-hair formed by the light beam of the collimator and the positioning laser pointer (Fig. 3.20, center).

We simulated two digital volumes corresponding to the soft-tissue and bone

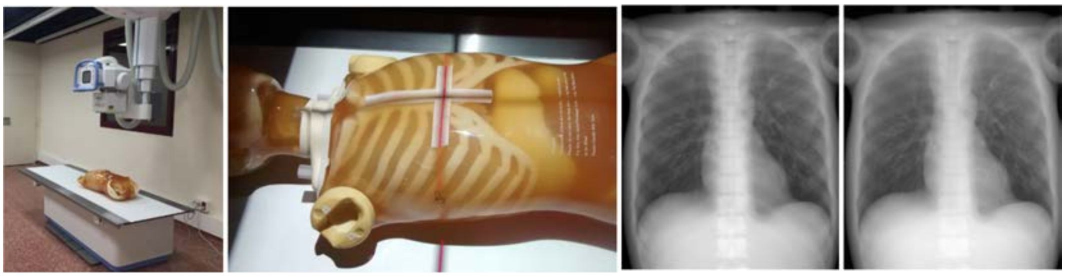

Figure 3.19: *From left to right: NOVA FA system from Sedecal, PBU-60 phantom prepared to acquire, low-energy and high-energy projections of the thorax phantom.*

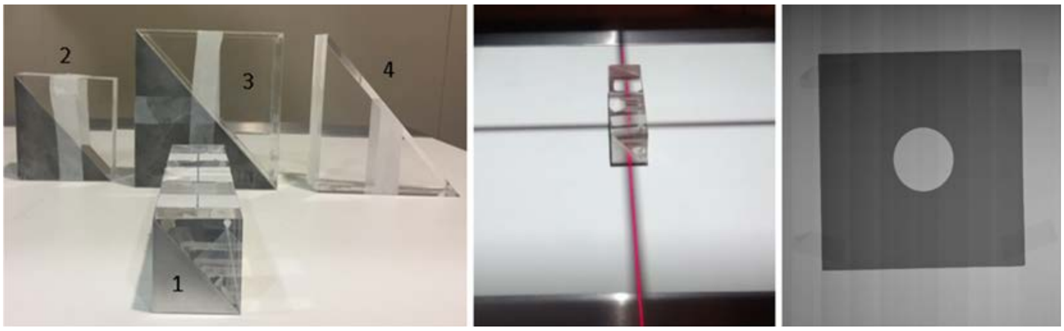

Figure 3.20: *DE calibration phantoms evaluated (left), phantom centered with the laser pointer (left).*

wedges with isotropic voxel of 0.1 mm were created and projected assuming the phantom located in the center along the x- and z- axis. The position along the y axis was calibrated acquiring three different radiographies at detector to source distances of 50, 75 and 100 cm of the aluminum filter with a hole of 51.5 mm diameter placed on top of the bed. The magnification calculated at the three distances was used to estimate the distance between the bed and the detector (as the average of the three values obtained). The horizontal and vertical position of the phantom (v-axis and z-axis in Fig. 3.3) was refined registering the projection data using a rigid transformation. The result of this process corresponds to the estimated soft tissue (t_s) and bone mass thicknesses (t_b).

To reduce the noise, the acquired data were fitted to a power series with $m = 2$ and $n = 4$. Calibration parameters were obtained using soft-tissue and bone values constrained to the maximum mass-thicknesses found in a clinical study (27 gr/cm^2 and 12 gr/cm^2). Fig. 3.21 shows the soft-tissue and bone maps of the chest study obtained when using the evaluated calibration phantoms. The best separation was obtained when using the two largest phantoms (150 mm).

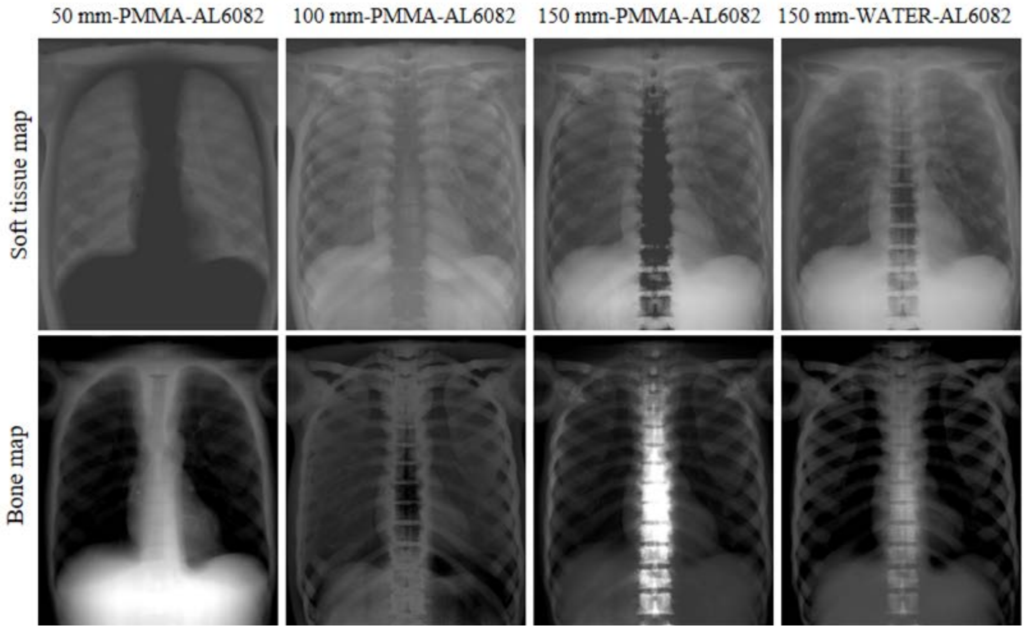

Figure 3.21: *Top: soft tissue maps. Bottom: bone maps. From left to right: maps obtained with the evaluated phantoms 1, 2, 3 and 4. All images are shown with the same window.*

3.4 Discussion

We have presented a comprehensive study of the design of an optimum calibration phantom for Dual Energy Radiography using both realistic simulations and real data acquired with an X-ray system.

The results of the simulation study showed that the energy dependency is key to choose equivalent materials, which has a larger impact on the quality of the results than the physical density. For all the materials tested, higher errors were obtained for the low-energy spectrum, due to the larger differences of the mass attenuation coefficients at low energies. This resulted in errors in the soft-tissue map when non-ideal bone materials were tested and vice versa. As soft tissue equivalent, water outperformed significantly the rest of candidate materials showing errors below 0.5% in the energy characterization and 12% in the obtained tissue maps. We have shown that adding the necessary case of PMMA increases errors up to 0.69% and 12%, respectively, but the maps are visually similar. However, it should be taken into account that water-based phantoms require waterproofness and avoid bubble formation, which are not a problem if using the least expensive solid material PMMA. The results with solid PMMA also showed a good visual identification of the lesions but no quantitative values (TME of 51%).

Teflon, a material widely used as bone equivalent resulted not optimum for DER, showing wrong values in the obtained tissue maps. As bone equivalent, Teflon presented the highest error in the energy characterization, 1300 times higher compared with the alloy AL6082. The latter showed the lowest errors both in energy dependency and tissue maps (7.2%).

Regarding phantom size a length of 150 mm was enough to yield correct tissue maps. Larger phantoms do not improve the results and only unnecessarily incremented the phantom weight. The positioning study of the phantom showed almost no effect of errors along the u-axis. Regarding v-axis, errors below 4 mm do not affect the soft-tissue maps. Higher sensitivity was found for the bone map, where the abdomen was not properly subtracted with error values higher than 1 mm, although the calcification was yet visible. Following the experimental protocol, including geometric calibration and registration, we can expect lower errors in both axes.

Feasibility of the complete protocol was validated with real data, using a phantom of 150 mm made of alloy AL6082 and a hollow PMMA prism with wall thickness of 3 mm. As in simulation results, the abdomen was not completely removed from the bone map. Nevertheless, the clinical impact of this problem might not be important in chest imaging, since it does not hinder the visualization of the lung to evaluate ground glass opacity or nodules.

Evaluations with a thorax phantom showed a correct separation of the spine, commonly used for densitometry studies, as well as the identification of small calcifications or nodules down to 6 mm, reported to have a low rate of detection. The complete protocol to incorporate quantitative dual energy capabilities is based on a preliminary calibration with a very simple and low-cost phantom with no strict placement requirements. This avoids the need of the interaction of a radiologic technician with high expertise in the protocol, as it is the case in densitometry exams. The method provides real mass-thickness values allowing for quantitative studies.

Chapter 4

3D capabilities (I): Geometric calibration

4.1 Introduction

In systems designed for planar imaging, the relative positions between source and detector may vary significantly at each projection view leading to highly non-standard geometries. Even in systems with a geometry more similar to a CT, such as in the case of C-arms, non-circular standard trajectories are usually found by slipping the arm over the base.

These facts lead to different types of undesirable effects in the reconstructed image unless they are properly accounted for during the reconstruction. To obtain good quality images, it is necessary to have a complete characterization of the system geometry including the angular position of the gantry, the source-object and detector-object distances, and the position of the detector panel. These values can be obtained through a calibration process done periodically, depending on the stability of the system geometry.

Calibration algorithms designed for CT systems [Noo et al., 2000,Johnston et al., 2008] are based on the direct solution of a set of equations that describe the system geometry. The method described in [Noo et al., 2000] is robust, easy to implement and it is based on a simple object formed of two metallic spheres, but it assumes that the system is isocentric. All these approaches calculate global calibration parameters for all projections, thus they cannot be directly applied to more general scenarios.

Alternative methods have been proposed to generate the geometrical calibration of an imaging system projection by projection. The approach based on the so called "camera model" calibration [Rougee et al., 1993, Zhang and Navab, 2003] was first developed for artificial vision and it is based on mapping the 3D coordinates of an object to the 2D system from the projection image. A matrix projection is obtained experimentally through the image of a phantom formed by two markers with known geometry. This approach can be applied to scans with different trajectories but the calculation of these parameters from the matrix projection has shown instability [Yao et al., 2015] and does not provide the center of rotation, rendering it not suitable for tomography systems.

[Cho et al., 2005] proposed a method specifically designed to obtain calibration parameters of a cone-beam system individually for each projection, based on the acquisition of a simple phantom with two circular patterns. However, this work lacks both implementation details as well as a stable estimation of the inclination angles since it is based on a optimization problem assuming that one of them is always different to zero. Based on this work, we propose a new geometrical calibration method, which estimates all the parameters per-projection including the two inclination angles of the detector with respect to the horizontal and vertical directions independently.

This chapter presents: 1) a study of the effects of the geometrical inaccuracies for CBCT systems on the reconstruction quality by simulations, and 2) the description and evaluation of the proposed geometrical calibration method.

4.2 Effect of geometrical inaccuracies in reconstruction

We studied the effects on the reconstructed quality of the geometrical inaccuracies shown in Fig. 4.1: linear shifts (h-v offset), skew angle (η), and the inclination angles, pitch (θ) and roll (ϕ).

As reference image, we used a chest CT of the anthropomorphic phantom PBU-60 (Kyoto Kagaku) obtained with the Toshiba Aquilion/LB scanner with a voxel

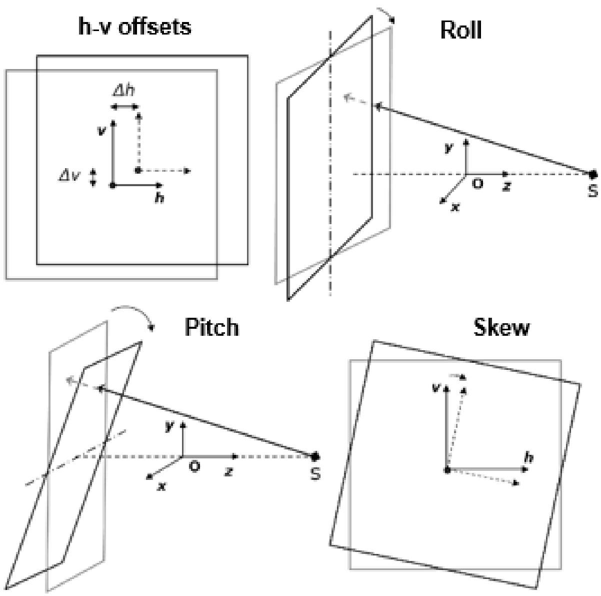

Figure 4.1: *Coordinate system and the geometrical inaccuracies in the detector panel.*

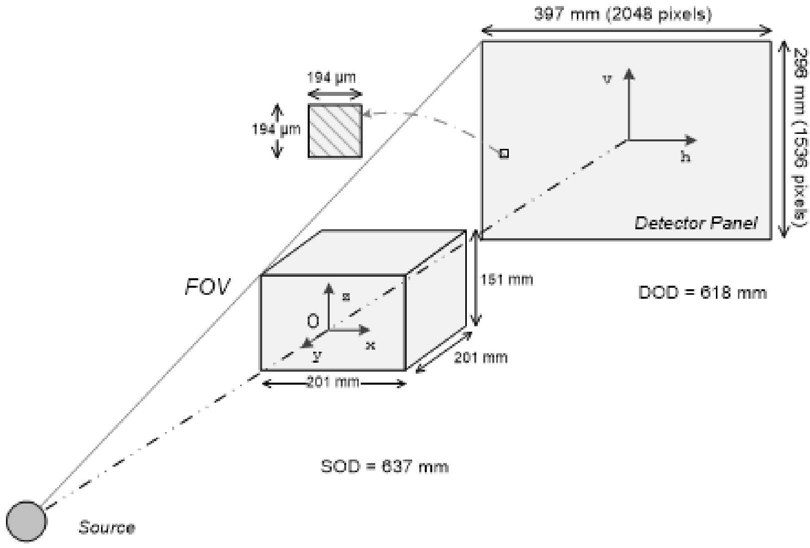

Figure 4.2: *C-arm geometry.*

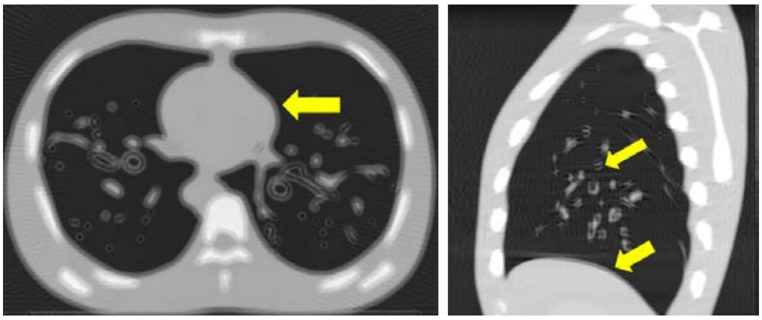

Figure 4.3: *Axial slice obtained with an h-offset of 2 mm (left), and sagittal slice obtained with an v-offset of 20 mm (right) of the anthropomorphic phantom. Yellow arrows indicate the double edges.*

size of 0.931 mm $\times$ 0.931 mm $\times$ 0.5 mm. From this, we simulated the geometry of the C-arm PowerMobil from Siemens Medical Solutions, shown in Fig. 4.2, which makes use of a flat panel detector (active matrix of 2048x1536 pixels, with a pixel size of 0.194 mm and a projection area of 40 $\times$ 30 cm^2 [Daly et al., 2008].

Five different datasets were simulated using FUX-SIM [Abella et al., 2017] with: 1) h-offset of 2 mm, 2) v-offset of 20 mm, 3) skew angle of 2 degrees, 4) pitch angle of 25 degrees and 5) roll angle of 8 degrees. All values of the different inaccuracies were selected high enough to detect visually their effects on the reconstructed images.

All datasets were reconstructed with an FDK-based method [Abella et al., 2012] without considering all the geometrical inaccuracies.

Left panel of Fig. 4.3 shows double edges in the whole image due to the horizontal offset. This effect is produced in all the views (axial, coronal and sagittal). Right panel of Fig. 4.3 shows an example of the doubles edges produced in the coronal and sagittal views due to the vertical offset.

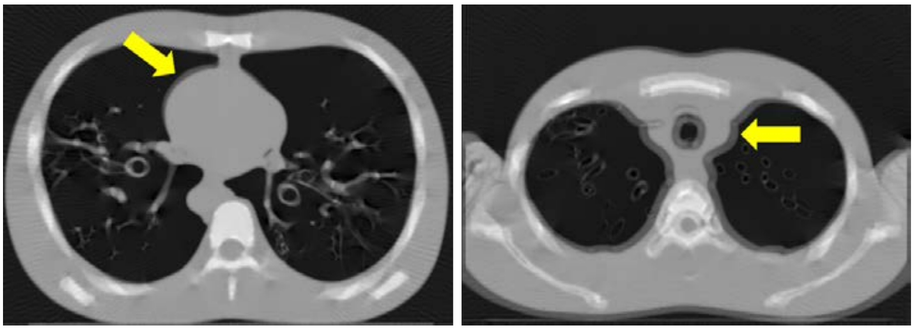

Figure 4.4: *Central slice (left) and slice further from the center of the FOV (right) obtained with a skew angle of 2 degrees. Yellow arrows indicate the double edges.*

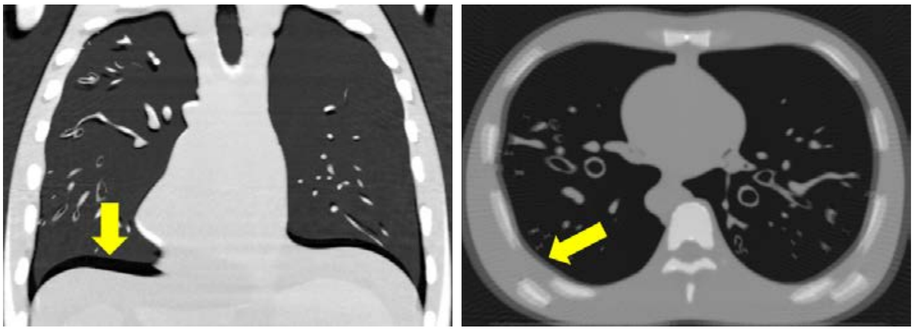

Figure 4.5: *Image difference between the coronal slice obtained with a pitch angle of 25 degrees and the reference image (left), and axial slice obtained with a roll angle of 8 degrees.*

Fig. 4.4 shows an example of the effect in the axial views of the skew angle, where double edges highly affect the image quality in axial views with dependence of the distance to the FOV center.

Fig. 4.5 shows an example of how the pitch angle produces distortion in the coronal and sagittal views. The roll angle also produces distortion but in axial views with dependence of the distance to the FOV center.

A more extended study of the effects in the reconstructed image by inaccuracies of the different parameters and a definition of their tolerance, understood as the maximum error to keep the image free from undesirable effects, can be found in [Abella et al., 2018]. This work presents a quantitative evaluation of the effects incorporated in both systematic and random ways. Fig. 4.6 summarizes the tolerances obtained for each geometrical parameter together with the type of undesirable effect and the views they are more noticeable.

	SYSTEMATIC ERRORS		RANDOM ERRORS	
	Effect on the image	**Tolerance value**	**Effect on the image**	**Tolerance value**
SDD changes systematic	Shape distortion in all views	18 mm	Double-edges in all views and streaks	9
SDD changes proportional	Double edges in all views	5 mm	-	-
Angular position	Rotation displacement in axial view	-	Double-edges in all views and streaks	0.25
Vertical shift	Double-edges in sagittal and coronal views and axial displacement proportional to vertical shift	6.984 mm	Double-edges in axial view and streaks	1.164
Horizontal shift	Double-edges in all views	0.543 mm	Double-edges and streaks in all views and streaks	0.776
Roll	Double-edges in all views	1.8 degrees	Double-edges in all views and streaks	2.5
Skew	Double-edges in axial view with dependence of the axial distance to the FOV center (value taken at 25% FOV from the center)	0.4 degrees	Double-edges in axial view and streaks	0.6
Tilt	Distortion in axial view with dependence of the distance to the FOV center (value taken at 25%FOV from the center).	10 degrees	Double edges in axial view (value taken at 25%FOV from the center) and streaks	21
	Distortion in coronal and sagittal views	8	Distortion in coronal and sagittal views and streaks	13

Figure 4.6: *Summary of geometrical tolerances.*

4.3 Proposed geometrical calibration algorithm

The calibration phantom is a PMMA cylinder with two circular patterns formed by ball bearings symmetrically embedded in the cylinder wall. Projections of the phantom should be obtained at the angular positions expected to be used in the specific trajectory during the acquisition of the sample. For each projection, the algorithm completes 6 steps: 1) identification of the position of the center of mass of ball bearings, 2) ellipse fitting, 3) determination of v-h offset, 4) determination of skew angle (η), 5) determination of converging point/inclination angles (θ and ϕ), and 6) determination of source and detector positions. An initial segmentation of the markers is achieved in a semi-automatic way using a calibration program with an interactive graphic user interface (Fig. 4.7), based on a global thresholding segmentation followed by morphological operations to remove artifacts. An initial threshold is estimated by Otsu's method [Otsu, 1979], but can be interactively adjusted by the user with a slider. Once the segmented markers are well identified, they are automatically classified into two sets (corresponding to each ring), according to their relative position with respect to the image center. To overcome the problem of overlapping markers, the tool allows the user to interactively correct the marker positions (place, remove or reposition), showing the updated ellipses overlaid onto the image in real time.

Following [Cho et al., 2005], ellipses are parametrized as:

$$a(h - h_0)^2 + b(v - v_0)^2 + 2c(h - h_0)(v - v_0) = 1 \tag{4.1}$$

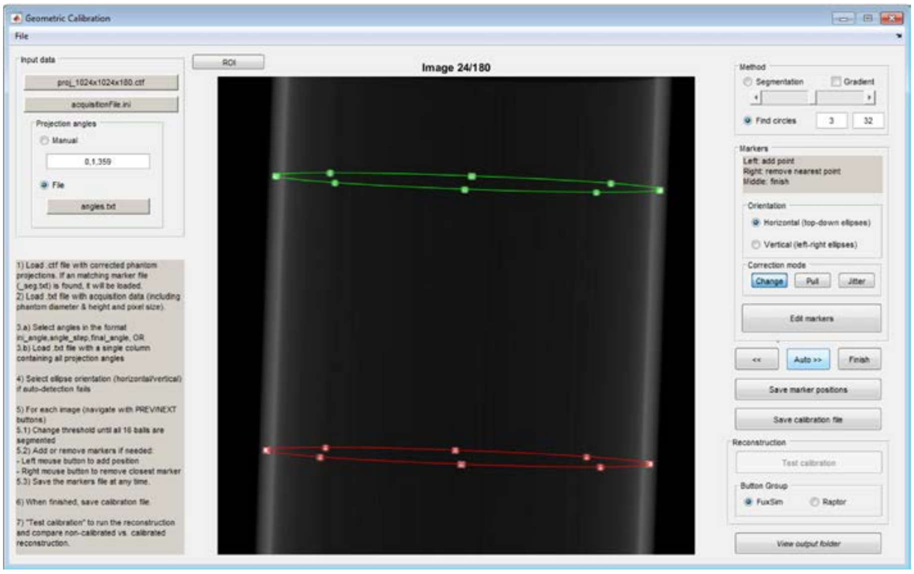

Figure 4.7: *System geometric calibration tool showing the ellipses for one projection of the calibration phantom.*

where (h_0, v_0) are the coordinates of the ellipse center and a, b, and c are parameters that describe its shape. To relate these parameters with the coordinates of the centers of mass of the balls previously obtained with the calibration program (h_b, v_b), we use the polynomial description of the ellipse:

$$p_0 h_b^2 + v_b^2 - 2p_1 h_b - 2p_2 v_b + 2p_3 h_b v_b + p_4 = 0 \tag{4.2}$$

where p_i are obtained solving the following system:

$$\begin{pmatrix} h_0^2 & -2h_0 & -2v_0 & 2h_0v_0 & 1 \\ \vdots & & & & \\ h_7^2 & -2h_7 & -2v_7 & 2h_7v_7 & 1 \end{pmatrix} \begin{pmatrix} p_0 \\ \vdots \\ p_7 \end{pmatrix} = \begin{pmatrix} -v_0 2 \\ \vdots \\ -v_7^2 \end{pmatrix} \tag{4.3}$$

Finally, we calculate ellipse parameters in equation 4.1 using the relations described by [Noo et al., 2000]:

$$h_0 = \frac{(p_1 - p_2p_3)}{(p_0 - p_3^2)}, v_0 = \frac{(p_0p_2 - p_1p_3)}{(p_0 - p_3^2)} \tag{4.4}$$

$$a = \frac{p_0}{(p_0h_0^2 + v_0^2 + 2p_3h_0v_0 - p_4)}, b = \frac{a}{p_0}, c = p_3 b \tag{4.5}$$

4.3.1 Determination of linear offsets

To calculate the possible horizontal and vertical displacements of the detector panel, known as h- and v-offset, we need to estimate the piercing point, that is, the projection of the center of the calibration phantom on the detector plane. To this end, we

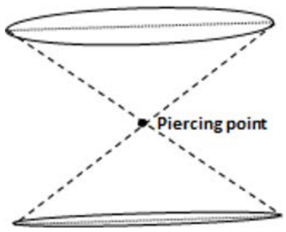

Figure 4.8: *Piercing point in the projection by the intersection of the lines.*

first find the opposite ends of mayor semi axis in both ellipses and then the intersection the lines that connect opposite points from the two circular patterns (Fig. 4.8). Then, the h- and v-offset are obtained from the difference between this point and the center of the image.

4.3.2 Determination of skew

The skew of the detector panel, η, is obtained using the equations that relate the radius of the short axis of the ellipses with the distance from point P_a (zero-short axis ellipse, produced by the projection of the central slice of the phantom) to the center of each ellipse, as described in [Cho et al., 2005]:

$$\eta = \frac{P_a^1 \cdot \tau_1 + P_a^2 \cdot \tau_2}{P_1^2} \tag{4.6}$$

where τ_i are the rotation angles of both ellipses, obtained from the parameters calculated before with the expression:

$$\tau = (1/2)acot\,(a - b/2c) \tag{4.7}$$

4.3.3 Determination of inclination angles

Regarding inclination angles, if both pitch angle, θ, and roll, ϕ, are zero, both ellipses have the same shape and their long axis are parallel, as shown in Fig. 4.9 (top, left). When θ is different from zero, one ellipse is lengthier than the other, as illustrated in the right panel of Fig. 4.9. The lines tangent to both ellipses converge to the pitch converging point, P_θ.

Since the calculation of both inclination angles in [Cho et al., 2005] is based on Pîÿ (Eq. 18 in [Cho et al., 2005]) pitch angle θ is assumed to be different from zero. To remove this restriction, we propose the following modification to the Cho method to estimate both effects separately.

The pitch angle is obtained from the geometric relationships:

$$\theta = asin\left[\frac{Z_s cos(\phi)}{v_\theta}\right], Z_s = \left[\frac{2RL_1L_2}{(H(L_2 - L_1)}\right] \tag{4.8}$$

where Z_S is the source distance, L_1 and L_2 are the distances between the two ellipses

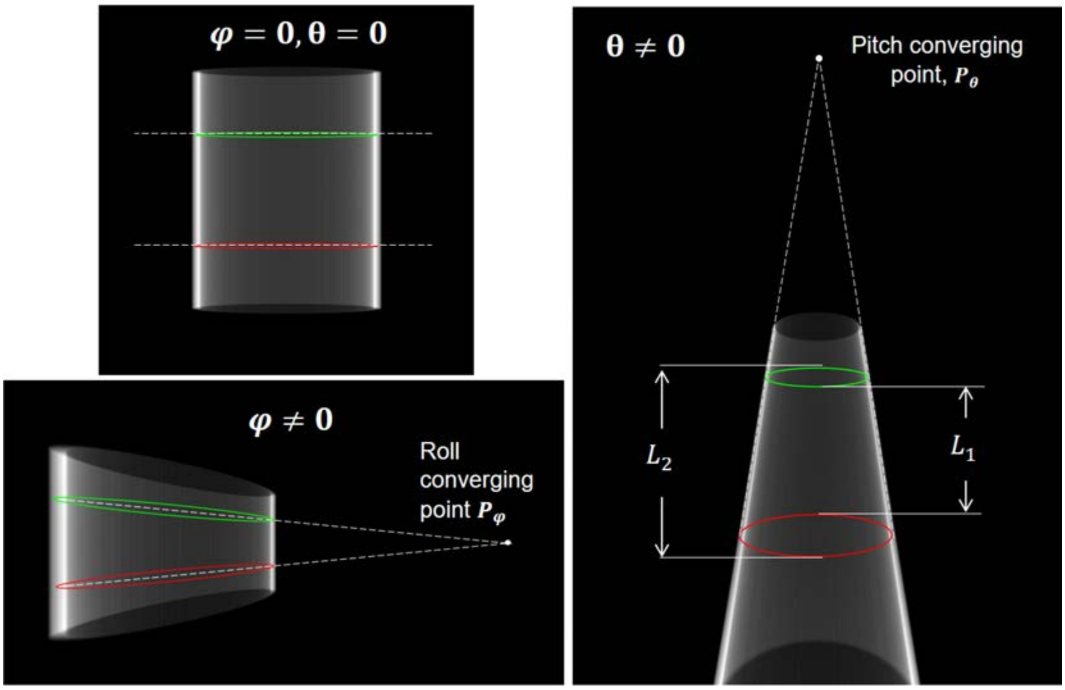

Figure 4.9: *Phantom projection for roll angle ϕ=60 degrees (left) and pitch angle θ=60 degrees (right).*

(Fig. 4.9,right), and R and H are the radius and the distance between the two circular patterns in the real phantom.

The roll angle is calculated by considering that, when ϕ is different from zero, the long axis of both ellipses converge to the roll converging point $P_\phi(h_\phi, v_\phi)$, as shown in the left-bottom panel of Fig. 4.9. Roll angle, ϕ, is obtained using the Nelder-Mead simplex method [Lagarias et al., 1998] to minimize the cost function C_ϕ:

$$C_\phi = sin(\phi) + c_1 \cdot \xi_1/2 \cdot (a_1) + c_2 \cdot \xi_2/2 \cdot (a_2) \tag{4.9}$$

where ξ_1 and ξ_2 are intermediate parameters for each ellipse given by:

$$\xi_k = \frac{T \cdot a_k \cdot \sqrt{a_k}}{\sqrt{a_k \cdot b_k + a_k^2 \cdot b_k \cdot (Z'_S)^2 - c_k^2}}, k = 1, 2 \tag{4.10}$$

with T given by

$$T = h_\phi \cdot sin(\phi) \cdot cos(\phi) \tag{4.11}$$

4.3.4 Evaluation

To evaluate the geometrical calibration proposed, we used a calibration phantom formed by a PMMA cylinder with height of 35 mm and diameter of 49.1 mm, with two circular patterns composed by ball bearings symmetrically embedded in the cylinder wall. We simulated five different datasets of the calibration phantom using

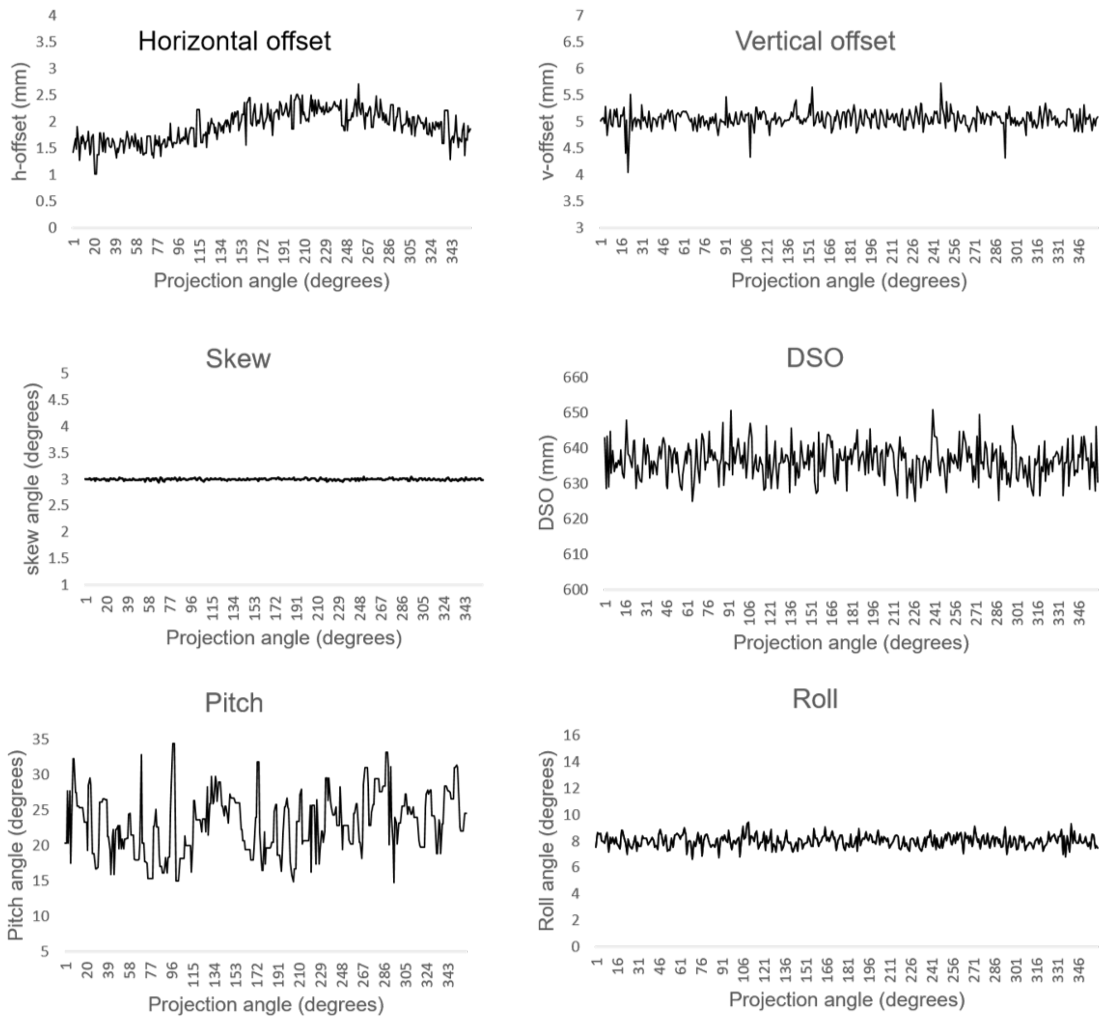

Figure 4.10: *Geometrical parameters obtained with the proposed calibration tool: .*

FUX-SIM [Abella et al., 2017] with: 1) h-offset of 2 mm, 2) v-offset of 5 mm, 3) skew angle of 3 degrees, 4) pitch angle of 6 degrees and 5) roll angle of 8 degrees.

Fig 4.10 shows all the estimated values along the different projection angles.

All the errors in the parameters estimation are highly below the tolerance found except the pitch angle, which is close to the tolerance in a few projections. Nevertheless, this parameter is the one that affects least the image quality.

4.4 Discussion

Regarding the effects on image quality, errors that affect the horizontal coordinate of the detector position, i.e. skew, roll and horizontal shift, are more restrictive than those affecting the axial direction, i.e. vertical shift and tilt. The effect of errors in skew and pitch has the particularity of varying their effect as a function of the distance to the center of the FOV while errors in angular position of the gantry, source-detector distance, roll and both shifts are constant across axial slices. Errors in skew, roll, horizontal shift, vertical shift result in double edges in the image. Errors in the vertical shift also result in a vertical displacement of the reconstructed sample proportional to the magnitude of the error, involving a reduction of the axial FOV. Errors in the detector panel tilt produce shape distortion.

The mentioned undesirable effects on the image resulting from geometrical inaccuracies in CBCT systems may have an impact on the quantification of the reconstructions, both in value and size of structures. These results could be used to guide the design of new systems, establishing the tolerances that have to be achieved by the mechanical devices together with the geometrical calibration process.

The proposed geometrical calibration method, based on the work of [Cho et al., 2005], estimates all the parameters per-projection: linear offsets, detector rotation (skew), inclination angles (pitch and roll), piercing point location (projection of the center of the calibration phantom), SDD (source to detector distance) and source and detector position.

The calibration procedure comprises the acquisition of a simple calibration phantom placed approximately in the center of the field of view. The method incorporates a semiautomatic segmentation step to avoid the problems of bearings superposition, and provides all the geometrical parameters needed to obtain a good quality reconstruction.

The intrinsic error of the calibration method is under the tolerance found for good quality images in all cases, which makes this proposal suitable in the incorporation of 3D capabilities in X-ray planar systems.

Chapter 5

3D capabilities (II): Limited-data reconstruction

5.1 Introduction

In conventional cone beam computed tomography (CBCT) systems, the source-detector pair rotates around the patient through 360 degrees (full angular span) to acquire generally more than 360 projections. However, there are cases in which the number of projections acquired is smaller and/or covers a smaller angular span due to movement limitations, as during surgery, or in multi-energy CT or in respiratory-gated CT, where only a few projections correspond to each source voltage or gate respectively. The reconstruction of these limited data implies an extremely ill-posed inverse problem and the use of conventional methods such as FDK results in severe artifacts in the image (streaks and/or edge distortion).

New advanced iterative reconstruction methods compensate for this lack of data by including prior assumptions, which can be included in the cost function to restrict the search space and help the method to find a better solution, as we mentioned in Chapter 1. One line of methods, the moment-based methods, such as [Dai et al., 2016], estimate the unknown projections by modeling with discrete Krawtchouk polynomials. When all the projections are available, they reconstruct them with FBP.

In some applications, these prior assumptions can be based on a preliminary reconstruction of a complete data set such as a previous scan in a longitudinal study. In respiratory or cardiac gating, the prior information may come from adding up data from all the phases [Abascal et al., 2016] and reconstructing it. However, in standard/static/single CT with limited-data this type of information is not available, thus being advisable to find a different prior. One option is to assume nonnegativity of the solution, $u > 0$, given that attenuation maps are always positive, or to restrict the problem considering only the possible solutions within the field of view. Another possibility is to assume that the human body presents homogeneous areas with similar X-ray attenuation properties, and therefore the solution will be piece wise constant. This fact can be by exploited considering that the gradient image should be sparse, containing only a few non-zero values corresponding to the edges and small details.

This prior assumption can be expressed as a quadratic function using the L_2 norm or using the L_1 norm (Fig. 5.1) as in the case of the Total Variation (TV) function [Rudin et al., 1992]:

$$TV(u) = ||\nabla u||_1 \tag{5.1}$$

The advantage of TV over quadratic norms is that it preserves the edges. Several works have exploited its use in limited-data X-ray tomography to assume local smoothness of the image [Sidky et al., 2006, Velikina et al., 2007, LaRoque et al., 2008, Duan et al., 2009, Matenine et al., 2015]. Nevertheless, this function is neither linear nor differentiable [Servent, 2013], what makes it more difficult to solve than the classical L_2-based optimization problems. Since TV minimization results in patchy images, other approaches have been proposed, such as reweighted TV [Chang et al., 2013], higher order TV [Debatin et al., 2013, Zhang et al., 2016] or the use of the wavelet domain [Rantala et al., 2006].

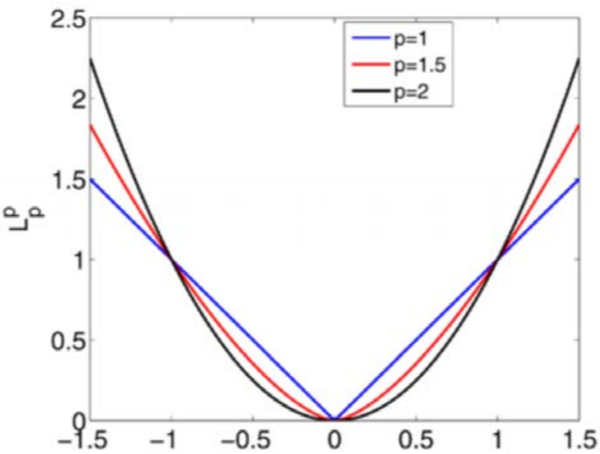

Figure 5.1: *L_p norms of 1D signal for p=[1,1.5,2]. Source: [Zhao et al., 2014].*

[Sidky et al., 2006] proposed a method that minimizes TV through the gradient descent algorithm. Following the same idea, [Velikina et al., 2007] filled the missing data points iteratively in the Fourier space, and [Duan et al., 2009] proposed an ART-TV scheme. In a more recent work [Matenine et al., 2015], authors combined a modified ordered subsets approach with the TV minimization. They optimized alternately the data fidelity and TV terms following the maximum log-likelihood and gradient descent algorithms for each problem. The main limitations of these methods are: 1) the data fidelity and the TV minimization are performed in two alternate steps separately, and 2) the convergency totally depends on the selection of the method parameters and the step size, which are generally found empirically.

Split Bregman-based algorithms redefined the L_1-cost function that assures a monotonic and fast convergence even when the cost function is not strictly convex neither differentiable, avoiding the strong dependency on the method parameters [Goldstein and Osher, 2009, Candes and Romberg, 2007].

5.1.1 Split Bregman algorithm for the solution of convex problems

Consider the following general optimization problem with the cost function composed by the combination of two convex one-dimensional functions:

$$u_0 \leftarrow \min_u E(u) + \mu H(u) \tag{5.2}$$

where $E(u)$ is a convex function defined over $\mathbb{R}^n$ beeing u the image vector (unknown), $H(u)$ is the penalty function, which is differentiable over $\mathbb{R}^n$, and μ the penalty parameter [Yin et al., 2008]. As we mentioned in Chapter 1, when the optimization problem is not well conditioned, a large value of μ is needed, which results in a strong dependency of the solution with the penalty parameter. Some works proposed different methods for its optimal finding through the L-curve [Hansen and O'Leary, 1993, Abascal et al., 2008].

To avoid the problems related with the penalty parameter, [Osher et al., 2005] proposed an alternative that modifies the cost function of Eq. 5.2 using the Bregman distance leading to:

$$u^{k+1} \leftarrow \min_u D_E^P(u, u^k) + \mu H(u) \tag{5.3}$$

where D_E^P corresponds to the Bregman distance [Bregman, 1967] which measures the closeness between two points, u_x and u_o of the function $E(u)$ and it is defined as:

$$D_E^P(u_x, u_o) = E(u_x) - E(u_o) - < p, u_x - u_o >, \quad p \in \partial E(u_o) \tag{5.4}$$

where p is the subgradient of E at the point u_0, as represented in Fig. 5.2. The Breg-

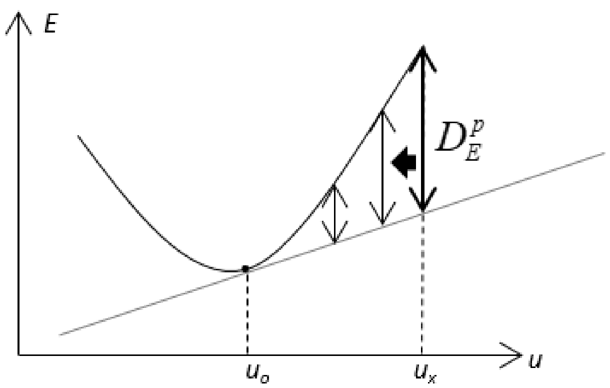

Figure 5.2: *Graphical representation of the Bregman distance*

man distance presents several properties [Burger, 2016] that help the optimal finding such as nonnegativity, asymmetry, linearity, and satisfies $D_E^P(u_x, u_o) \geq D_E^P(u_1, u_o)$ for an intermediate point u_1 between u_x and u_0.

The first iteration ($u^0 = 0\,, p^0 = 0$) of Eq. 5.3 is equivalent to minimizing the cost function in Eq. 5.2, and for the following iterations, different solutions are obtained after minimizing the Bregman distance between the current solution and the rest of the possible points (see Fig. 5.2).

After derivating the transformed cost function Eq. 5.3 and setting the result equal to zero, we obtain:

$$p^{k+1} = p^k - \nabla H(u^{k+1}) \tag{5.5}$$

where p are the subgradients given by:

$$p = \frac{\partial E(u)}{\partial u}, p^{k+1} \in \frac{\partial E(u^{k+1})}{\partial u} \tag{5.6}$$

The update of the subgradient, p^{k+1}, needed at each step, is known as the Bregman iteration (BI). Consider now that the function $H(u)$ corresponds to the quadratic norm of a data mismatch term, defined as:

$$H(u) = \frac{1}{2}||Au - f||_2^2 \tag{5.7}$$

The Bregman iteration (Eq. 5.5) is now:

$$p^{k+1} = p^k - A^T(Au^{k+1} - f) \tag{5.8}$$

The steps followed with this alternative are shown in Algorithm 4. The main advan-

Algorithm 4 Bregman distance minimization.

1: $u^0 \leftarrow 0, p^0 \leftarrow 0$
2: **for** $k = 0, ...$ **do**
3: $\quad u^{k+1} \leftarrow \min_u E(u) - E(u^k) - < p^k, u - u^k > + \frac{\mu}{2}||Au - f||_2^2$
4: $\quad p^{k+1} = p^k - A^T(Au^{k+1} - f)$
5: **end for**
6: **return** u

tage of this algorithm is its fast convergence because it is assured that the sequence of intermediate solutions u^k gets closer to the optimal solution u_0 monotonically in terms of the Bregman distance. Furthermore, no strict assumptions on E and H are needed for convergence such as strict convexity, differentiation or smoothness. It also avoids the strong dependency on the penalty parameter to converge. One limitation of this algorithm is the calculation of the subgradients at each step. To solve this, an equivalent version of Algorithm 4 was proposed [Osher et al., 2005, Yin et al., 2008, Goldstein and Osher, 2009] where the Bregman iteration is done through the update of $H(u)$, specifically updating f, shown in Algorithm 5.

At iteration $k = 0$, both algorithms solve the same minimization problem. For the rest k iterations, authors proved in [Yin et al., 2008] a theorem that states that both Bregman iterative procedures in Algorithm 4 and Algorithm 5 are equivalent

Algorithm 5 Equivalent Bregman distance minimization.

$u^0 \leftarrow 0, f^0 \leftarrow 0$
for $k = 0, \ldots$ **do**
  $u^{k+1} \leftarrow \min_u E(u) + \frac{\mu}{2}||Au - f^k||_2^2$
  $f^{k+1} = f^k + f - Au^{k+1}$
end for
return u

since they both have the same cost functions (up to a constant).

5.2 Limited-data iterative reconstruction method (LDIR)

We propose LDIR, a new iterative method for the reconstruction of limited-data that defines a cost function with two terms. One term corresponds to the data mismatch, imposed as a quadratic constraint, which states that the difference between the estimation and the data should be lower than the intrinsic data noise, ξ. The other term corresponds to the assumption of piece wise constant images through the exploitation of the total variation of the image:

$$\min_u TV(u) \ s.t. \ ||Au - f||_2^2 < \xi \tag{5.9}$$

where $TV(u)$ corresponds to the isotropic total variation:

$$TV(u) = \sum_i \sqrt{(\nabla_x u)^2 + (\nabla_y u)^2 + (\nabla_z u)^2} \tag{5.10}$$

Using the Bregman distance associated with the total variation of the image, Eq. 5.10 can be converted into the following sequence of unconstrained simpler problems [Osher et al., 2005]:

$$u^{k+1} \leftarrow \min_u D^{p^k}_{TV(u)}(u, u^k) + \frac{\mu}{2}||Au - f||_2^2 \tag{5.11}$$

$$p^{k+1} = p^k - \mu A^T(Au - f) \tag{5.12}$$

We use Algorithms 5 to solve Eqs. 5.11, 5.12:

$$u^{k+1} \leftarrow \min_u TV(u) + \frac{\mu}{2}||Au - f^k||_2^2 \tag{5.13}$$

$$f^{k+1} = f^k + f - Au^{k+1} \tag{5.14}$$

Eq. 5.14 is the Bregman iteration that imposes the constraint iteratively.

Given the non differentiability of the TV term, an auxiliary variable is incorporated to decouple the L_1 and the L_2 terms and solve them separately converting Eqs. 5.13 and 5.14 to:

$$\begin{aligned} (u^{k+1}, d_i^{k+1}) \leftarrow \min_{u,d_i} ||(d_x, d_y, d_z))||_1 + \frac{\mu}{2}||Au - f||_2^2 \\ subject\ to\ d_i = \nabla_i u,\ i = x, y, z \end{aligned} \tag{5.15}$$

We convert Eq. 5.15 to an unconstrained problem adding a penalty term for each constraint.

$$(u^{k+1}, d_i^{k+1}) = \min_{u,d_i} ||(d_x, d_y, d_z))||_1 + \frac{\mu}{2}||Au - f||_2^2 + \sum_i \frac{\lambda}{2}||d_i^k - \nabla_i u||_2^2 \tag{5.16}$$

Now, we can use the Bregman iteration leading to:

$$(u^{k+1}, d_i^{k+1}) = \min_{u,d_i} ||(d_x, d_y, d_z))||_1 + \frac{\mu}{2}||Au - f||_2^2 + \sum_i \frac{\lambda}{2}||d_i^k - \nabla_i u - b_i^k||_2^2 \quad (5.17)$$

$$b_i^{k+1} = b_i^k + \nabla_i u^{k+1} - d_i^{k+1} \quad (5.18)$$

Since variables u and d_i are not coupled, the problem 5.17 can be divided into two sub-problems. The first sub-problem contains only L_2-norm terms:

$$u^{k+1} = \min_u \frac{\mu}{2}||Au - f||_2^2 + \sum_i \frac{\lambda}{2}||d_i^k - \nabla_i u - b_i^k||_2^2 \quad (5.19)$$

which is solved following a classic approach, derivating and equating the result to zero.

$$\frac{\partial}{\partial u}\left[\frac{\mu}{2}(Au - f)^T(Au - f) + \sum_i \frac{\lambda}{2}(d_i - \nabla_i u - b_i)^T(d_i - \nabla_i u - b_i)\right] = 0 \quad (5.20)$$

After derivation and grouping we obtain the following linear system of equations:

$$\left(\mu A^T A - \lambda \sum_i \nabla_i^T \nabla_i\right) u^{k+1} = \mu A^T f^k + \lambda \sum_i \nabla_i^T (d_i^k - b_i^k) \quad (5.21)$$

which can be summarized in the following matrix-vector product system:

$$K u^{k+1} = rhs^k \quad (5.22)$$

where K is a matrix operator and rhs refers to the right-hand-side of the system. Eq. 5.22 is solved iteratively using a Krylov space solver, the biconjugate gradient stabilized method (BiCGSTAB) [Van der Vorst, 1992], described in Algorithm 6. The second sub-problem contains the L_1 term that is not differentiable:

$$d_i^{k+1} = \min_{d_i} ||(d_x, d_y, d_z))||_1 + \sum_i \frac{\lambda}{2}||d_i^k - \nabla_i u - b_i^k||_2^2 \quad (5.23)$$

Subproblem 5.23 is tackled analytically by a shrinkage formula [Goldstein and Osher, 2009], which is equivalent to a thresholding operation where the threshold value is given by $\frac{1}{\frac{\alpha}{\lambda}}$.

$$d_i^{k+1} = shrink\left(\sum_i \nabla_i u + b_i^k, \frac{\alpha}{\lambda}\right) \quad (5.24)$$

$$d_i^{k+1} = \frac{\nabla_i u^{k+1} + b_i^k}{s_i^k} max\left(s_i^k - \frac{1}{\lambda}, 0\right) \quad (5.25)$$

$$s_i^k = \sqrt{\sum_i |\nabla_i u^{k+1} + b_i^k|^2} \quad (5.26)$$

The complete LDIR algorithm to solve the total variation problem 5.10 is given in

Algorithm 6 BiCGSTAB.

procedure
  u^0 is an initial guess
  $r^0 = rhs - Ku^0$
  Choose an arbitrary vector $\hat{r}^0$, s.t. $< \hat{r}^0, r^0 > \neq 0$, i.e. $\hat{r}^0 = r^0$
  for $k \leftarrow iterations$ **do**
    $\rho_0 = \alpha = w^0 = 1$
    $v^0 = p^0 = 0$
    $\beta = (\rho^k/\rho^{k-1})(\alpha/w^{k-1})$
    $p^k = r^{k-1} + \beta(p^{k-1} - w^{k-1}v^{k-1})$
    $v^k = Kp^k$
    $\alpha = \rho^k / < \hat{r^0}, v^k >$
    $s = r^{k-1} - \alpha v^k$
    $t = Ks$
    $w^k =< t, s > / < t, t >$
    $u^k = u^{k-1} + \alpha p^k + w^k s$
    if u^k is accurate enough then quit;
    $r^k = s - w^k t$
  end for
  return u
end procedure

Algorithm 7.

Algorithm 7 LDIR

$u = 0, d_i^0 = 0, b_i^0 = 0, f^k = f$
while $||Au - f||_2^2 > \sigma^2$ **do**
  $\left(\mu A^T A - \lambda \sum_i \nabla_i^T \nabla_i\right) u^{k+1} = \mu A^T f^k + \lambda \sum_i \nabla_i^T (d_i^k - b_i^k)$
  $d_i^{k+1} = \frac{\nabla_i u^{k+1} + b_i^k}{s_i^k} max\left(s_i^k - \frac{\alpha}{\lambda}, 0\right)$
  $b_i^{k+1} = b_i^k + \nabla_i u^{k+1} - d_i^{k+1}$
  $f^{k+1} = f^k + f - Au^{k+1}$
end while
return u

5.3 Surface-Constrained Method for Limited-Data Tomography in CBCT Systems (SCoLD)

In scenarios with a low number of projections, together with a limited angular span, the proposed LDIR method may lead to severe distortions of the sample. To mitigate these distortions, the object contour has been proposed as prior information in other applications: Fluorescence Diffuse Optical Tomography [Correia et al., 2011], Fluorescence Molecular Tomography [Wang et al., 2014], Electron tomography [Gopinath et al., 2012], Multimodal Image Reconstruction [Kazantsev et al., 2014] and Object-based reconstruction [Gaullier et al., 2009]. However, the use of this prior for limited-view CBCT has not been yet explored.

We propose an extension of the LDIR method that includes the surface a-priori information of the sample, which we will refer to as surface support, restricting the search space.

We modify the problem 5.10 adding positivity and subspace constraints:

$$\min_u TV(u) \quad s.t. \quad ||Au - f||_2^2 < \xi, u \geq 0, u \in \Omega_s \tag{5.27}$$

where Ω_s is the subspace corresponding to the surface support. Since these two new constraints depend only on u, they can be incorporated into the first sub-problem in LDIR with only L_2 norm terms (Eq. 5.19) leading to the following:

$$u^{k+1} = \min_u \frac{\mu}{2}||Au - f||_2^2 + \sum_i \frac{\lambda}{2}||d_i^k - \nabla_i u - b_i^k||_2^2, \quad s.t. \quad u \geq 0, u \in \Omega_s \tag{5.28}$$

Eq. 5.28 is converted into an unconstrained problem using the concept of indicator function of a set C in $\mathbb{R}^n$ which is convex and defined as [Setzer et al., 2010, Abascal et al., 2011]:

$$\imath_C(x) = \begin{Bmatrix} 1, & if\ x \in C \\ 0, & otherwise \end{Bmatrix} \tag{5.29}$$

In our case, the set C for positive constraint and the surface support are defined as:

$$C_p = \{x \in \mathbb{R}^n | x > 0\} \tag{5.30}$$

$$C_s = \{x \in \mathbb{R}^n | x \in \Omega_s\} \tag{5.31}$$

Adding the two indicator functions Eq. 5.28 results as:

$$\begin{aligned} u^{k+1} = \min_u \frac{\mu}{2}||Au - f^k||_2^2 + \sum_i \frac{\lambda}{2}||d_i^k - \nabla_i u - b_i^k||_2^2 + \imath_{v \in \Omega_s} + \imath_{w \geq 0}, \\ s.t.\ v = u, w = u \end{aligned} \tag{5.32}$$

Using the Bregman iteration concept and adding the corresponding auxiliary variables, Eq. 5.32 can be replaced by:

$$\begin{aligned} u^{k+1} = \min_{u,d,v,w} \frac{\mu}{2}||Au - f^k||_2^2 + \sum_i \frac{\lambda}{2}||d_i^k - \nabla_i u - b_i^k||_2^2 + \frac{\gamma}{2}||v^k - u - b_v^k|| + \\ + \frac{\beta}{2}||w^k - u - b_w^k|| + \imath_{v \geq 0} + \imath_{w \in \Omega_s} \end{aligned} \tag{5.33}$$

$$b_v^{k+1} = b_v^k + u^{k+1} - v_i^{k+1} \tag{5.34}$$

$$b_w^{k+1} = b_w^k + u^{k+1} - v_w^{k+1} \tag{5.35}$$

Now, Eq. 5.33 can be split into four sub-problems. The first one is a quadratic problem that solves for u:

$$u^{k+1} = \min_u \frac{\mu}{2}||Au - f^k||_2^2 + \sum_i \frac{\lambda}{2}||d_i^k - \nabla_i u - b_i^k||_2^2 + \\ + \frac{\gamma}{2}||v^k - u - b_u^k||^2 + \frac{\beta}{2}||w^k - u - b_w^k||^2 \tag{5.36}$$

which can be solved derivating and setting the result to zero:

$$\Psi'(u) = \frac{\partial}{\partial u}\left[\frac{\mu}{2}(Au - f)^T(Au - f) + \sum_i \frac{\lambda}{2}(d_i - \nabla_i u - b_i)^T)(d_i - \nabla_i u - b_i) + \right] + \\ + \frac{\partial}{\partial u}\left[\frac{\gamma}{2}(v^k - u - b_u^k)^T(v^k - u - b_u^k) + \frac{\beta}{2}(w^k - u - b_w^k)^T(w^k - u - b_w^k)\right] \tag{5.37}$$

After derivation and grouping, we obtain the following linear system of equations:

$$\left(\mu A^T A - \lambda \sum_i \nabla_i^T \nabla_i + \beta I + \gamma I\right) u^{k+1} = \mu A^T f^k + \\ + \lambda \sum_i \nabla_i^T (d_i^k - b_i^k) + \gamma(v^k - b_v^k) + \beta(w^k - b_w^k) \tag{5.38}$$

which can be again summed up as:

$$Ku^{k+1} = rhs^k \tag{5.39}$$

Finally, Eq. 5.39 is solved as previously done in LDIR, with the biconjugate gradient stabilized method [Van der Vorst, 1992].

The second sub-problem [Setzer et al., 2010, Abascal et al., 2011] is:

$$v^{k+1} = \min_v \frac{\gamma}{2}||v^k - u - b_u^k||_2^2 + \imath_{w \in \Omega_s} \tag{5.40}$$

which is solved as:

$$w^{k+1} = \min_w \frac{\beta}{2}||w^k - u - b_w^k||_2^2 + \imath_{w \in \Omega_s} \tag{5.41}$$

The third subproblem is:

$$v^{k+1} = \max\left(u^{k+1} - b_u^k, 0\right) \tag{5.42}$$

which is solved as:

$$w^{k+1} = \begin{Bmatrix} u_j - b_{w_j}^k, & if\ u_j \in \Omega_s \\ 0, & otherwise \end{Bmatrix} \tag{5.43}$$

Finally, d_i is obtained from Eq. 5.23 by the shrinkage operation as in LDIR (Eqs. 5.24 and 5.25). The final solution of the reconstruction problem will be given by v instead of u as proposed in [Setzer et al., 2010].

The SCoLD algorithm to solve Eq. 5.27 is shown in Algorithm 8.

Algorithm 8 SCoLD

$u = 0, d_i^0 = 0, b_i^0 = 0, f^k = f$
while $||Au - f||_2^2 > \sigma^2$ **do**
  $(\mu A^T A - \lambda \sum_i \nabla_i^T \nabla_i)\, u^{k+1} = \mu A^T f^k + \lambda \sum_i \nabla_i^T (d_i^k - b_i^k) + \frac{\gamma}{2}||v^k - u - b_v^k||_2^2 + \frac{\beta}{2}||w^k - u - b_w^k||_2^2$
  $d_i^{k+1} = \frac{\nabla_i u^{k+1} + b_i^k}{s_i^k} max\left(s_i^k - \frac{1}{\lambda}, 0\right)$
  $v^{k+1} = max(u^{k+1} - b_v^k, 0)$
  $w^{k+1} = \left\{ \begin{array}{cc} u_j - b_{w_j}^k, & if\ u_j \in \Omega_s \\ 0, & otherwise \end{array} \right\}$
  $b_i^{k+1} = b_i^k + \nabla_i u^{k+1} - d_i^{k+1}$
  $b_v^{k+1} = b_v^k + u^{k+1} - v_i^{k+1}$
  $f^{k+1} = f^k + f - Au^{k+1}$
end while
$u = v^{k+1}$
return u

5.3.1 Visual explanation of SCoLD method

In this section, we present a visual explanation of the implementation of the SCoLD method showing the evolution of the intermediate solutions of the algorithm using an FDK reconstruction of a previous acquisition with an small-animal scanner [Vaquero et al., 2008]. We simulated a limited dataset using FUX-SIM [Abella et al., 2017] with 30 projections within an angular span of 90 degrees.

Fig. 5.3 shows the solutions u, d_x, v, relevant variables to understand the algorithm, $rhs, \nabla u$, and the Bregman iteration corresponding to the data fidelity constraint, f. For simplicity, we only show the x-direction variables but analogous results are obtained for y- and z-directions.

As we can see in Fig. 5.3, the K operator provides a smooth version of the rhs. At first iteration, $k = 0$, the solution u of Eq. 5.38 corresponds to the backprojection of the initial data, and for the following iterations, it progresses to an equivalent high-pass filtered version thanks to the incorporation of the Total Variation effect.

This TV effect is directly related with the solution d_x, given by the shrinkage operation. The output of the shrinkage can be understood as the edges and details (given by the derivative $\nabla_x u$), that will be included in the next iteration. The threshold parameter of the shrinkage should be set so that at the beginning this output should be zero and start appearing gradually from the fourth or fifth iteration. This can be controlled by the user with the α parameter considering the threshold as $\frac{\alpha}{\lambda}$. With this, the TV effect will be gradually incorporated both in solutions u and v.

All the auxiliary variables corresponding to the different constraints are updated iteratively. In Fig. 5.3, we can see how the variable corresponding to the data fidelity, f, presents more details and edges while increasing the number of iterations because it represents the difference between the new filtered estimation respect to the initial data and the previous estimation.

The final solution v is the same as u but limited by the surface support thus avoiding the distortions of the sample due to the limited-view.

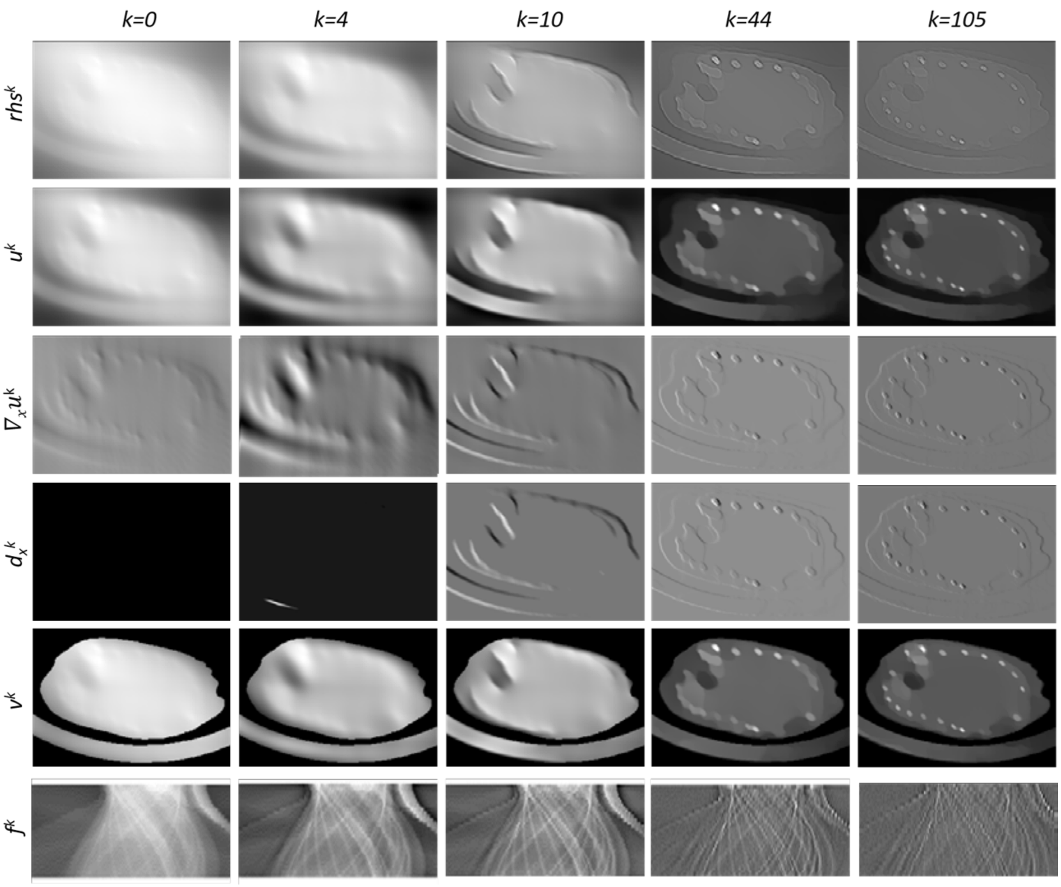

Figure 5.3: *From left to right: different intermediate results for iterations* $k = (0, 4, 10, 44, 105)$. *From top to bottom: relevant variables to understand the working of the SCoLD method.*

5.3.2 Study of SCoLD behavior

In this section, we present a study of the key aspects for any iterative algorithm: fast convergence and robustness against variations of the method parameters (μ, λ, γ and k). Also we explored its dependency with the number of projections and the angular span.

As reference image, we used the FDK reconstruction of a previous acquisition with an small-animal scanner, the Argus CT [Vaquero et al., 2008] (520×520 pixels; 0.125 mm pixel size) with 360 projections within 360 degrees. From this, we simulated limited datasets using FUX-SIM [Abella et al., 2017] with different $NumProjs$ uniformly distributed over different angular spans depending on the study.

All datasets were reconstructed with an FDK-based method [Abella et al., 2012] and SCoLD. For the latter, the surface support was extracted from the reference image through thresholding and morphological operations.

Image quality was assessed with the root mean square error (RMSE) between the reference image and the intermediate solution u_k from the limited dataset.

Convergence study

For the convergence study we used $NumProjs = 120$ within an angular span of 120 degrees. We reconstructed this data with $k = 200$ iterations varying λ, μ parameter, maintaining the theoretical relation described in [Goldstein and Osher, 2009], with $\lambda = (2, 10, 20, 40)$. We selected a large number of iterations, $k = 200$ to assure convergence in all limited-data configurations although a few number of iterations is enough for most cases.

Fig. 5.4 shows how error decreases monotonically for all λ and μ combinations reaching similar results, which is consistent with the theory [Goldstein and Osher, 2009].

When λ is very low ($\lambda = 2$), SCoLD is not stable. Regarding the rest of the cases, the lowest error is found when ($\lambda = 10, \mu = 5$). For these reasons, we select these parameter values for the following studies.

Fig. 5.5 shows a significant reduction of streak artifacts and the complete recovery of the external contour compared with FDK.

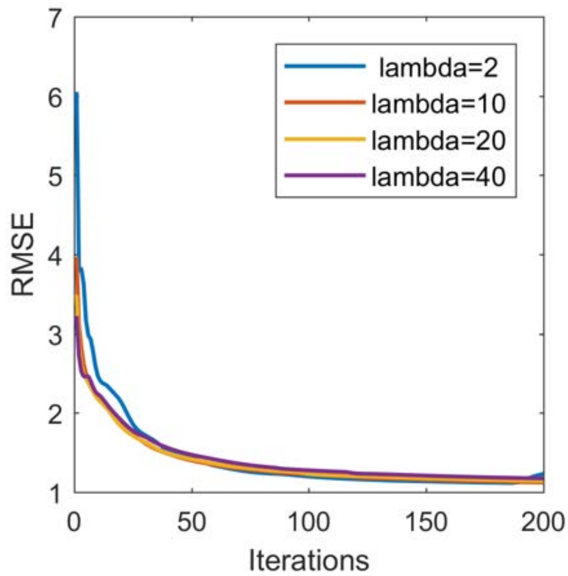

Figure 5.4: *RMSE between the reference and u^k with SCoLD method for different values of λ and $\mu = \lambda/2$.*

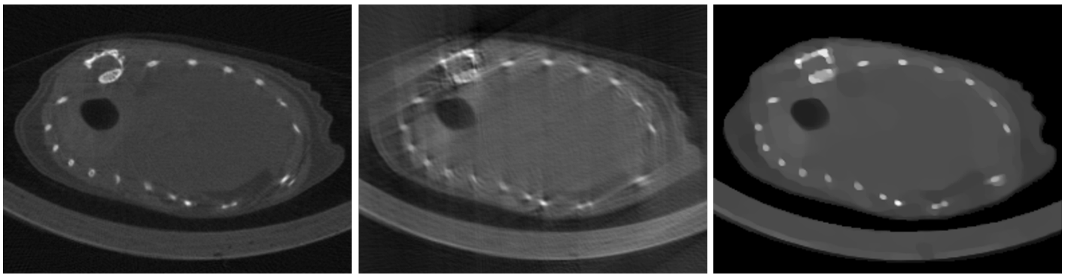

Figure 5.5: *From left to right: reference image, FDK and SCoLD reconstructions for 120 projections in an angular span of 120 degrees. Reconstruction parameters were:* $\mu = 5, \lambda = 10, \gamma = 0.01$ *and* $k = 200$ *iterations*

Study of robustness against variations of parameters

We have studied the effect of μ and γ varying both parameters as $\mu = (0.1, 0.5, 1, 5, 10, 20)$ and $\gamma = (0, 0.00001, 0.001, 0.1)$. We used $\lambda = 10$ for all the cases.

Fig. 5.6 shows that a minimum value of 0.5 for μ is needed to obtain an stable and monotonic behavior of the method and higher values of μ result in an faster convergence. Regarding γ parameter, for higher values than 0.1 the method does not converge. For the angular span of 120 degrees, the behaviour is similar to that of LDIR, that corresponds to $\gamma = 0$.

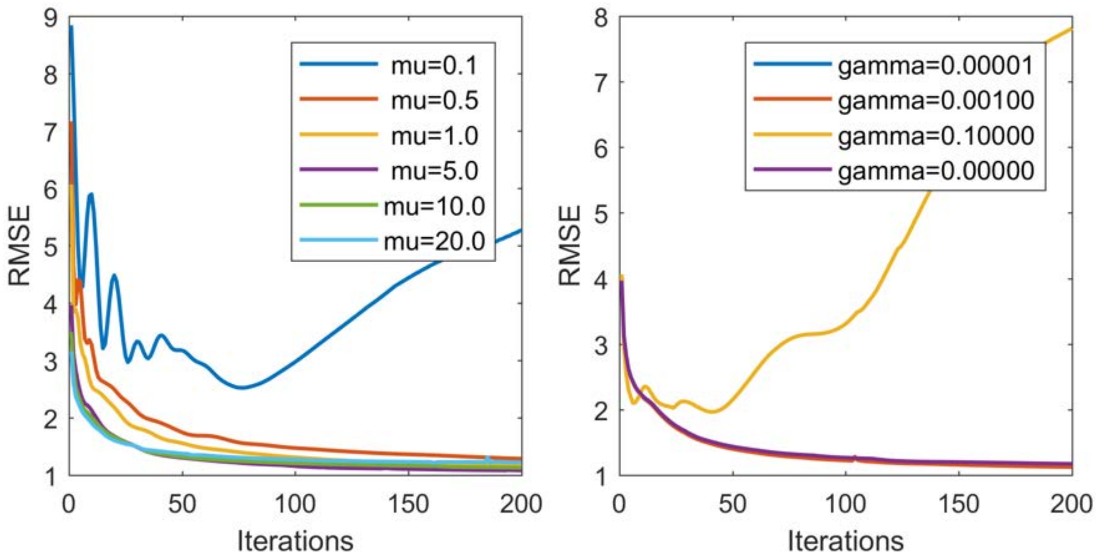

Figure 5.6: *RMSE between the reference and* u^k *with SCoLD method with* $\lambda = 10$ *varying* μ *(left) and* γ *with* $\mu = 5$ *(right).*

Study of robustness against different limited-data configurations

We study the effect of varying the total number of projections and the angular span simulating three different data configurations.

- $NumProjs = 120$ within an angular span of 120 degrees
- $NumProjs = 40$ within an angular span of 120 degrees
- $NumProjs = 120$ within an angular span of 90 degrees

All datasets were reconstructed using $\mu = 5, \lambda = 10, \gamma = 0.01, k = 200$.

RMSE plotted in Fig. 5.7 shows a lower error for the case of $NumProjs = 120$ over an angular span of 120 degrees. The three curves show a similar convergence behavior. We can see that reducing angular span results in a higher error compared with reducing the number of projections uniformly distributed in 360 degrees.

Fig. 5.8 shows a similar result when reducing the number of projections keeping the same angular span of 120 degrees. When reducing the angular span to 90 degrees, the external contour is not well recovered (yellow arrow in Fig. 5.8), which indicates that a higher value of the surface parameter, γ, is required.

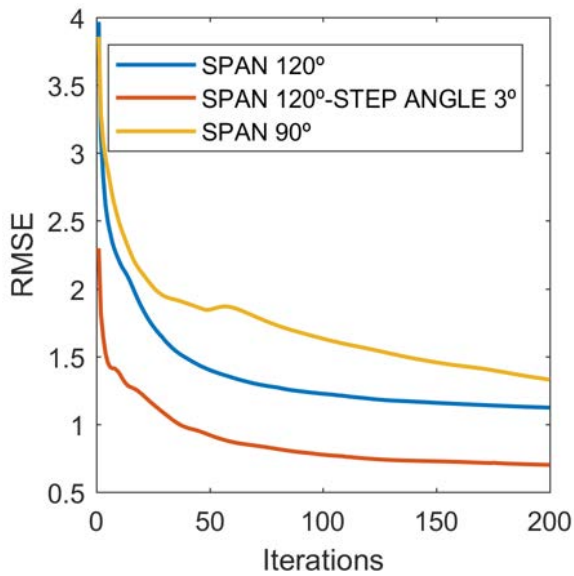

Figure 5.7: *RMSE between the reference and u^k with SCoLD method for the three different limited datasets using $\mu = 5, \lambda = 10, \gamma = 0.01$.*

Fig. 5.9 shows the RMSE when varying γ. For $\gamma = 0.003$, we obtained a monotonic decrease of RMSE with the number of iterations and lowest error. Right panel of Fig.5.9 shows a complete recovery of the external contour for this γ value.

From previous results, this value of γ is also suitable for the angular span of 120 degrees.

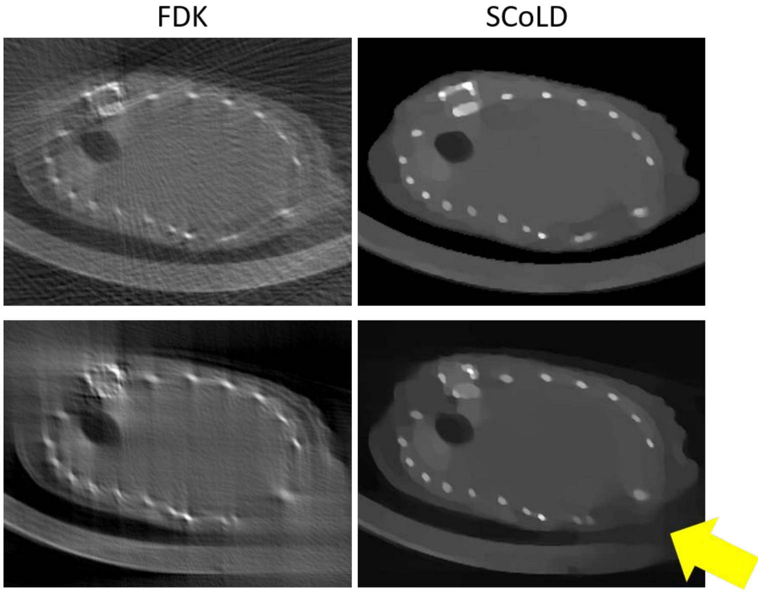

Figure 5.8: *Results for the limited data with 40 projections in an angular span of 120 ° (top) and for the case of 90 projections in a angular span of 90 ° (bottom) with* $\mu = 5, \lambda = 10, \gamma = 0.001, k = 200$ *parameters where the yellow arrow indicates the contour that it is not well defined.*

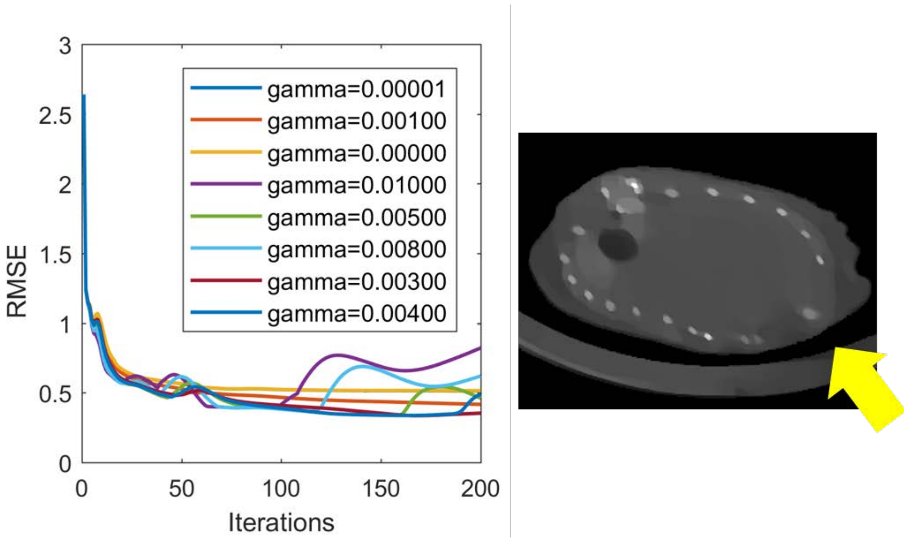

Figure 5.9: *RMSE between the reference and* u^k *for* $k = 1 : 200$ *for the limited data with 90 projections in an angular span of 90 degrees using the different* γ *values (left) and SCoLD reconstruction when* $\gamma = 0.003$ *where the yellow arrow indicates the well-defined contour (right).*

Comparison study of using different prior information

We have studied the benefits of the priors included in SCoLD as imposed constraints, starting from LDIR approach and adding sequentially the different priors:

- LDIR that includes only TV as assumption
- LDIR with positivity constraint ($u > 0$) as BI, named as "LDIR+"
- LDIR with support constraint as BI corresponding to the field of view ($u \in \Omega_{FOV}$), named as "LDIR-FOV"
- SCoLD that contains the constraints $u > 0, u \in \Omega_S$ as BI where Ω_S corresponds to the surface support

We simulated a limited dataset with $NumProjs = 30$ uniformly distributed over an angular span of 90 degrees. We used the optimum reconstruction parameters found in the previous section, $\lambda = 10,\ \mu = 5,\ \gamma = 0.003$. Fig. 5.10 shows a lower error for large number of iterations with SCoLD method, the only approach that includes the surface information. As we can see in Fig. 5.11 the support based on the FOV is not enough to recover the external contour and to eliminate the shape distortion when the angular span is reduced to 90 degrees.

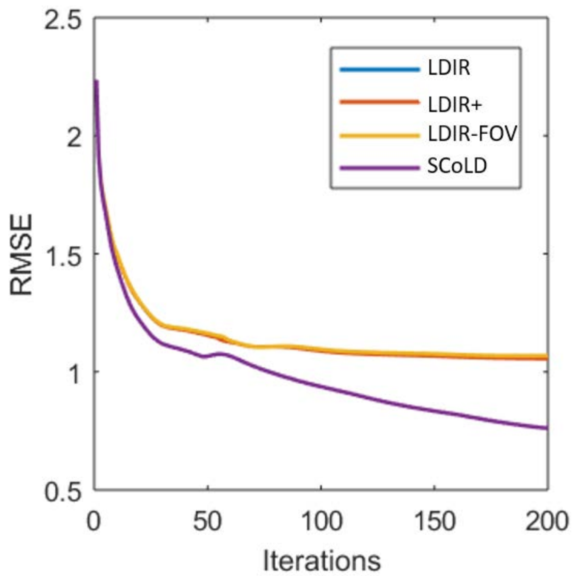

Figure 5.10: *RMSE between the reference image and the final reconstruction with the different reconstruction approaches studied.*

5.3.3 Recovery of density values and uniformity

We have studied the robustness of SCoLD against variations in sample size and heterogeneity with the three synthetic phantoms shown in Fig. 5.12: two homogeneous cylinders with density values corresponding to soft tissue (1 gr/cm^3) with diameters of 3.6 mm and 13.2 mm, and one heterogeneous phantom made of two cylinders of soft tissue and cortical bone (1.92 gr/cm^3) with diameters of 3.6 mm and 13.2 mm respectively.

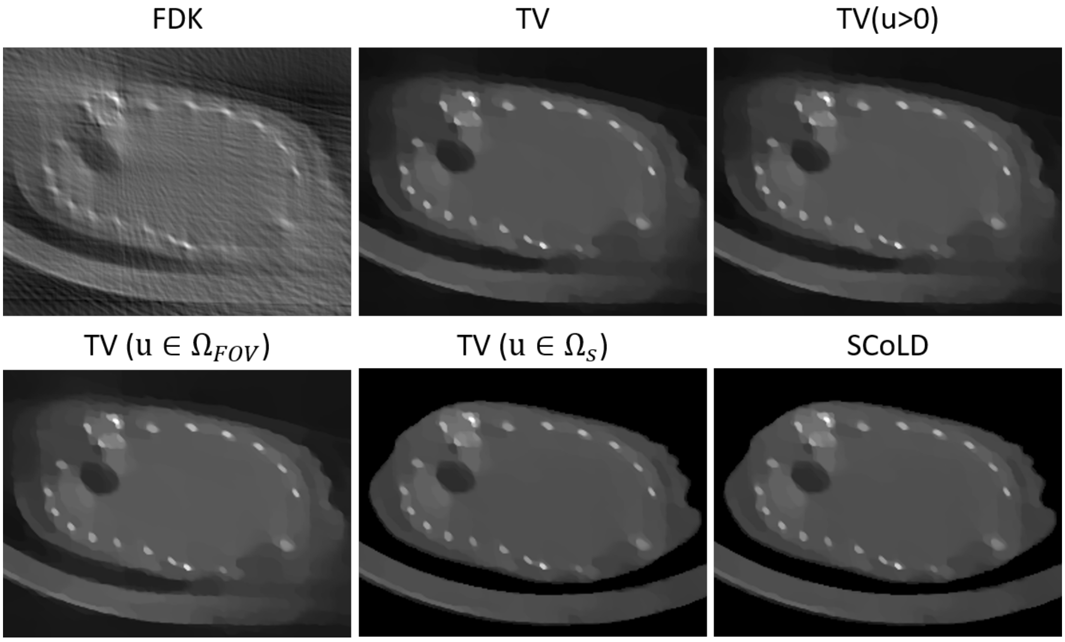

Figure 5.11: *Reconstructions of the limited data with 30 projections within an angular span of 90 degrees with FDK, LDIR, LDIR+, LDIR-FOV and SCoLD method.*

The simulated datasets with $NumProjs = 30$ over an angular span of 90 degrees, were reconstructed with FDK and SCoLD using the optimum parameters found in the previous section, $\lambda = 10, \mu = 5, \gamma = 0.003$. Central profiles in the reference (simulated phantom), FDK and SCoLD reconstructions were obtained.

Fig. 5.12 shows that SCoLD recovers not only the external contour but also all the edges in the internal structures (bone).

The central profiles (Fig. 5.13) shows that SCoLD recovers the uniformity in the three cases, lost in the FDK reconstruction. In all phantoms the density values with SCoLD are slightly higher than the ones of the reference image.

5.3.4 Optimization of the acquisition protocol

In this section, we study the optimum acquisition protocols for obtaining tomographic images with X-ray planar systems in terms of view angles, required number of projections and angular span.

As reference, we used the FDK reconstruction of three previous acquisitions with the Argus CT using 360 projections over 360 degrees, centered in three different anatomical regions: abdomen, head and thorax, shown in Fig. 5.14. The surface masks shown also in Fig. 5.14 were extracted from the reference images through thresholding and morphological operations.

Five different studies have been carried out in order to isolate possible different effects when acquiring, explained in Fig. 5.15:

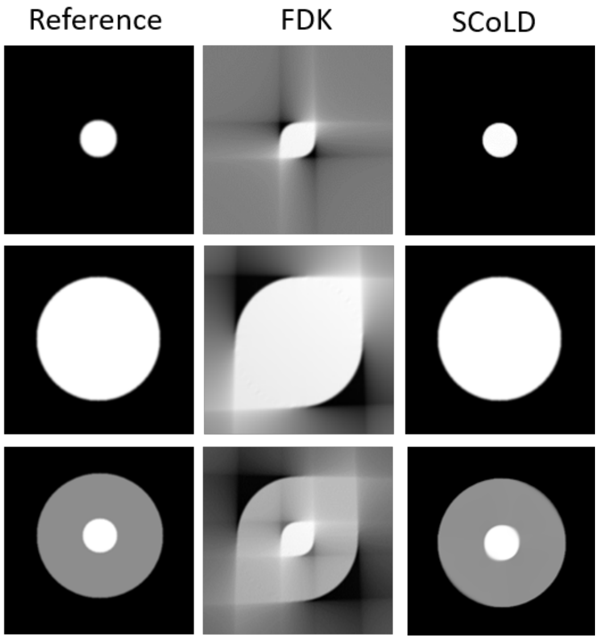

Figure 5.12: *Reference image, FDK and SCoLD reconstructions. From top to bottom: small cylinder (diameter of 3.6 mm), big cylinder (diameter of 13.2 mm) and heterogeneous phantom with soft tissue and bone cylinders.*

(a) To evaluate the angle views where most details and edges are parallel to the direction of the rays, we simulated limited data in the shaded area in green in Fig. 5.15 with an angular span of 90 degrees.

(b) To evaluate the acquisition in scenarios such as surgery where movement limitations are higher and the patient monitoring equipment may block the rotation, we simulated two sets of non-consecutive and symmetric projections separated by 90 degrees within an angular span of 45 degrees for each group, shaded area in blue in Fig. 5.15.

(c) To evaluate the angle views where most details and edges are perpendicular to the direction of the rays, we simulated limited data in the shaded area in orange Fig. 5.15 over an angular span of 90 degrees.

(d) To evaluate the effect of reducing the number of projections, we simulated two different datasets with $NumProjs = 45, 30$ over a fixed angular span of 90 degrees from oblique views to most details and edges.

(e) To evaluate the effect of reducing the angular span, we simulated different datasets with angular spans of 60, 90 and 120 degrees.

All limited datasets were reconstructed with FDK, LDIR and SCoLD. We used the selected reconstruction parameters, $\lambda = 10, \mu = 5, \gamma = 0.003, k = 200$.

Top panel of Fig. 5.16 shows the study (a) where most edges are parallel to the direction of the rays. Both LDIR and SCoLD methods reduce the streak artifacts in a

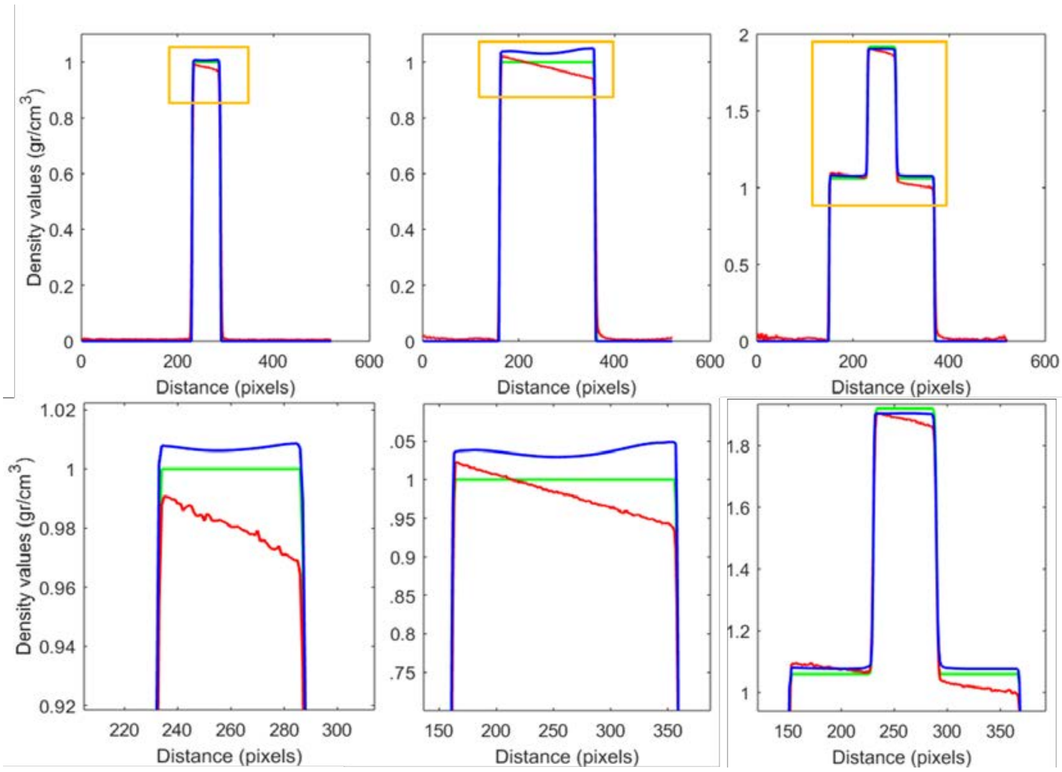

Figure 5.13: *Top: Central profiles of the reference image (in green), the reconstructions with FDK (in red), with SCoLD (in blue) of the small cylinder (left), big cylinder (center) and the heterogeneous phantom (right). Bottom: zoom-in of the profiles in the area under the orange square.*

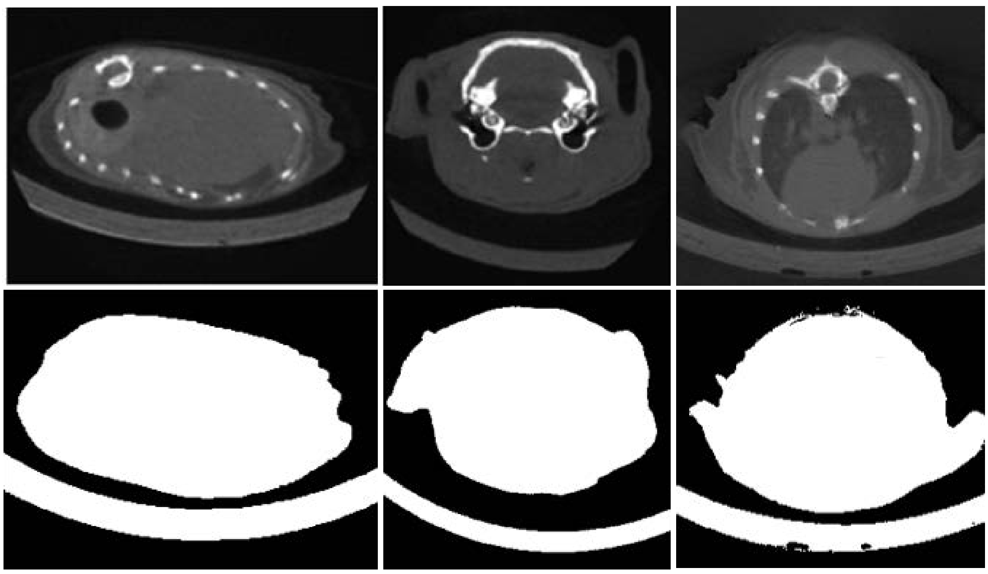

Figure 5.14: *Axial slice of abdomen (left), head (center) and thorax (right) studies. Bottom: surface masks extracted from the top studies by basic morphological operations.*

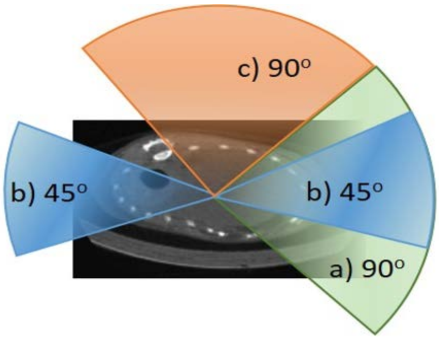

Figure 5.15: *Scheme of the scan protocols studied in cases (a), (b) and (c) with total angular span of 90 degrees while from different view angles.*

similar way but the contour and the details inside are better recovered with SCoLD. Bottom panel of Fig. 5.16 shows the results for the study (b) with data separated by 90 degrees in two groups. In this case, FDK reconstruction shows more streak artifacts and a more dramatic effect of distortion of the sample. SCoLD completely compensated both effects, while LDIR was not able to separate well the sample from the bed.

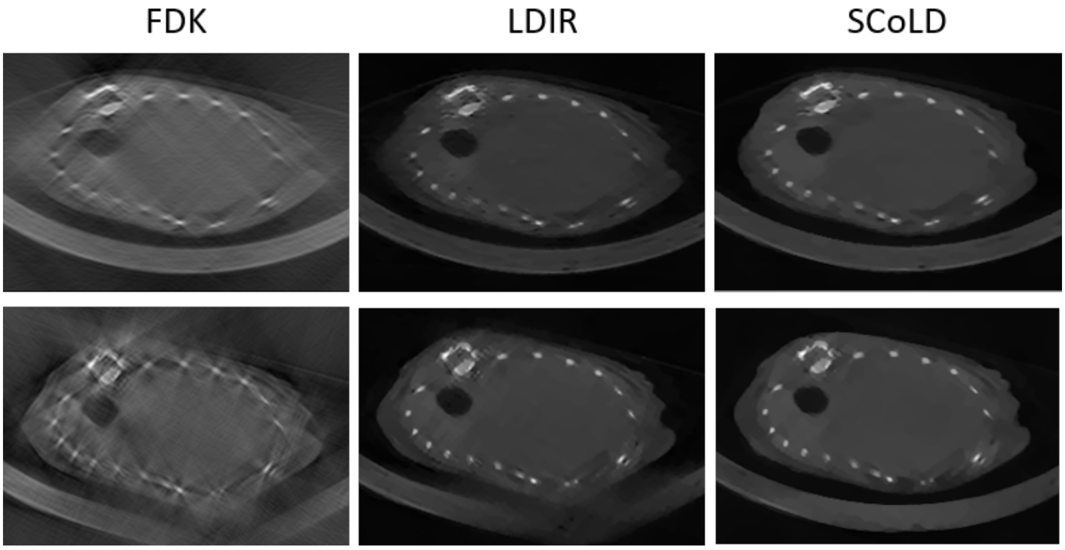

Figure 5.16: *Top panel: reconstructions of study (a) where most edges are parallel to the rays direction within an angular span of 90 degrees. Bottom panel: reconstructions of study (b) where 90 projections were acquired in two sets separated by 90 degrees. From left to right: FDK, TV-only and SCoLD method.*

Fig. 5.17 shows the study (c), where most details and edges are perpendicular to the rays direction for the abdomen, head and thorax regions. Image quality with SCoLD and LDIR methods is highly enhanced in terms of the definition of the bone details and the streaks reduction with respect to FDK but only SCoLD recovers the external contour. Nevertheless, details perpendicular to the direction of the X-rays are lost and it is not possible to recover them. Fig. 5.18 shows the effect of reducing

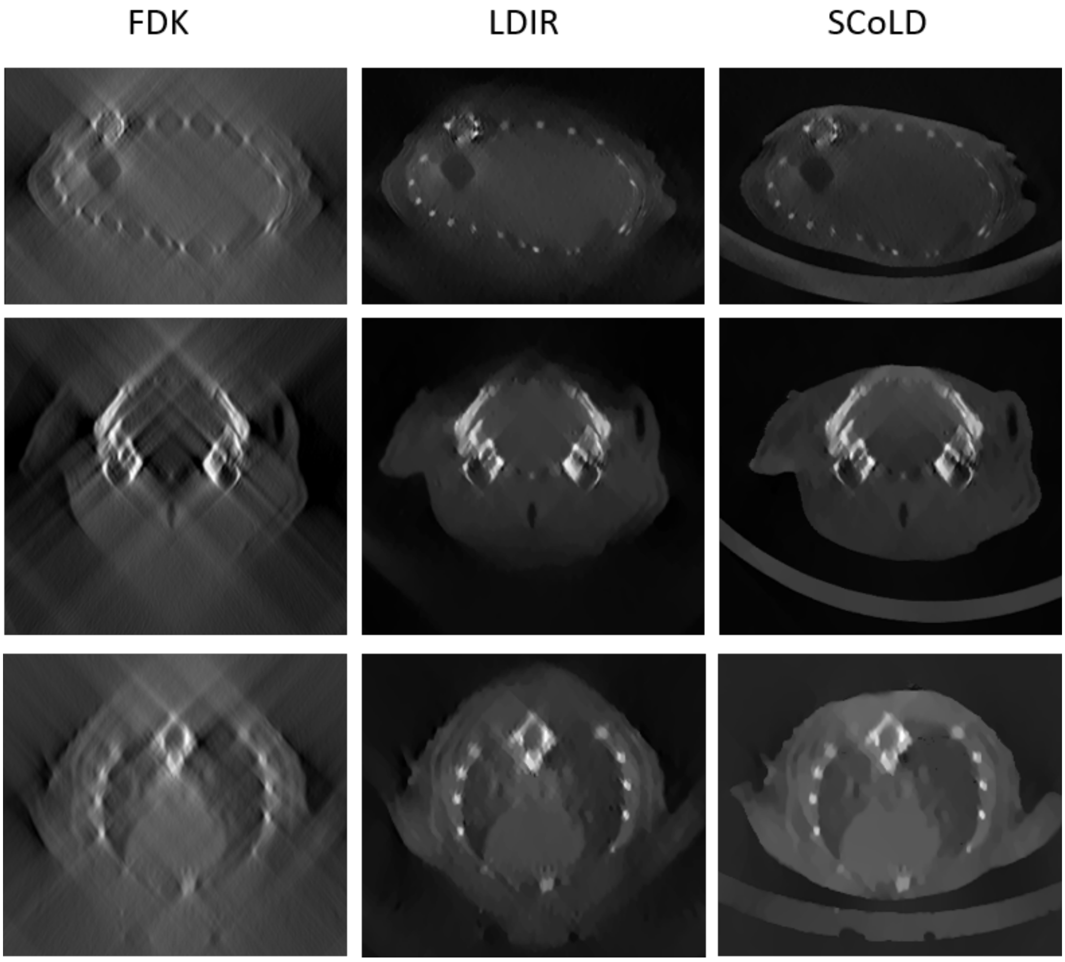

Figure 5.17: *Reconstructions of study (c) where most edges are perpendicular to the rays direction within an angular span of 90 degrees. From top to bottom: abdomen, head and thorax samples. From left to right: FDK, TV-only and SCoLD method.*

the total number of projections within an angular span of 90 degrees. For a given angular span, reducing the total number of projections has no effect on the quality of image when using SCoLD.

Fig. 5.19 shows that SCoLD obtained similar results compared with LDIR for high angular span (120 degrees). However, for the case with angular span of 90 degrees, the external contour perpendicular to the rays is only recovered with SCoLD. For the case with the lowest angular span, 60 degrees, LDIR does not compensate the external distortion unlike SCoLD.

In all protocols studied, SCoLD highly outperforms FDK, in terms of streaks reduction and external contour recovery. The higher restricted problem of SCoLD helps to obtain a better recovery compared with LDIR.

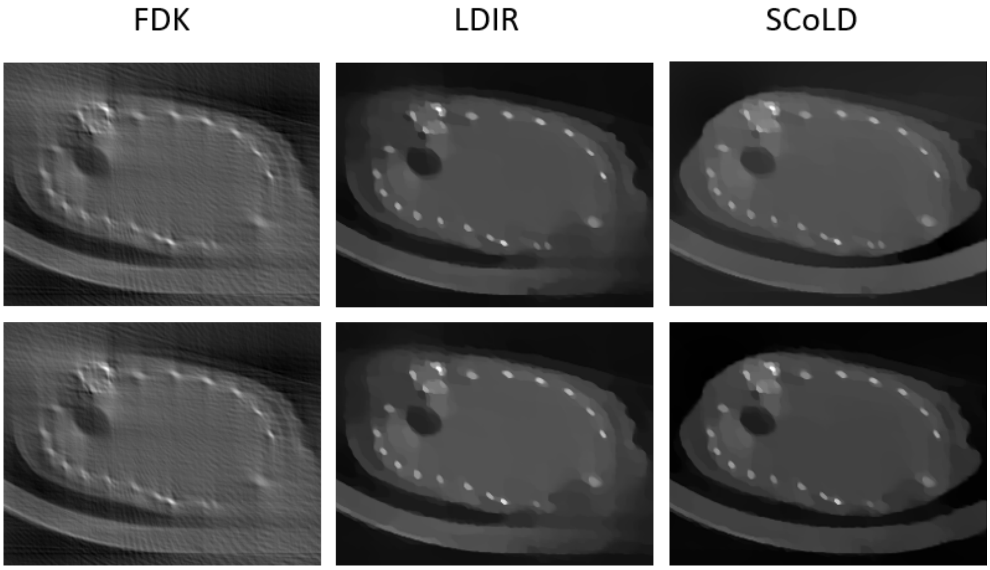

Figure 5.18: *Reconstructions of study (d) where the total number of projections is reduced within an angular span of 90 degrees. From top to bottom:* $NumProjs = 45, 30$.

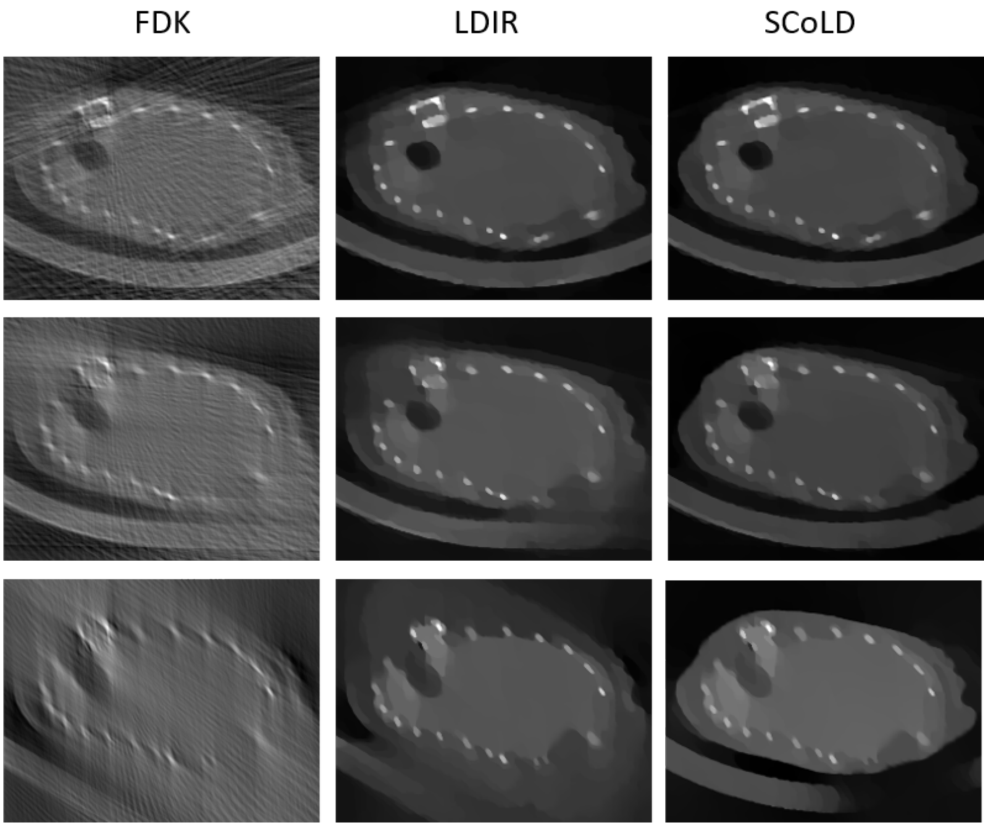

Figure 5.19: *Reconstructions of study (e) where the angular span is reduced. From top to bottom: angular span of 120, 90 and 60 degrees.*

5.4 Design of a modular and flexible implementation of SCoLD

In this section, we present a modular implementation allowing any geometry with flexible positioning of source and detector based on a cone-beam geometry, shown in Fig. 5.25. It allows including all the system geometrical parameters.

The accelerated implementation proposed, written in C and CUDA, is described in Algorithms 9, 10 and 11.

The modular design includes different modes (LDIR, SCoLD) depending on the input parameters. It is also possible to include different prior assumptions, such as the posivity constraint, the surface-based constraint, the FOV-based constraint, in addition to exploit different transformed domains such as TV or wavelet.

Fig. 5.20 shows the workflow of the mode corresponding to SCoLD.

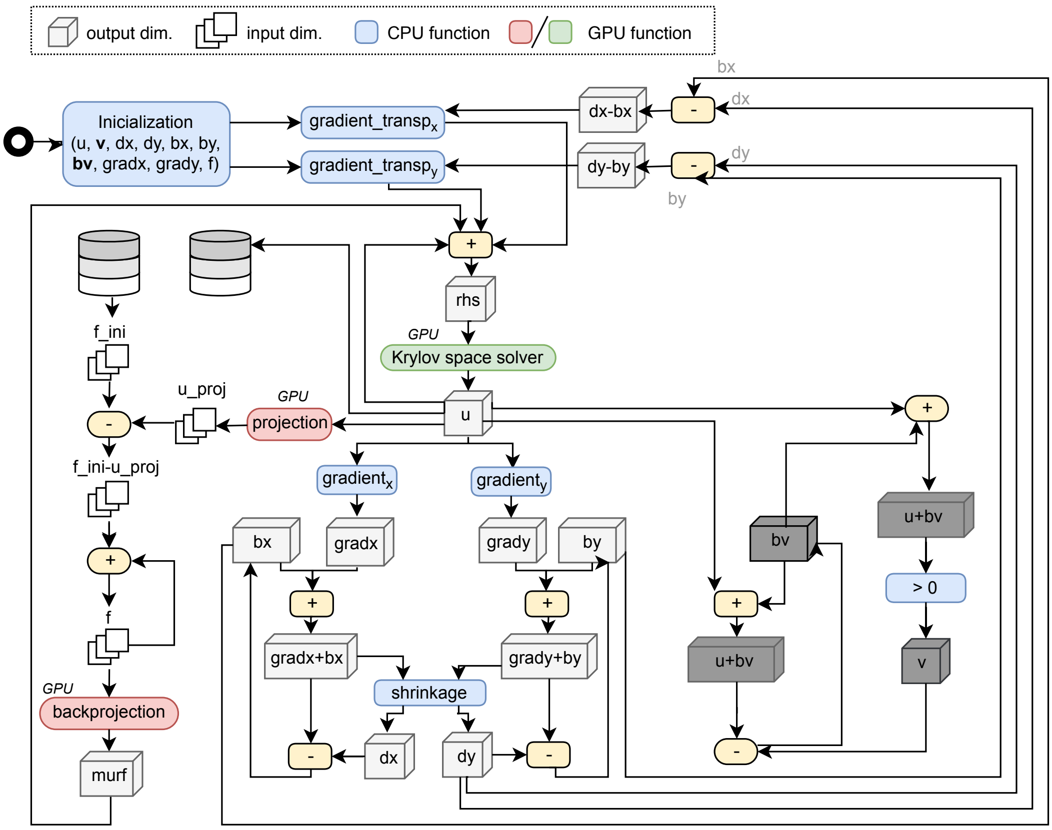

Figure 5.20: *Workflow of the SCoLD implementation.*

The system matrix A and its transpose are substituted by a ray-driven projector and a voxel-driven backprojector, which are applied at each iteration a variable number of times, depending on the convergence of the Krylov space solver. Given that those kernels represent the main computational burden of the method, we implemented them as accelerated kernels that run on GPUs. Other operations

Algorithm 9 Proposed modular implementation of SCoLD.

Input parameters
-*it*: <*algorithm_mode, FOV, T1,T2*>
-*algorithm_mode*: "0" (T1 only),"1" (T1 Prior Constraint)
-*FOV*: "0" (No), "1" (Yes)
-*T1,T2*: "0" (TV), "1" (Wavelet)
-*it_f*: path for prior (only for modes 1 and 2)
-*it_p*: input specific parameters in each mode
-*it_k*: <tolKrylov, iterKrylov>
-*it_s*: <iteration debugging>

LDIR-specific parameters
-*backNormFactor*: factor to compensate back/forward projection
-*threshold*: threshold for the shrinkage operation
-*tolKrylov*: convergence criteria
-*iterKrylov*: maximum number of internal iterations (Krylov)
-*mu*: weights the data fidelity term
-*lambda*: weights the Total Variation assumption

SCoLD-specific parameters
-*backNormFactor*: factor to compensate back/forward projection
-*threshold*: threshold for the shrinkage operation
âĹŠ*tolKrylov*: convergence criteria
-*iterKrylov*: Maximum number of internal iterations (Krylov)
-*mu*: weights the data fidelity term
-*lambda*: weights the Total Variation assumption
-*gamma*: weights the surface constraint
-*beta: weights the positivity constraint*

procedure RECOIT3D($f\_ini, FOV, prior, it_p arams, iterations$)
    Memory allocation for u,v,b,bv,d
    $f\_back \leftarrow backprojection(f\_ini)$
    $murf \leftarrow mu * f\_back * backNormFactor$
    for $k \leftarrow iterations$ **do**
        $rhs \leftarrow murf + lambda * (\sum Tt(d-b)) + gamma * (v - bv)$
        $u \leftarrow bicgstab(@jtjx, rhs, tolKrylov, MaxIter)$
        $Tu \leftarrow T(u)$
        $[d] \leftarrow shrinkage(Tu + b, threshold)$
        $v = max(u + bv, 0)$
        $v = v * prior, v = v * FOV$
        $b \leftarrow b + Tu - d$
        $bv \leftarrow bv + u - v$
        $u \leftarrow u * FOV > 0$
        $u\_proj \leftarrow projection(u)$
        $f \leftarrow f + f\_ini - u\_proj$
        $f\_back \leftarrow backprojection(f)$
        $murf \leftarrow mu * f\_back * backNormFactor$
    end for
    if algorithm_mode=0 || algorithm_mode=2 $u \leftarrow uBest$
    if algorithm_mode=1 $u \leftarrow vBest$
    return u
end procedure

Algorithm 10 Transform operation.

procedure T(T1 || T2)
  case 0 (TV)
    $dx = Dx(u)$
    $dy = Dy(u)$
    $Tu = [dx, dy]$
  case 1 (WT)...
  return Tu
end procedure

Algorithm 11 Transpose transform operation.

procedure TT(T1 || T2)
  case 0 (TV)
    $dxt = Dxt(u)$
    $dyt = Dyt(u)$
    $Ttu = [dx, dy]$
  case 1 (WT)...
  return Ttu
end procedure

that run on GPU are the gradients ($gradient_x$, $gradient_y$), the shrinkage operation ($shrinkage$), and the L_2-norm calculation (using CUBLAS library). The remaining element-wise operations are vectorized by the compiler [Agulleiro and Fernandez, 2010] and multi-thread CPU parallelized with OpenMP 4.0.

The Krylov space solver is implemented with the BiCGStab method, where the input matrix K in Eq. 5.22 is substituted by the Algorithm 12. Its worflow is represented in Fig. 5.21.

Algorithm 12 Callback function for Krylov space solver (BiCGStab).

procedure JTJX(sol)
  $gradsolx \leftarrow gradient_x(sol)$
  $gradsoly \leftarrow gradient_y(sol)$
  $bT \leftarrow lambda * \sum(Tt(T(solMat)))$
  $sol\_proj \leftarrow projection(sol)$
  $bFback \leftarrow backprojection(solMat\_proj)$
  $bF \leftarrow mu * bFback * backNormFactor$
  $Ksol \leftarrow bT + bF$
  return $Ksol$
end procedure

The division of the main problem into simpler sub-problems from the Split Bregman formulation results in the need for allocating up to ten times the memory corresponding to the desired output volume, resulting in a total memory footprint of several GB. Given GPU memory restrictions, we implemented a partitioning strategy

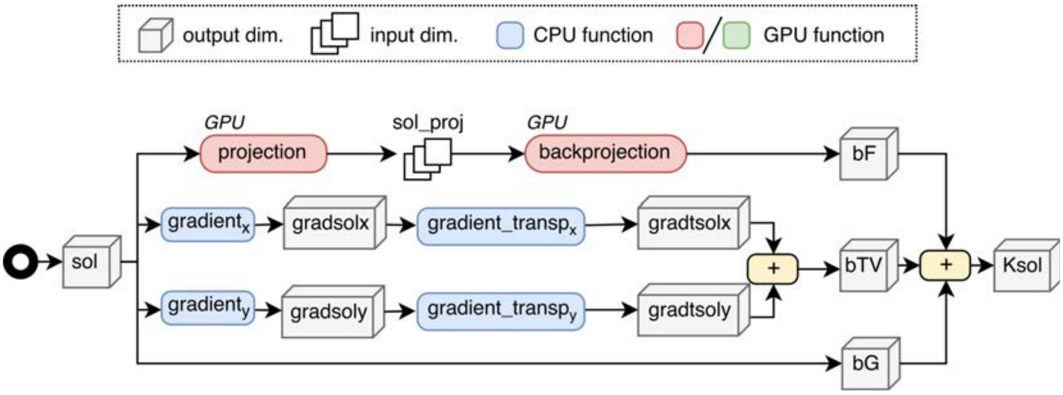

Figure 5.21: *Workflow of the Krylov space solver*

in both backprojection and projection operations, which are the ones that require the highest amount of memory. With this strategy, input and output data are divided into chunks, and the memory is allocated dynamically.

5.4.1 Backprojection and projection kernels

It is possible to set all the system geometrical parameters, described before in Chapter 4, as well as the deviations from the ideal position of the detector (offsets, skew, roll, and pitch in Fig. 5.25. Linear shifts (u_offset, v_offset) and skew angle (η) are applied by simple geometrical operations (shift or rotation of pixel coordinates):

$$\begin{pmatrix} x\_aux \\ y\_aux \end{pmatrix} = \begin{pmatrix} cos(\eta) & -sin(\eta) \\ sin(\eta) & cos(\eta) \end{pmatrix} \begin{pmatrix} x + u\_offset \\ y + v\_offset \end{pmatrix} \tag{5.44}$$

The effect of detector inclination (roll and pitch) is shown in Fig. 5.25, where ϵ is the inclination angle of the detector, A" is a pixel in the real detector, and A is the corresponding pixel in the ideal detector. For each point in the ideal detector, we can calculate the corresponding point in the real detector according to the expression

$$|PA'| = \frac{|PA|}{cos(\epsilon) + sin(\epsilon)\dfrac{|PA|}{DSO + DDO}} \tag{5.45}$$

Three different approaches were implemented: ray-driven, voxel-driven, and distance-driven. Ray-driven methods tend to introduce artifacts (Moiré patterns) in the backprojection, whereas voxel-driven projection introduces grid artifacts into the projections [De Man and Basu, 2002]. With more accurate geometric modeling, distance-driven methods often lead to better image quality than ray-driven projection and voxel-driven back-projection [De Man and Basu, 2004]. This is done by projecting voxel and detector boundaries into the same axis and calculating the overlap between them (Fig. 5.23), both for projection and for backprojection. Ray-driven and voxel-driven approaches rely on the computation of the trajectory corresponding to

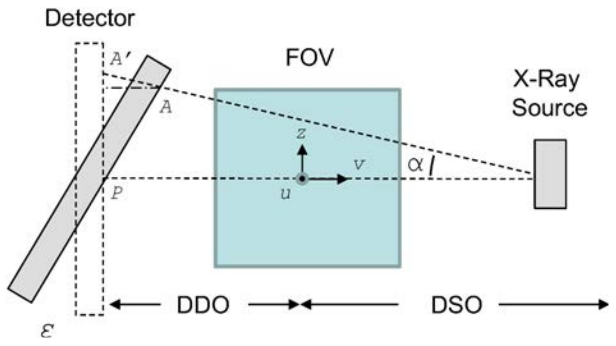

Figure 5.22: *The effect of detector inclination (roll and pitch).*

the center point of the voxel/pixel (black dot in Fig. 5.23 for the case of voxel-driven backprojection), whereas distance-driven mode aims to obtain a more accurate representation of the contribution to the voxel/pixel by computing trajectories for its limits (u_1 and u_2 in Fig. 5.23).

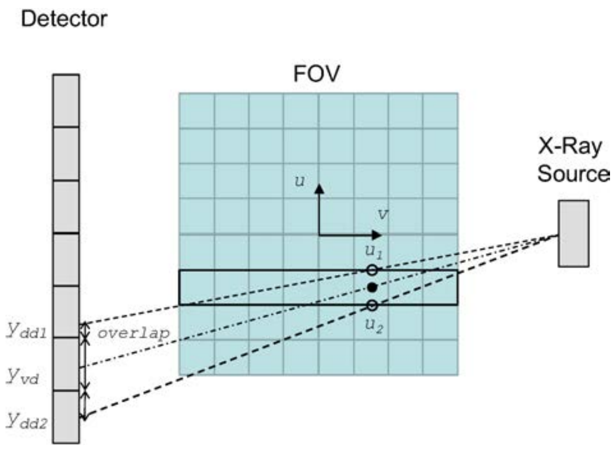

Figure 5.23: *Voxel-driven vs. distance-driven for backprojection. The contribution for the voxel (u,v) is calculated from the yvd value in the projection in the voxel-driven case and from ydd1 and ydd2 in the distance-driven case.*

Given that the kernels are the most time-consuming components, this layer is where most of the optimizations were made, including the full parallelization of the ray trajectories. We implemented two alternatives for projection and backprojection based on ray-/voxel-driven and distance-driven methods. Since each interpolation method needs a specific parallelization approach, we decided to implement two versions of each kernel in order to optimize performance.

The projection kernel emulates data acquisition in an X-ray system: the line integral is based on the computation of the sum of $Nstep$ values along the X-ray beam to update the contribution to the detector pixel:

$$p_\theta(x,y) = step \times \sum_{v_i=-\frac{rad}{step}}^{\frac{rad}{step}} \frac{1}{cos(\alpha)} f\left(\frac{1}{Mag} xcos(\theta + vsin\theta, \frac{-1}{Mag} xsin\theta + vcos\theta, \frac{1}{Mag} y\right) \tag{5.46}$$

where rad is the maximum radius of the FOV (in mm), $f(u, v, z)$ is the voxel value in the sample at coordinates (u, v, z), $p_\theta(x, y)$ is the projection data for position (x, y) in the detector at angle θ, α is the angle of the ray with respect to the central ray of the beam, and Mag is the magnification due to the cone angle, given by

$$\alpha = arctg \frac{\sqrt{x^2 + y^2}}{DSO + DDO} \tag{5.47}$$

$$Mag = \frac{DSO + v}{DSO + DDO} \tag{5.48}$$

where DSO and DDO are the distance from the center of the field of view (FOV) to the source and the detector, respectively (see Fig. 5.25).

Sampling is performed along the v-axis given by step (in mm), which is set by default to the minimum dimension of the pixel, covering $2 \times rad$. We include the term $\frac{1}{cos\alpha}$ to compensate for the higher sampling in rays that are distant from the central ray, as shown in Fig. 5.24 for the case of the ray that corresponds to y_1. The pseudocode in Algorithm 13 shows the projection kernel for both the ray-driven

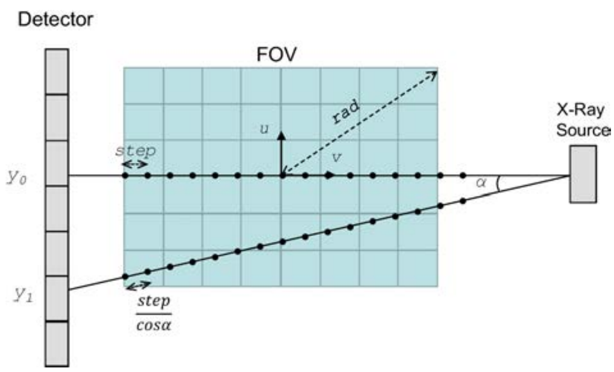

Figure 5.24: *Sampling scheme on the v-axis for the case of a non-isotropic voxel. y0 corresponds to the central ray. Sampling points are indicated with dots.*

algorithm (italic font) and the distance-driven algorithm (bold font).

The backprojection kernel implements the integral along all the angles of the result of spreading back the projection values (sometimes after filtering or other pre-processing steps) along each ray, according to the following equation (if all the

Algorithm 13 Projection kernel.

```
Data: volume, geometric parameters(uoffset, voffset, skew, tilt)
Result: projection data
for θ in NumProjs do
    for x in x_proj do
        for y in y_proj do
            Compute centered x coordinate in projection
            Compute centered y coordinate in projection
            Compute centered x1 and x2 coordinate boundary in proj
            Compute centered y1 and y2 coordinate boundary in proj
            if skew then
                Apply skew to (x,y) coordinates
                Apply skew to (x1,y1) and (x2,y2) coordinates
            end if
            if shift then
                Apply u- and/or v-offset to (x,y) coordinates
                Apply v- and/or y-offset to (x1,y1) and (x2,y2) coordinates
            end if
            for v in v_vol do
                Compute centered v coordinate
                Compute (u, v) rotated coordinates for θ angle
                Compute (u1, v) and (u2, v) rotated coordinates for θ angle
                Compute real so and do distances
                Compute inverse magnification factor:InvMag
                Obtain ideal u coordinate:InvMag×u_rot
                Obtain ideal z coordinate:InvMag×z
                Obtain ideal x1 and x2 coord:InvMag×u_rot1,2
                Obtain ideal y1 and y2 coord: InvMag×y1,2
                for x_i > floor(x1) and x_i<ceil(u2):
                  Compute contribution for x_i
                  for y_i >float(y1) and y_i<ceil(y2):
                  Compute contribution for y_i
                Update weighted value
                Trilinear interpolation
                Update projection position (θ, x, y) with computed value in
            end for
            Apply factor 1/cosα
        end for
    end for
end for
```

geometrical parameters are zero):

$$f(u,v,z) = \triangle\theta \cdot \sum_{\theta=ini}^{ini+nproj} p_\theta \left(Mag \cdot [ucos\theta - vsin\theta], Mag \cdot z\right) \qquad (5.49)$$

where ini is the initial projection angle, $nproj$ is the total number of projections, $f(u, v, z)$ is the value in the back-projected volume at coordinates (u, v, z), $p_\theta(x, y)$ the projection data for position (x, y) in the detector at angle θ, $\triangle\theta$ the step angle in radians, and Mag the magnification due to the cone shape of the beam given that

$$Mag = \frac{DSO + [usin\theta + vcos\theta]}{DSO + DDO} \tag{5.50}$$

where DSO and DDO are the distance from the center of the FOV to the source and the detector, respectively (see Fig. 5.25). The implementation of the backprojection kernel is shown in Pseudocode 2 for the ray-driven algorithm (italic font) and distance-driven algorithm (bold font).

The pseudocode in Algorithm 14 shows the backprojection kernel for both the ray-driven algorithm (italic font) and the distance-driven algorithm (bold font).

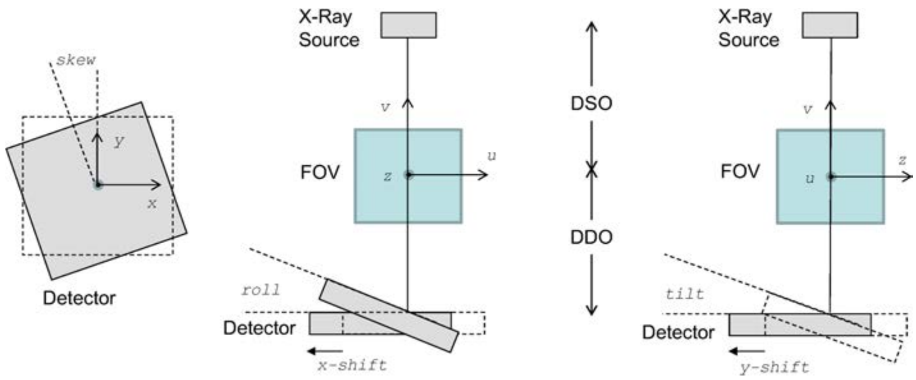

Figure 5.25: *Geometrical parameters used to parametrize deviations from the ideal position of the detector: offsets, skew, roll, and pitch.*

5.4.2 Time performance

The LDIR implementation was evaluated in a computer with two Intel(R) Xeon(R) E5-2630 v3 processors at 2.40 GHz and one NVidia Tesla K40c GPU. Limited-data acquisitions ($DimProj \times DimProj \times NumProjs$ pixels) were simulated from a previously acquired small-animal full scan (512 × 512 × 512 pixels; 0.125 mm pixel size). We studied the following parameters: dependency on the number of projections with $NumProj$ = 45, 60, 90, and 120 covering an angular span of 360 degrees and $DimProj$ = 512; dependency on angular span for $NumProj$ = 45 uniformly distributed in an angular span of 45, 60, 90, 135, 150, 180, and 270 degrees ($DimProj$ = 512); and the effects of the projection size, by considering $DimProj$ = 256, 512, and 1024 when 90 projections are obtained uniformly distributed in an angular span of 360 degrees. All simulations were generated using FUX-SIM [Abella et al., 2017].

These data were reconstructed with an FDK-based method [Abella et al., 2012] and the proposed iterative method resulted in a volume of $DimProj \times DimProj \times DimProj$ pixels. For the latter, we used α = 0.003, μ = 20, β = 3, and λ = 2 as

Algorithm 14 Backprojection kernel.

```
Data: projections, geometric parameters(uoffset, voffset, skew, tilt)
Result: volume data
for u in u_vol do
    for z in z_vol do
        Compute centered u and z coordinates
        Compute centered u1, u2 and z1,z2 boundary coordinates
        for v in v_vol: do
            for θ in projections: do
                Compute centered v coordinates
                Compute real so and do distances
                Compute u and v rotated coordinates for θ angle
                Compute u1,u2 and v rotated coordinates for θ angle
                Compute magnification factor
                Obtain ideal x and y coordinates
                Obtain x1,x2 and y1,y2 coordinates
                if shift then
                    Apply u- and/or v-offset to (x,y) coord
                    Apply u- and/or v-offset to (x1,y1) and (x2,y2) coord
                end if
                if pitch or roll then Apply tilt or roll to (x,y) coordinates
                    Apply tilt or roll to (x1,y1) and (x2,y2) coordinates
                end if
                if skew then
                    Apply skew to (x,y) cordinates
                    Apply skew to (x1,y1) and (x2,y2) cordinates
                end if
                for x_i > floor(x1) and xi < ceil(x2):
                  Compute contribution for x_i
                for y_i > float(y1) and yi < ceil(y2):
                  Compute contribution for y_i
                  Update weighted value
                  Bilinear interpolation
                  Store computed value in volume position (u,v,z)
            end for
        end for
    end for
end for
```

reconstruction parameters. The number of iterations was 35, selected high enough to ensure an error variation smaller than 1%.

Fig. 5.26 plots the dependence of the RMSE with the number of iterations, k, for six different limited-data cases varying the angular span and the number of projections. We can see that the proposed iterative method shows a similar behavior for all limited-dat

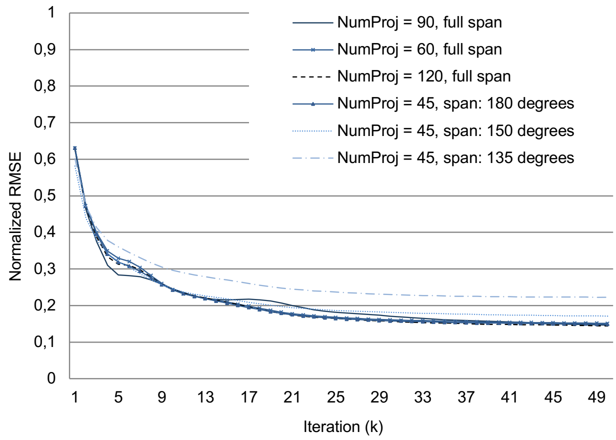

Figure 5.26: *RMSE vs. iterations for: 60, 90 and 120 projections (full span); angular span of 135,150 and 180 degrees (45 projections).*

Figs. 5.27, 5.2 … each
configuration, obt … r to
avoid time variab … ne is
divided into backp … ions
including I/O ope

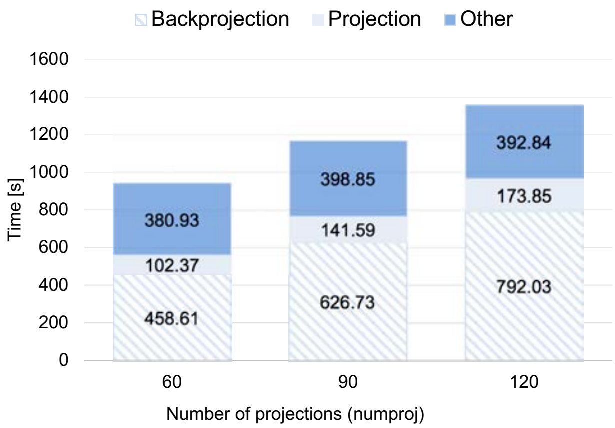

Figure 5.27: *Execution time (in seconds) for different number of projections.*

Finally, we compared our implementation in GPU of the iterative method with a CPU-only implementation of the same iterative method parallelized using OpenMP to fully exploit multi-core architectures. Figs. 5.30 and 5.31 plot the time spent in the first iteration (average of three different executions) reaching a speedup factor of 48× with the GPU implementation with respect to the CPU-only one.

Similar results were obtained with SCoLD, with an average increase of 0.06% of the total execution time compared with the LDIR method.

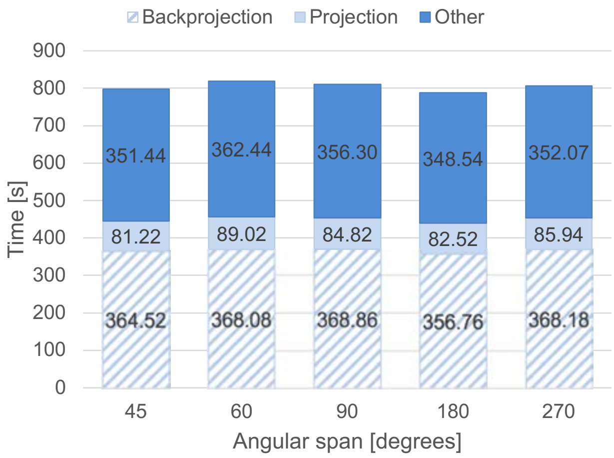

Figure 5.28: *Execution time (in seconds) for different angular span (degrees).*

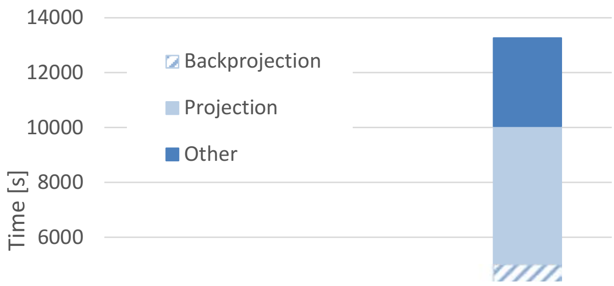

Figure 5.29: *I*

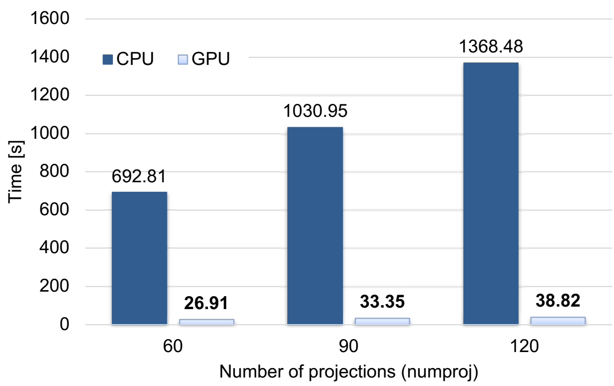

Figure 5.30: *Execution time (in seconds) of the CPU and GPU version of the TV method in the first iteration for different number of projections (NumProj).*

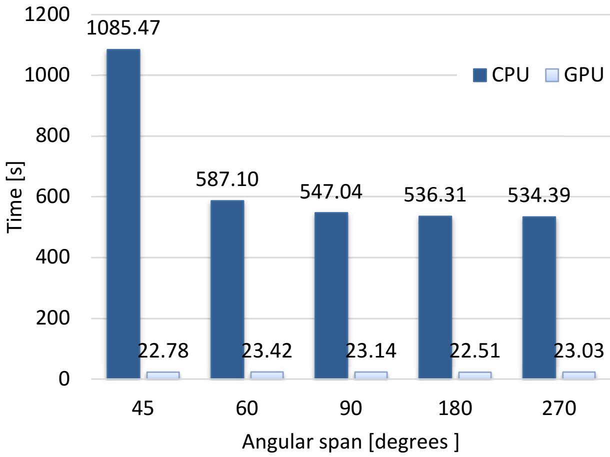

Figure 5.31: *Execution time (in seconds) of the CPU and GPU version of the TV method in the first iteration for different number of projections (NumProj).*

5.5 Discussion

We have proposed two advanced iterative methods for limited-data scenarios with X-ray planar systems. The first one, the limited-data iterative reconstruction method (LDIR), minimizes the TV of the image and imposes the data fidelity at the same time in an efficient way by following the Split Bregman formulation. This approach reduces the reconstruction problem to a sequence of simpler convex sub-problems where the intermediate solutions get closer to the optimum monotonically.

LDIR reduces significantly the streak artifacts produced in all limited-data configurations, similarly to previous proposals in the literature. However, in limited-view applications where the angular span is reduced, it may still lead to severe distortions of the sample. To solve this, we proposed an extension of the LDIR method, a novel iterative Surface-Constrained reconstruction method for Limited-Data tomography (SCoLD) that makes use of the surface information of the sample to compensate the lack of data. This information is incorporated as an imposed constraint, following also the Split Bregman formulation.

Evaluation of the SCoLD method showed fast convergence and robustness to variations of the method parameters, independently of the angular span or the number of projections. Both density values and the uniformity were recovered, independently of the sample, thus enabling quantitative studies. Its main advantage over previous works is that the restriction on the search space by exploiting the surface-based support results in a complete recovery of the external contour of the sample and surroundings, even for extremely reduced angular spans.

One limitation of both proposed methods is that TV may result in patchy-like artifacts in some cases. To mitigate this effect, advanced TV approaches have been proposed in the literature, such as reweighted TV [Chang et al., 2013] or higher order TV [Debatin et al., 2013, Zhang et al., 2016]. The reweighted TV method [Chang et al., 2013] modifies the conventional TV by a weigthted log-sum function that approximates better the L_0 norm than the L_1 norm with an adaptive weight that is updated iteratively. The higher-order TV approaches [Debatin et al., 2013, Zhang et al., 2016] preserve the edges thanks to the adaptive weighted TV term and suppress the staircase appearance with the second-order TV term. Both terms parameters have been chosen empirically [Debatin et al., 2013, Zhang et al., 2016] and they should be optimized.

In the same direction of improving the images texture, other approaches have proposed the use of of non local means filter [Huang et al., 2011, Chen et al., 2016] or other transformed domains such as wavelet [Rantala et al., 2006] or curvelet [Frikel, 2013]. The filter depends on the distance between patches and on a parameter h that controls the strength of the filter. An improved version was proposed in [Chen et al., 2016], where the parameter h is updated according to two more metrics, the average gradient and the region homogeneity, between patches.

The proposed implementation of SCoLD enables the use of flexible geometries incorporating the variations of all the geometrical parameters. Its modular design allows to create new reconstruction approaches easily adding more constraints formulated as Bregman iterations and exploiting other transformed domains such as wavelet or curvelet space. Its efficient implementation through GPU-accelerated kernels and partitioning strategies enables the reconstruction of large volumes ($>1024^3$ pixels) in a few minutes (with an acceleration up to 48 $\times$ compared to a CPU-only version). The execution time of the proposed implementation varies linearly with the number of projections and does not depend significantly on the angular span. The size of the input projections results in a quadratic increase in total computing time.

The study of the optimum acquisition protocols for limited-data scenarios using SCoLD, allowed us to identify some recommendations. Reducing angular span affects much more than the number of projections. SCoLD allows us to reduce the angular span down to 60 degrees thanks to the surface-based constraint. Results showed that it is possible to reduce the number of projections down to 33% over any angular span. In scenarios where movement limitations are more strict, such as operating rooms where patient monitoring equipment may block the system rotation, SCoLD can maintain the image quality when acquiring separated groups of projections, separated even 90 degrees. In general, it is desirable to acquire projections with rays tangent to most edges but it is recommended to optimize the scan views for each type of study.

Chapter 6

3D capabilities (III): Validation in real systems

In this chapter we present a whole protocol to obtain 3D imaging with planar X-ray systems, which combines the proposed geometrical calibration method (previously described in Chapter 4), and the novel SCoLD reconstruction method (presented in Chapter 5), able to deal with limited data from non-standard circular trajectories.

The calibration procedure comprises the acquisition of a simple calibration phantom placed approximately in the center of the field of view. Projections of the phantom should be obtained at the angular positions expected to be used in the specific trajectory during the acquisition of the sample. The built calibration phantom is a PMMA cylinder with two circular patterns of diameter 49.1 mm separated 35 mm, each one formed by eight ball bearings (with 0.8 mm of diameter) symmetrically located around the cylinder with internal and external diameters of 45.5 mm and 49.5 mm respectively (Fig. 6.1). The method incorporates a semiautomatic segmentation

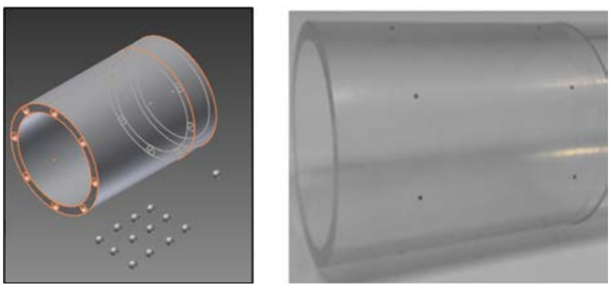

Figure 6.1: *Design of the calibration phantom (left) and real phantom (right).*

step to avoid the problems of bearings superposition, and provides all the geometrical parameters per-projection needed to obtain a good quality reconstruction.

In some cases, the exact position of the source and detector elements may not be repeatable for consecutive rotations due to low mechanical precision, thus we added a step of refinement of the parameters. This procedure, previously developed in the group and presented in [Ballesteros et al., 2018], uses a preliminary FDK reconstruction to orientate and adjust the surface support to the FOV of the system, by means of a 3D registration based on mutual information. The registered support is then projected using the initial calibration. The calibration parameters are finally updated based on the misalignments between the initial projections and the projected support.

The proposed implementation of SCoLD enables the reconstruction of limited-view data incorporating the variations of all the geometrical parameters. This method incorporates the surface information, which can be extracted with a 3D light surface scanner, as an imposed constraint.

For the evaluation of the protocol, we used one hand and one foot of a PBU-60 anthropomorphic phantom (Kyoto Kagaku Co., Kyoto, Japan). Both phantoms were acquired beforehand in a Toshiba Aquilion/LB helical scanner and reconstructed as a CT volume of 512×512×1645 voxels (used as reference image), with 0.931×0.931×0.5 mm pixel size.

The whole protocol was tested on two different C-arm devices: a commercial C-arm based on an image intensifier (SIREMOBIL, SIEMENS) and an in-house C-arm prototype based on a flat panel detector.

All datasets were reconstructed with the FDK-based method [Abella et al., 2012] and with SCoLD to evaluate the performance of the proposal. The low number of projections (60, 49 and 25), and the angular span (120 degrees) used in the real experiments were selected considering the previous study on their optimization (Chapter 5).

6.1 Evaluation with C-arm Model Siremobil

The C-arm Model SIREMOBIL Compact L of Siemens consists of an X-ray source and a 23 cm-diameter image intensifier attached to a C-arm gantry. The detector of the SIREMOBIL system is an X-ray image intensifier (XRII) connected to a TFT monitor for image visualization. We exported the acquired images to a PC through a USB port using an external video-capture device (model NPG USB RealStudio II), which copied static images and video data onto the connected computer. To evaluate the lines distortion and vignetting of the intensifier, we used a phantom consisting of an old electronic board with radio-opaque cupper straight lines at right angles (Fig. 6.2, left) attached to the intensifier outer casing. Profiles taken along the line patterns on the projection images showed a straight pattern indicating no significant line distortion or vignetting in the image intensifier. Nevertheless, the projection showed a slightly oval shape (yellow lines in Fig. 6.2, right) that does not match the circular shape of the image intensifier case.

A difference of 8% found between small and large diameter was corrected by the

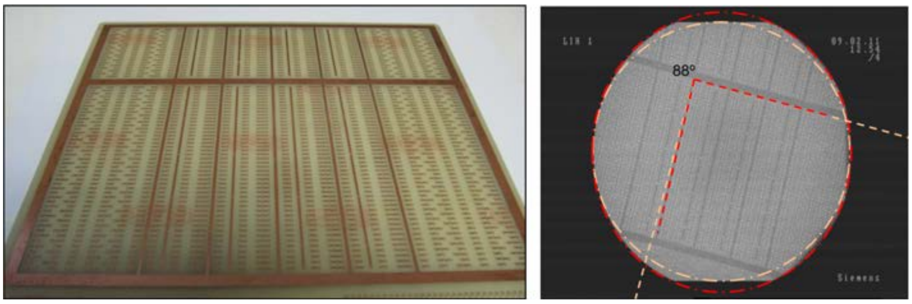

Figure 6.2: *Left: Electronic board consisting of a cupper layer on a plastic plate used to evaluate distortions in the image intensifier. Right: Phantom projection acquired with the C-arm; red lines follow the obtained pattern and yellow lines show the ideal directions and shapes of the phantom.*

geometrical transformation:

$$\begin{pmatrix} x' \\ y' \\ 1 \end{pmatrix} \begin{pmatrix} 1 & 0 & 0 \\ 0 & 1.08 & 0 \\ 0 & 0 & 1 \end{pmatrix} = \begin{pmatrix} x \\ y \\ 1 \end{pmatrix} \tag{6.1}$$

The rotation around y-axis (vertical rotation in Fig.6.3) is severely non-isocentric due to the slipping of the arm over the base. To maintain a reasonable FOV size seen from all projection angles, we acquired 60 projections rotating around the horizontal supporting arm (horizontal rotation in Fig. 6.3, following an orbit close to be isocentric.

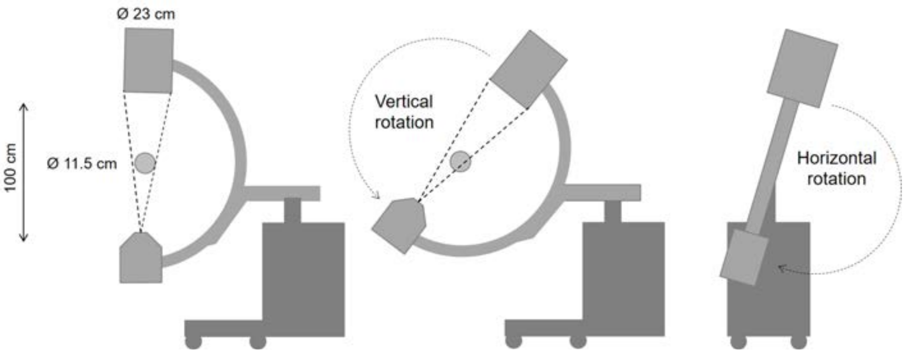

Figure 6.3: *SIREMOBIL geometry (left), non-isocentric vertical rotation movement showing the dimensions of detector and FOV (center), and horizontal rotation movement (right).*

As with other conventional C-arms, not designed for tomography, the movement of our device is manual and the only angular positioning information provided is a rudimentary scale drawn on the arm (Fig. 6.4, left). To increase the accuracy of angular positioning, we implemented a position recording device based on an ADIS16209 digital inclinometer, with an accuracy of 0.1 degrees (Fig. 6.4, left). This system was connected to the computer by a single-board microcontroller, the model TM4C123G of LaunchPad board (Texas Instruments). To avoid inaccuracies due to possible vibration of the C-arm, we averaged ten consecutive readings from the inclinometer. Position values, measured as relative increments in the range of ±90 degrees, were transformed into absolute values ranging from 0 to 360 degrees to be used in the reconstruction. The direction of rotation was estimated from previous recorded positions.

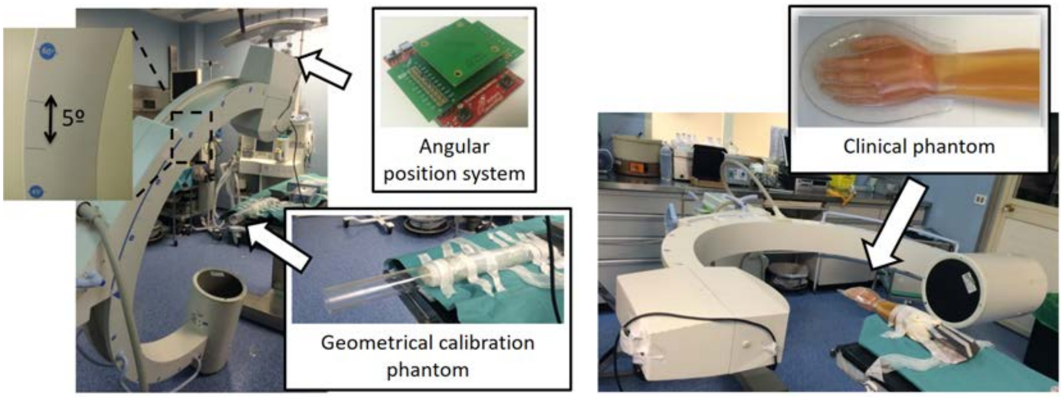

Figure 6.4: *Setting for calibration phantom (left) and clinical phantom (right) acquisitions, showing the angular position recording system.*

An ideal surface support, needed for the SCoLD reconstruction, was extracted from the reference image through thresholding and morphological operations.

Fig. 6.5 shows axial, sagittal views of the image reconstructed with FDK (before and after the refinement of the geometrical calibration) and reconstructed with SCoLD.

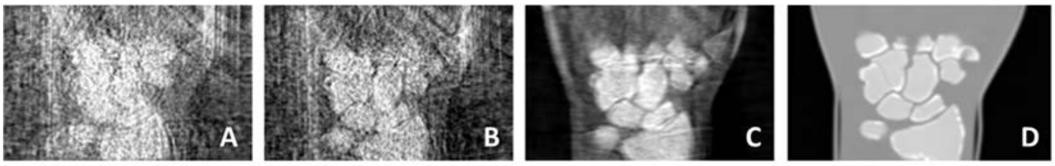

Figure 6.5: *Coronal views of the reconstruction of the PBU-60 phantom. A and B correspond to FDK before and after the refinement of the calibration respectively. C is the reconstruction with SCoLD and D is the CT volume acquired on the helical scanner.*

6.2 Evaluation with in-house built C-arm prototype

The in-house built C-arm prototype is based on a wireless, flat panel detector, the XRpad 4336 (PerkinElmer Inc., US), with an imaging area of 35 cm x 43 cm and a pixel size of 0.1 mm. The X-ray generator is a light weight integrated system Transportix (Radiologia, Algete, Spain) with 4 KW, 125 kVp, 100 mA, 1 ms-10 s, 0,1-250 mAs, and dual focal spot 0,6-1,5 mm. The distance from source to detector is 125 cm, with a useful FOV for reconstruction of 17 cm.

We obtained 49 projections within an angular span of 120 degrees using the rotation along C-arm plane of both hand and foot, as shown in Fig. 6.6.

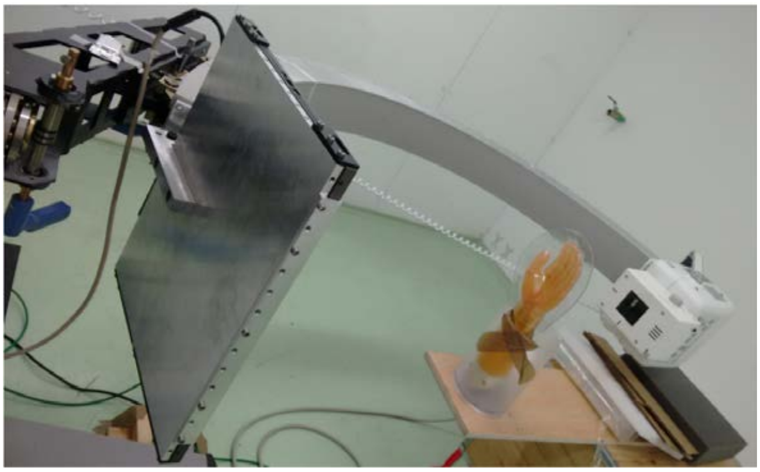

Figure 6.6: *Setting with the in-house C-arm for the clinical phantom acquisition.*

We evaluated a possible implementation of the surface extraction using a 3D Artec Eva scanner (Artec3D, Luxembourg) to scan the surface of the foot, and the software Artec Studio to create a polygonal mesh from which a 3D binary support of the surface was obtained (Fig. 6.7). We could not replicate this experiment with the hand phantom since it is wrapped in a plastic cover that prevents the acquisition of its real surface with a surface scanner, as it can be seen in Fig. 6.6 (top-right).

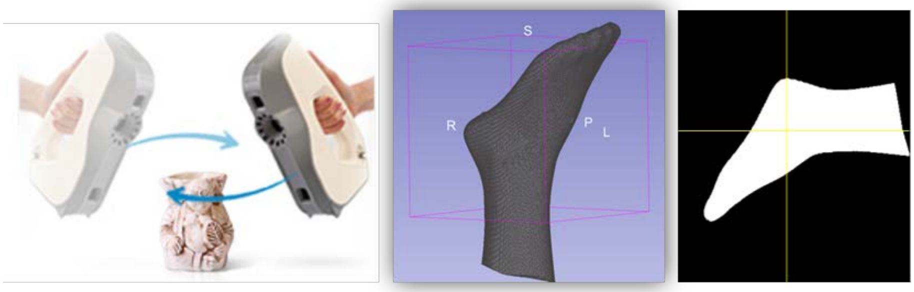

Figure 6.7: *3D light scanner. Source: www.artec3d.com (left), foot surface obtained with the 3D light scanner (center), sagittal view of the support obtained (right).*

Fig. 6.8 and Fig. 6.9 show the reconstructed image using the geometrical calibration with FDK and SCoLD with the ideal support, for limited data with different number of projections.

Fig. 6.10 shows the result of the reconstructed image using the refined geometrical calibration with FDK and SCoLD using the real support obtained with the surface scanner. The horizontal patterns visible in the coronal views are due to the current implementation of the surface-constrained reconstruction method (SCoLD)

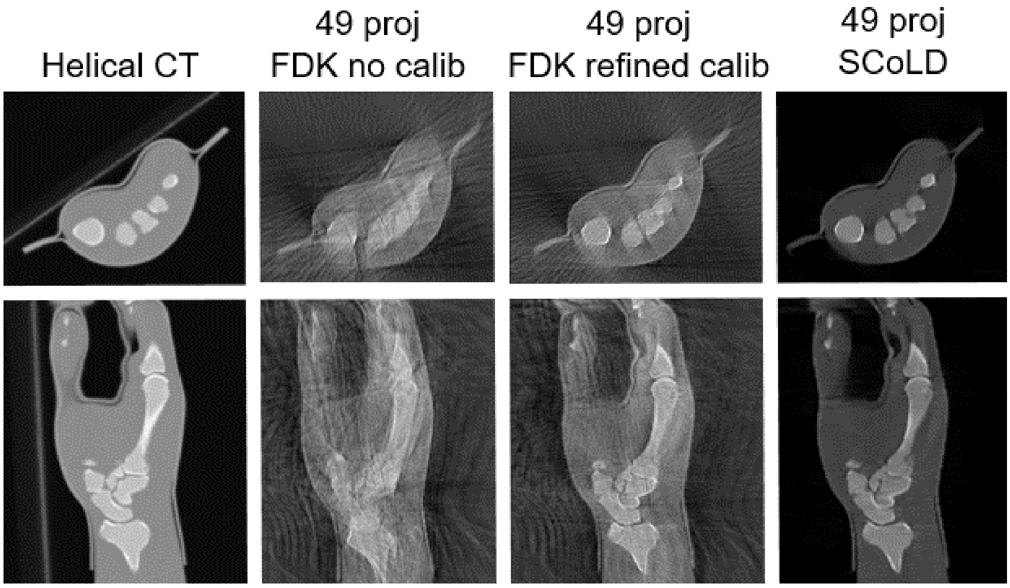

Figure 6.8: *Axial and coronal views of the CT volume acquired on the helical scanner and of the reconstruction of the limited data with an angular span of 120 degrees and 49 projections.*

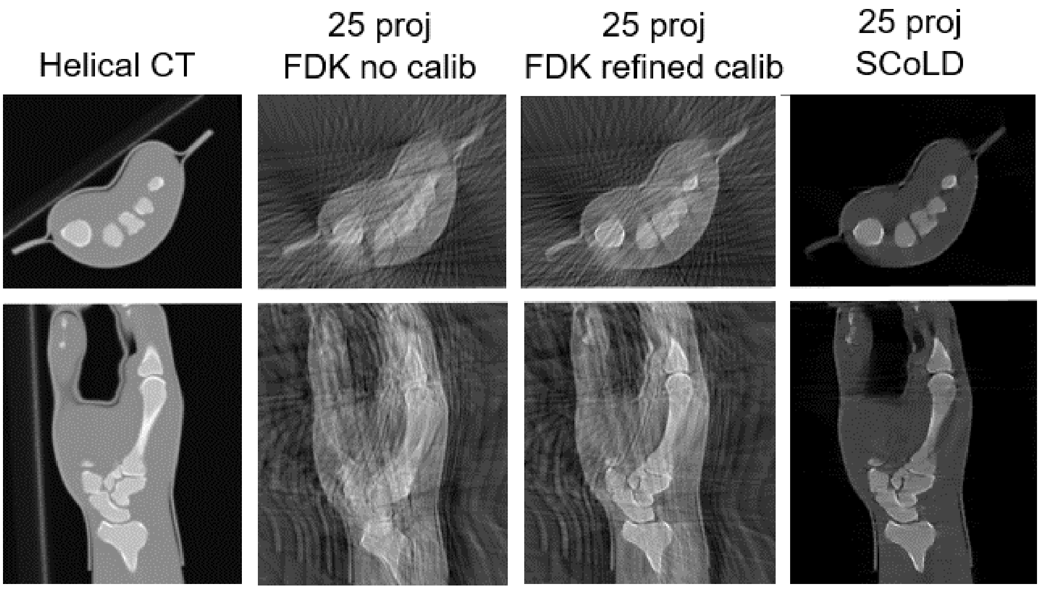

Figure 6.9: *Axial and coronal views of the CT volume acquired on the helical scanner and of the reconstruction of the limited data with an angular span of 120 degrees and 25 projections.*

that calculates only the derivatives along x and y directions. The 3D implementation which would avoid those patterns.

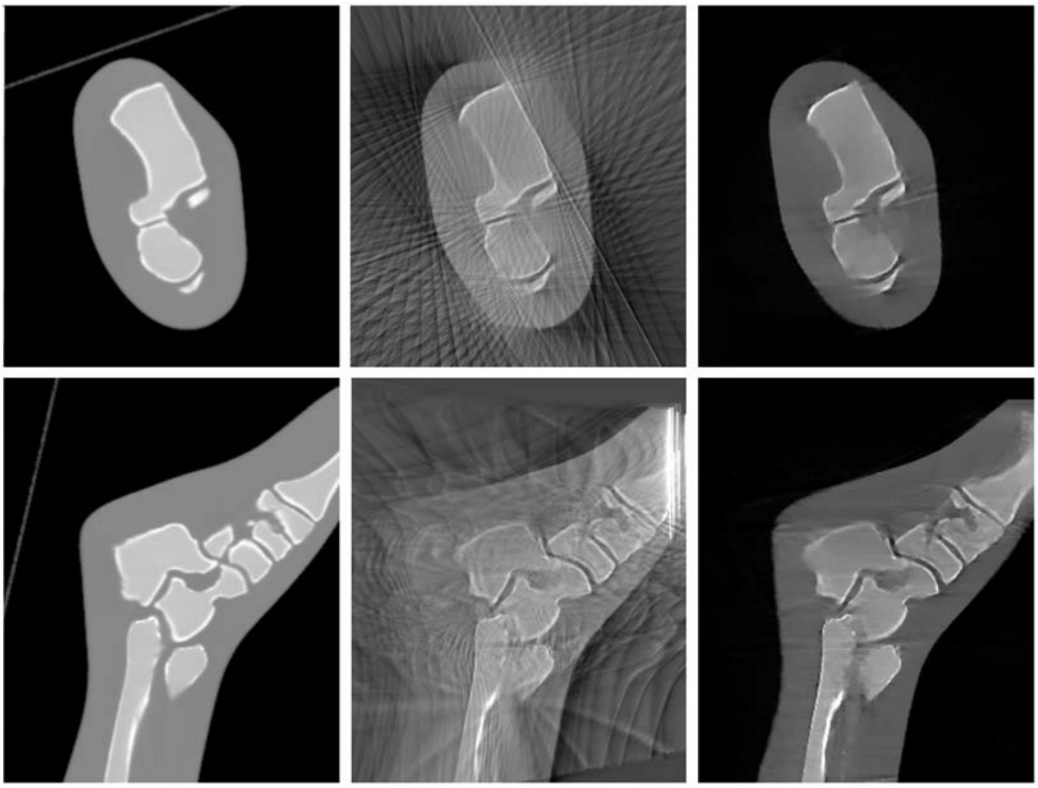

Figure 6.10: *Axial and coronal views of the CT volume acquired on the helical scanner (left) and of the reconstruction of the limited data with 25 projections obtained on the C-arm with FDK (center), and with SCoLD using the real support (right).*

Chapter 7

General discussion, conclusions and future lines

7.1 General discussion

The advances of current planar X-ray systems, such as the use of digital detectors and flexible robotized movements of the source and the detector, foster the incorporation of advanced capabilities into these systems. In this line, this thesis presents original contributions in two directions: dual energy radiography and 3D imaging with X-ray sytems designed for planar systems.

Dual-energy radiography studies are currently based on the weighted subtraction method that results in tissue maps valid for visualization but not for quantitative evaluation. Those maps have to be tuned manually by a radiologic technician with high expertise in the protocol. Furthermore, in densitometry exams, the bone mineral content and density are estimated from these non-quantitative studies and compared through a statistical test with tabulated measurements of a representative population sample differentiated by age and gender.

The first contribution of this thesis is a complete protocol to incorporate dual energy capabilities that enable quantitative planar studies. The proposal is based on the use of a preliminary calibration with a very simple and low-cost phantom formed by two parts corresponding to soft tissue and bone equivalent materials. This calibration is performed automatically with no strict placement requirements, thus avoiding the need of the interaction of an experienced technician.

Among the properties studied for the selection of the equivalent materials, such as physical density or mean ratio of atomic number-to-mass (Z/A), energy dependency resulted the most relevant. Simulation studies showed water to be the optimum soft tissue substitute due to its very similar energy dependency leading to the best tissue maps compared with other candidate materials proposed in the literature. Following this result, we propose the use of a hollow prism of PMMA with a wall thickness of 5.6 mm filled with water. An alternative to avoid possible water leaking and bubbles formation, could be a solid PMMA prism. However, it allows visual inspection of lesions but not quantitative studies, due to its large difference in energy dependency with respect to soft tissue. As an optimum substitute for bone, aluminum is desirable compared with other widely used materials such as Teflon. We propose a prism made of the aluminum alloy AL6082, with an energy response very similar to that of bone, leading to excellent quantitative results as well as good machinability, availability and cost (around 2 €/Kg).

The protocol provides real mass-thickness values directly enabling real quantitative studies and not only relative comparisons, as in densitometry exams. It allows identifying small calcifications or nodules down to 6 mm, reported to show a low rate of detection in chest imaging. The comprehensive evaluation shown in this thesis reported the feasibility of the proposal.

The second contribution is a complete protocol for the incorporation of tomographic capabilities into X-ray systems originally intended for planar imaging. For this purpose, we have to face three main challenges: 1) the geometrical calibration of equipment that follows non-standard circular trajectories posing more difficulties, 2) the reconstruction of a limited number of projections from a reduced angular span, which leads to severe artifacts when using conventional reconstruction methods, and 3) the optimization of the acquisition protocols, not yet explored with those systems.

In most planar systems, the relative position of the source-detector pair varies considerably during acquisition making it necessary a complete geometrical characterization. To handle this first challenge, we propose a new geometrical calibration method, based on the work of Cho et al. [Cho et al., 2005], that estimates all the parameters per-projection including the two inclination angles of the detector with respect to the horizontal and vertical directions independently. The evaluation of this method was complemented with a study of the geometrical tolerances based on the effect of the different misalignments on the reconstructed images. Errors in the estimation of the calibration parameters resulted much lower than the tolerances needed for a correct reconstruction.

To handle the second challenge, we propose a novel iterative Surface-Constrained reconstruction method for Limited-Data tomography (SCoLD), which makes use of the surface information of the patient to compensate the lack of data in limited-view scenarios using planar systems. SCoLD incorporates the surface-based support as an imposed constraint, following the Split Bregman formulation. Evaluation of the proposed method showed fast convergence and robustness to variations of the parameters, independently of the angular span or the number of projections. Evaluation showed a good recovery of the uniformity and the density values, independently of the sample, thus allowing quantitative studies.

SCoLD reduces significantly the streak artifacts produced in all limited-data configurations similarly to previous proposals in the literature. However, its main advantage over previous works is that the restriction on the search space by exploiting the surface-based support in SCoLD, results in a complete recovery of the external contour of the sample and surroundings even for extremely reduced angular spans.

The proposed implementation of SCoLD enables the use of flexible geometries incorporating the variations of all the geometrical parameters. Its modular design allows to create new reconstruction approaches easily adding more constraints formulated as Bregman iterations and exploiting other transformed domains such as wavelet or curvelet space. Its efficient implementation through GPU-accelerated kernels and partitioning strategies enables the reconstruction of large volumes ($>1024^3$ pixels) in a few minutes (with a reduction up to 48 $\times$ compared to a CPU-only version).

The study of the optimum acquisition protocols for limited-data scenarios using SCoLD, allowed us to identify some recommendations. Reducing angular span affects much more than the number of projections. SCoLD allows to reduce the angular span down to 60 degrees thanks to the surface-based constraint. Results showed that it is possible to reduce the number of projections until 33% within any angular span. In scenarios where movement limitations are more strict, such as operating rooms where monitoring equipment may block the system rotation, SCoLD can maintain the image quality when acquiring non-consecutive projections, even separated 90 degrees. In general, it is desirable to acquire projections with rays tangent to most edges.

Within a collaboration framework with the clinics through University Hospital Gregorio Marañón and the industry through the company SEDECAL S.A. (Madrid, Spain), the feasibility of the whole protocol has been proved using two C-arm systems, based respectively on an image intensifier and on a flat panel detector. We proved that a real surface support for SCoLD reconstruction can be obtained from a structured light 3D scanner. This surface information was also used to refine the geometrical calibration parameters compensating the low repeatibility of the source and detector positions. However, the light structure scanner presented two limitations: 1) its elevated cost, 2) possible errors due to the body hair or to the use of no tight clothes that can provide a wrong surface of the patient. The first one can be solved using less expensive systems, such as the Kinect camera system, and the second problem using infrared cameras.

7.2 General conclusions

1.- A complete protocol to incorporate dual energy capabilities in planar systems have been proposed. Compared to current DXA systems, 1) it provides real mass-thickness values directly, allowing quantitative planar studies instead of relative comparisons and 2) it is based on an automatic preliminary calibration without the need of interaction of an experienced technician.

2.- Energy dependency of the equivalent material of the calibration is key to obtain quantitative studies in addition to correct separation of soft tissue and bone structures. The proposed calibration phantom is formed by a prism of PMMA filled with water and a prism made of the aluminum alloy AL6082.

3.- A complete protocol for the incorporation of tomographic capabilities into X-ray systems originally intended for planar imaging have been proposed including a new geometrical procedure and an advance reconstruction method able to deal with limited-view data acquired in non-standard geometries.

4.- The proposed reconstruction method incorporates the surface information, which can be extracted with a 3D light surface scanner, as an imposed constraint. The restriction of the search space by exploiting the surface-based support becomes crucial for a complete recovery of the external contour of the sample and surroundings when the angular span is extremely reduced. The modular, efficient and flexible design followed for its implementation allows for the reconstruction of limited-view data with non-standard trajectories in real time.

5.- Regarding the acquisition protocol with these systems, it is desirable to acquire projections with rays tangent to most edges. Using the surface-constrained method, it is possible to reduce the total number of projections until 33% and the angular span down to 60 degrees. In scenarios where movement limitations of the source-detector pair are more strict, non-consecutive projections can be acquired even separated 90 degrees.

The contributions of this thesis open the way to providing depth and quantitative information very valuable for the improvement of radiological diagnosis. This could impact considerably the clinical practice, as conventional radiology is still the imaging modality most used in Medicine, accounting for 80-90% of the total medical imaging exams. These advances open the possibility of new clinical applications in scenarios where 1) the reduction of the radiation dose is key, such as lung screening or Pediatrics, according to the ALARA criteria (As Low As Reasonably Achievable), 2) a CT system is not available due to movement limitations, such as during surgery or in an ICU and 3) where costs issues complicate the availability of CT systems, such as rural areas or underdeveloped countries.

Finally, the work of this thesis has a clear application in the industry, since it is part of a proof of concept of the new generation of planar X-ray systems which will be commercialized worldwide by the company SEDECAL (Madrid, Spain), among the leaders worldwide in radiology systems. Currently, two software developments derived from this thesis have been licensed to SEDECAL (16/2017/710, 16/2017/7104).

7.3 Future lines

The proposed protocol for incorporating dual energy capabilities into planar X-ray systems has been tested only on a thorax anthropomorphic phantom. The next step could be to compare our results with those obtained using a current DEXA system with the same thorax phantom, and on different anatomical parts such as abdomen or limbs. This evaluation will be performed within the current collaboration with the Radiology Department of University Hospital Gregorio Marañón.

The current implementation of the surface-constrained reconstruction method (SCoLD) calculates only the derivatives along x and y directions, which results in some horizontal patterns visible in the coronal views of the reconstructed limited data. We are already developing its extension to 3D, which would avoid those patterns.

The use of the Total Variation minimization in SCoLD for the assumption of homogeneous areas in the attenuation maps, may result in patchy images in some cases. Our group proved that the use of the wavelet domain enhances the texture quality of the final reconstruction. Another option could be to include texture information from patches of a standard CT as an imposed constraint.

The feasibility of the proposal for incorporating 3D capabilities into C-arm systems that follow non-standard circular trajectories was proved. We are currently testing it in geometries even less similar to a CT, such as linear tomosynthesis with a radiology room, thanks to the geometrical flexibility of the SCoLD implementation. In this case, the geometrical calibration and the acquisition protocol will be adapted and optimized. An extra challenge posed by these systems is the effect of the anti-scatter grids due to the different relative position between the source and the detector, which could be solved avoiding the use of those grids and compensating the scatter effect by software.

Regarding the acquisition protocols, the scan views can be designed and optimized for each type of study. Even more, we could design an intelligent X-ray system that updates the scan views and the number of projections based on real-time intermediate reconstructions.

Finally, the two main contributions of this thesis, dual energy and 3D capabilities, can be exploited simultaneously by acquiring different groups of projections at different voltages. These studies could provide more quantitative information while still reducing the dose compared with a conventional CT study. In this line, the acquisition protocol should be also optimized taking into account the geometry limitations and the source capabilities for fast kilovoltage switching.

Chapter 8

Scientific contributions derived from this thesis

8.1 Journal papers

Published in International Journals

- de Molina, C., Serrano E., García-Blas, J., Carretero, J., Desco, M., and Abella, M. *GPU-accelerated iterative reconstruction for limited-data tomography in CBCT systems.* BMC Bioinformatics, 2018. Impact Factor: 2.448 (Q1).
- Abella, M., Serrano, E., García-Blas J., García, I., de Molina, C., Carretero, J., and Desco, M. *Fux-sim: Implementation of a fast universal simulation/reconstruction framework for X-ray systems.* PloS one, 12(7):e0180363, 2017. Impact Factor: 2.086 (Q1).

Submitted in International Journals

- Abella, M., de Molina, C., Ballesteros, N., García-Santos, A., Martínez, A., García-Barquero, I., and Desco, M. *Enabling tomography with low-cost C-arm systems.* PloS one, 2018. Impact Factor: 2.086 (Q1). Preliminary accepted.
- Abella, M., García-Barquero, I. de Molina, C. and Desco, M. *Tolerance to geometrical inaccuracies in CBCT systems: A comprehensive Study.* PloS one, 2018. Impact Factor: 2.086 (Q1).
- de Molina, C., Martínez, C., Desco, M., and Abella, M. *Optimization design of a calibration for quantitative radiography.* Scientific Reports, 2018. Impact Factor: 4.259 (Q1).

Under Preparation

- de Molina, C., Abascal, J.F.P.J., Desco, M. and Abella, M. *Surface-Constrained Method for Limited-Data Tomography in CBCT Systems (SCoLD).* To be submitted to: IEEE Trans. Med. Imaging. Impact Factor: 3.942 (Q1).

- de Molina, C., Abascal, J.F.P.J., Desco, M. and Abella, M. *Exploration and evaluation of span, limited view limited angle geometries for different clinical applications with planar X-ray systems.* To be submitted to: Physics on Medicine and Biology. Impact Factor: 2.742 (Q2).

8.2 Contributions to conferences

Proceedings

- Abella, M., de Molina, C., Ballesteros, N., García-Santos, A., García-Barquero, I., Martínez, A., Desco, M. *Setting up a low-cost C-arm for its use as a tomograph: preliminary results.* CT-Meeting 2018: The 5th International Conference on Image Formation in X-Ray Computed Tomography. 143-146. Poster.

- Abascal, J.F.P.J., Abella, M., Mory, C., Ducros, N. de Molina, C., Marinetto, E., Peyrin, F., Desco, M. *Sparse reconstruction methods in x-ray CT.* Proc in SPIE Optical Engineering + Applications - Developments in X-Ray Tomography XI (2017), San Diego, US. http://dx.doi.org/10.1117/12.2272711. Oral presentation.

- Martínez, C., de Molina, C., Desco, M., Abella, M. *Calibration free method for beam hardening compensation: preliminary results.* 2017 IEEE Nuclear Science Symposium and Medical Imaging Conference. Poster.

- Serrano, E., García -Blas, J., García, I., de Molina, C., Carretero, J., Desco, M., Abella, M. *Design and Evaluation of a Parallel and Multi-Platform Cone-Beam X-Ray Simulation Framework.* CT-Meeting 2016: The 4th International Conference on Image Formation in X-Ray Computed Tomography. 423-426. Poster.

- de Molina, C., Abascal, J.F.P.J., Desco, M., Abella, M. *Study of the possibilities of Surface-Constrained Compressed Sensing (SCCS) Method for Limited-View Tomography in CBCT systems.* CT-Meeting 2016: The 4th International Conference on Image Formation in X-Ray Computed Tomography. Poster.

- Martínez, C., de Molina, C., Desco, M., Abella, M. *Simple method for beam-hardening correction based on a 2D linearization function.* CT-Meeting 2016: The 4th International Conference on Image Formation in X-Ray Computed Tomography. 475-478. Poster.

- Martínez, A., Polo, R., de Molina, C., Martínez, C., García -Blas, J., Desco, M., Abella, M. *X-Ray Scatter Correction Method for Planar Radiography Based on a Beam Stopper: a Simulation Study.* 2016 IEEE Nuclear Science Symposium and Medical Imaging Conference. Poster.

- Martínez, A., García-Santos, A., Serrano, E., García -Blas, J.,de Molina, C., Polo, R., Desco, M., Abella, M. *A software tool for the design and simulation of X-ray acquisition protocols.* CT meeting 2016: In Proceedings of the 4th International Meeting on Image Formation in X-Ray CT. 323-326. Poster.

- de Molina, C., Abascal, J. F. P. J., Pascau, J., Desco, M., Abella, M. (2014, November). *Evaluation of the possibilities of limited angle reconstruction for the use of digital Radiography system as a tomograph.* In Nuclear Science Symposium and Medical Imaging Conference (NSS/MIC), 2014 IEEE (pp. 1-4). IEEE. Poster.

- García-Blas, J. and Abella, M. and de Molina, C. and Liria, E. and Isaila, F., Carretero, J. and Desco, M. *Parallel Implementation of a X-Ray Tomography Reconstruction Algorithm for High-Resolution Studies.* XIII Mediterranean Conference on Medical and Biological Engineering and Computing 2013. Poster.

- de Molina, C. and Pascau, J. and Desco, M. and Abella, M. *Calibration of a C-arm X-ray System for Its Use in Tomography.* XIII Mediterranean Conference on Medical and Biological Engineering and Computing, 2013. Oral presentation.

- Liria, E., Higuero, D., Abella, M. and de Molina, C. and Desco, M. *Exploiting parallelism in a X-ray tomography reconstruction algorithm on hybrid multi-GPU and multi-core platforms.* 2012 IEEE 10th International Symposium on Parallel and Distributed Processing with Applications (ISPA). 867-868. Poster.

- de Molina, C., Sisniega, A., Vaquero, J.J., Desco, M and Abella, M. *Complete scheme for beam hardening correction in small animal computed tomography.* 2012 IEEE 2012 Nuclear Science Symposium and Medical Imaging Conference (NSS/MIC). 3835-3838. Poster.

- Ye, X., de Molina, C., Ballesteros, N., Martínez, A., Desco, M. Abella, M. *Extracción de superficie con escáner de luz estructurada para tomografía de ángulo limitado.* XXXV Congreso Anual de la Sociedad Española de Ingeniería Biomédica (CASEIB), 2017. 243-246. Oral presentation.

- Ballesteros, N., de Molina, C., Desco, M., Abella, M.*Corrección de artefacto por movimiento respiratorio para TAC de pequeño animal en estudios con bajas dosis de radiación.* Congreso Anual de la Sociedad Española de Ingeniería Biomédica (CASEIB), 2017. 247-250. Oral presentation.

- Martínez, C. Ballesteros, N. de Molina, C. Desco, M. Abella, M.*Corrección del efecto de endurecimiento basado en una linealización 2D.* XXXV Congreso

Anual de la Sociedad Española de Ingeniería Biomédica (CASEIB), 2017. 529-532. Oral presentation.

- Martínez, C., de Molina, C., Desco, M., Abella, M..*Corrección empírica del artefacto de endurecimiento de haz exento de calibración.* Congreso Anual de la Sociedad Española de Ingeniería Biomédica (CASEIB), 2016. 2-4. Oral presentation.

- García-Santos, A., de Molina, C., García Barquero, I., Pascau González-Garzón, J., Desco Menéndez, M., Abella García, M.*Setting up a C-arm for its use as a tomograph / Puesta a punto de un arco en C para su uso como tomógrafo.* XXXIII Congreso Anual de la Sociedad Española de Ingeniería Biomédica (CASEIB), 2015. 134-137. Oral presentation.

- García-Santos, A., de Molina, C., García, I., Pascau, J., Desco, M., Abella, M.*Evaluation of the effect of angular calibration accuracy in a C-arm for its use in tomography.* XXXII Congreso Anual de la Sociedad Española de Ingeniería Biomédica (CASEIB), 2014. Oral presentation.

- de Molina, C., García -Barquero, I., Desco, M., Abella, M. *Study of the Implementation of Dual Energy Decomposition in a Real Digital Radiography System.* XXXII Congreso Anual de la Sociedad Española de Ingeniería Biomédica (CASEIB), 2014. Oral presentation.

- de Molina, C., Sisniega, A., Vaquero, J.J. and Desco, M. and Abella, M. *Un nuevo algoritmo para la reducción del artefacto de anillo en tomografía computarizada de pequeño animal.* XXX Congreso Anual de la Sociedad Española de Ingeniería Biomédica (CASEIB), 2012. Oral presentation.

- de Molina, C., Abella, M., Sisniega, A., and Vaquero, J.J. and Desco, M. *Corrección empírica de primer y segundo orden del artefacto de endurecimiento de haz en imágenes de micro-TAC.* Congreso Anual de la Sociedad Española de Ingeniería Biomédica (CASEIB), 2011. Oral presentation.

Abstracts

- de Molina, C., Martínez C., Desco, M., Abella, M. *Calibration set-up for Dual Energy capabilities in a Real Advance Digital Radiography System.* 13th European Molecular Imaging Meeting (EMIM), 2018. Poster.

- Martínez C., Ballesteros, N., de Molina, C., Desco, M., Abella, M. *Recovering density values on small animal X-ray imaging through beam hardening compensation: preliminary results.*. 13th European Molecular Imaging Meeting (EMIM), 2018. Poster.

- Ballesteros, N., de Molina, C., Ye, X., Desco, M., Abella, M. *Surface extraction with structured-light scanner for limited angle tomography.* 13th European Molecular Imaging Meeting (EMIM), 2018. Poster.

- Martínez, C., de Molina, C., Ballesteros, N., Desco, M., Abella, M. Calibration free method for beam hardening compensation: preliminary results. 2nd ySMIN Meeting, 2018. Oral presentation.
- Martínez, C., de Molina, C., Desco, M., Abella, M. Free calibration method for beam hardening correction in small animal studies. 1st ySMIN Meeting, 2017. Poster.
- Martínez, A., Polo, R., de Molina, C., Martínez, C., García-Blas, J., Desco, M., Abella, M. X-Ray scatter correction method for planar radiography based on a beam stopper: a simulation study. 1st ySMIN Meeting, 2017. Poster.
- de Molina, C., Martínez, C., Desco, M., Abella, M. Calibration set-up for Dual Energy capabilities in a Real Digital Radiography System. 1st ySMIN Meeting, 2017. Poster

8.3 Intellectual Property

- *Title*: FUX-Sim, Software de simulación de sistemas de radiología
  Inventors: Abella, M., Desco, M., García-Barquero I., de Molina, C., Serrano, E., García-Blas, J., Carretero, J.
  Organization: Universidad Carlos III de Madrid y Fundación para la Investigación Biomédica del Hospital Gregorio Marañón
  Application number: M-3481/2017, de 24/05/2017
  Registration number: 16/2017/710, 24/05/2017
  Licensed to the company "Sociedad Española de Electromedicina y Calidad (SEDECAL)" in April, 2018.
- Title: Rap-ToR, Software de reconstrucción de imagen en tiempo real para TAC *Inventors*: Abella, M., Desco, M., de Molina, C., Serrano, E., García-Blas, J., Carretero, J.
  Organization: Universidad Carlos III de Madrid y Fundación para la Investigación Biomédica del Hospital Gregorio Marañón
  Application number: M-3480/2017, de 24/05/2017
  Registration number: 16/2017/7104
  Licensed to the company ”Sociedad Española de Electromedicina y Calidad (SEDECAL)” in April, 2018.

8.4 Participation in Research Projects

This thesis has been developed as part of several research projects with public funding:

- DPI2016-79075-R. ”Nuevos escenarios de tomografía por rayos X”, IP: Mónica Abella García, Ministerio de Economía y Competitividad, 01/01/2017-31/12/2019, 147.620 €.

- ”Nuevos escenarios de tomografía por rayos X (NEXT) DPI2016-79075-R. Ministerio de Economía”, Industria y Competitividad. (Universidad Carlos III de Madrid). 30/12/2016-29/12/2019. 147.620 €.

- 2018/00169/001. ”Obtención de imagen 3D con sistemas de tomografía de rayos X y sistemas de arco en C”. Financiado por la Fundación para la Investigación Biomédica del Hospital Gregorio Marañón. 34.000 €. 07/03/2018 - 31/12/2019. IP: Mónica Abella García.

- DTS17/00122, ”Nuevo sistema de tomografía por rayos X portátil”, IP: Manuel Desco Menéndez, 01/01/2018-31/12/2019, Instituto de Salud Carlos III, 84.920 €.

- 2017/00550/001. ”Evaluación de protocolos de adquisición para un nuevo sistema de rayos X multipropósito”, financiado por la entidad SOCIEDAD ESPAÑOLA DE ELECTROMEDICINA CALIDAD S. A. IP: Mónica Abella García y Francisco Javier García Blas. 14.900 €. 01/10/2017-31/03/2018.

- Collaboration with the professor Adam Alessio at the Imaging Research Laboratory (IRL) of the University of Washington (Seattle, USA). 4 months. 12/11/2015-11/03/2016.

- FP7-IMI-2012 (GA-115337), ”PreDict-TB: Model-based preclinical development of anti-tuberculosis drug combinations”. FP7-IMI - Seventh Framework Programme (EC-EFPIA). Unión Europea. (Universidad Carlos III de Madrid). 01/05/2012-31/10/2017.

- TEC2013-47270-R, ”Avances en Imagen Radiológica (AIR)”, Ministerio de Economía y Competitividad”, 01/01/2014-31/12/2016. IP: Mónica Abella Garcia and Manuel Desco Menéndez. 160.204 €

- 120028/14, ”Nuevo sistema integral de radiografía”, IP: Manuel Desco Menéndez, Fundación para la Innovación y Prospectiva de la Salud en EspaÃśa (FIPSE), 15/02/2015-14/02/2016. 25.000,00 €

- RTC-2014-3028-1, ”Nuevos Escenarios Clínicos con Radiología Avanzada (NECRA)”, Ministerio de Economía y Competitividad, 01/06/2014-31/12/2016 IP: Mónica Abella García. 2014-2016. 219.458,96 €

- IDI-20130301, ”Nuevo sistema integral de radiografía (INNPROVE: INNovative image PROcessing in medicine and VEterinary)”, IP: Mónica Abella García and Manuel Desco Menéndez. Ministerio de Economía y Competitividad. Subcontratación CDTI, 14/01/2013-31/03/2015. Total: 1.860.629€ (UC3M: 325.000€). (Art. 83)

- IPT-2012-0401-300000 INNPACTO 2012 , ”Tecnologías para Procedimientos Intraoperatorios Seguros y Precisos. XIORT. MINECO. (Universidad Carlos III de Madrid). 01/01/2013-31/12/2015.

Also, the PhD candidate was working at the prestigious medical imaging center, the Imaging Research Laboratory (IRL) of the University of Washington, led by the professor Paul Kinahan, with a large experience dedicated to advanced tomographic imaging. Her work was supervised by the doctor in Bioengineering and member of the American Board of Science in Nuclear Medicine, Adam Alessio, and was focused on tomosynthesis reconstruction, as part of a research project whose main goal is to discriminate ground glass opacity in chest tomosynthesis images giving a score of the level and avoiding the need of a CT, which implies higher cost and dose. This internship also helped to the establishment of a more formal and stable collaboration on the research line on limited-data tomography.

8.5 Bachelor Thesis

During the development of this thesis, the doctoral candidate has collaborated in the direction of several bachelor thesis on X-ray imaging:

- Ye, X., *Advanced image reconstruction for limited-view Cone-Beam CT*. 2018. Bachelor thesis (biomedical engineering), 11/07/2018.
- García-Santos, A., *Setting up a C-arm for its use as a tomographâĂİ. Bachelor thesis*, (biomedical engineering) with grade: 10, 09/07/2015.
- Viña, C., *Implementation of a Complete Scheme of Beam Hardening Correction in a Small Animal CT Scanner*. Bachelor thesis (telecommunications engineering) with grade: 10 Cum Laude, 13/07/2015.
- Pedrero, A., *Truncation artifact compensation for small-animal X-Ray tomography*. Bachelor thesis (biomedical engineering) with grade: 10 Cum Laude, 09/07/2014.
- Paraíso, M., *Calibration of a C-arm X-ray system for its use in tomography*. Bachelor thesis (industrial engineering) with grade: 10 Cum Laude, 27/02/2013.

Bibliography

[Abascal et al., 2016] Abascal, J. F., Abella, M., Marinetto, E., Pascau, J., and Desco, M. (2016). A novel prior-and motion-based compressed sensing method for small-animal respiratory gated ct. *PloS one*, 11(3):e0149841.

[Abascal et al., 2008] Abascal, J.-F. P., Arridge, S. R., Bayford, R. H., and Holder, D. S. (2008). Comparison of methods for optimal choice of the regularization parameter for linear electrical impedance tomography of brain function. *Physiological measurement*, 29(11):1319.

[Abascal et al., 2011] Abascal, J.-J., Chamorro-Servent, J., Aguirre, J., Arridge, S., Correia, T., Ripoll, J., Vaquero, J. J., and Desco, M. (2011). Fluorescence diffuse optical tomography using the split bregman method. *Medical physics*, 38(11):6275–6284.

[Abella, 2010] Abella, M. (2010). *Contributions to image reconstruction in high-resolution multimodality systems for preclinical applications*. PhD thesis, Universidad Politecnica de Madrid.

[Abella et al., 2018] Abella, M., García, I., De Molina, C., and Desco, M. (2018). Tolerance to geometrical inaccuracies in cbct systems: A comprehensive study. *submitted to PloS one (under review)*.

[Abella et al., 2017] Abella, M., Serrano, E., Garcia-Blas, J., García, I., De Molina, C., Carretero, J., and Desco, M. (2017). Fux-sim: Implementation of a fast universal simulation/reconstruction framework for x-ray systems. *PloS one*, 12(7):e0180363.

[Abella et al., 2012] Abella, M., Vaquero, J. J., Sisniega, A., Pascau, J., Udías, A., García, V., Vidal, I., and Desco, M. (2012). Software architecture for multi-bed fdk-based reconstruction in x-ray ct scanners. *Computer methods and programs in biomedicine*, 107(2):218–232.

[Adams, 2013] Adams, J. E. (2013). Dual-energy x-ray absorptiometry. In *Osteoporosis and Bone Densitometry Measurements*, pages 101–122. Springer.

[Agulleiro and Fernandez, 2010] Agulleiro, J. and Fernandez, J.-J. (2010). Fast tomographic reconstruction on multicore computers. *Bioinformatics*, 27(4):582–583.

[Alvarez and Macovski, 1976] Alvarez, R. E. and Macovski, A. (1976). Energy-selective reconstructions in x-ray computerised tomography. *Physics in Medicine & Biology*, 21(5):733.

[Ballesteros et al., 2018] Ballesteros, N., De Molina, C., Ye, X., Desco, M., and Mónica, A. (2018). Surface extraction with structured-light scanner for limited angle tomography. *13th European Molecular Imaging Meeting (EMIM).*

[Bazzocchi et al., 2016] Bazzocchi, A., Ponti, F., Albisinni, U., Battista, G., and Guglielmi, G. (2016). Dxa: Technical aspects and application. *European journal of radiology*, 85(8):1481–1492.

[Bellers et al., 2004] Bellers, E. B., de Bruijn, F. J., Mistretta, C. A., and Wang, Y. (2004). An automatic calibration method for dual energy material decomposition. *Journal of X-ray Science and Technology*, 12(1):19–25.

[Boone et al., 2001] Boone, J. M., Nelson, T. R., Lindfors, K. K., and Seibert, J. A. (2001). Dedicated breast ct: radiation dose and image quality evaluation. *Radiology*, 221(3):657–667.

[Braby et al., 1995] Braby, L., Johnson, G., and Barthe, J. (1995). Practical considerations in the design and construction of tissue-equivalent proportional counters. *Radiation protection dosimetry*, 61(4):351–379.

[Bregman, 1967] Bregman, L. M. (1967). The relaxation method of finding the common point of convex sets and its application to the solution of problems in convex programming. *USSR computational mathematics and mathematical physics*, 7(3):200–217.

[Brody et al., 1981] Brody, W. R., Butt, G., Hall, A., and Macovski, A. (1981). A method for selective tissue and bone visualization using dual energy scanned projection radiography. *Medical physics*, 8(3):353–357.

[Burger, 2016] Burger, M. (2016). Bregman distances in inverse problems and partial differential equations. In *Advances in Mathematical Modeling, Optimization and Optimal Control*, pages 3–33. Springer.

[Bushberg, 2002] Bushberg, J. T. (2002). *The essential physics of medical imaging.* Lippincott Williams & Wilkins.

[Candes and Romberg, 2007] Candes, E. and Romberg, J. (2007). Sparsity and incoherence in compressive sampling. *Inverse problems*, 23(3):969.

[Cardinal and Fenster, 1990] Cardinal, H. N. and Fenster, A. (1990). An accurate method for direct dual-energy calibration and decomposition. *Medical physics*, 17(3):327–341.

[Chang et al., 2013] Chang, M., Li, L., Chen, Z., Xiao, Y., Zhang, L., and Wang, G. (2013). A few-view reweighted sparsity hunting (fresh) method for ct image reconstruction. *Journal of X-ray Science and Technology*, 21(2):161–176.

[Chen et al., 2016] Chen, Z., Qi, H., Wu, S., Xu, Y., and Zhou, L. (2016). Few-view ct reconstruction via a novel non-local means algorithm. *Physica Medica: European Journal of Medical Physics*, 32(10):1276–1283.

[Cho et al., 2005] Cho, Y., Moseley, D. J., Siewerdsen, J. H., and Jaffray, D. A. (2005). Accurate technique for complete geometric calibration of cone-beam computed tomography systems. *Medical physics*, 32(4):968–983.

[Chuang and Huang, 1988] Chuang, K.-S. and Huang, H. (1988). Comparison of four dual energy image decomposition methods. *Physics in Medicine & Biology*, 33(4):455.

[Collums, 2012] Collums, T. L. (2012). *Comparison of plastics used in tissue equivalent proportional counters (TEPC) and development of a balloon borne TEPC*. Oklahoma State University.

[Conant et al., 2016] Conant, E. F., Beaber, E. F., Sprague, B. L., Herschorn, S. D., Weaver, D. L., Onega, T., Tosteson, A. N., McCarthy, A. M., Poplack, S. P., Haas, J. S., et al. (2016). Breast cancer screening using tomosynthesis in combination with digital mammography compared to digital mammography alone: a cohort study within the prospr consortium. *Breast cancer research and treatment*, 156(1):109–116.

[Correia et al., 2011] Correia, T., Aguirre, J., Sisniega, A., Chamorro-Servent, J., Abascal, J., Vaquero, J. J., Desco, M., Kolehmainen, V., and Arridge, S. (2011). Split operator method for fluorescence diffuse optical tomography using anisotropic diffusion regularisation with prior anatomical information. *Biomedical optics express*, 2(9):2632–2648.

[Crabtree et al., 2007] Crabtree, N. J., Leonard, M. B., and Zemel, B. S. (2007). Dual-energy x-ray absorptiometry. In *Bone Densitometry in Growing Patients*, pages 41–57. Springer.

[Dai et al., 2016] Dai, X., Shi, D., and Deng, H. (2016). Limited-view ct reconstruction based on discrete krawtchouk moments. In *Information Science and Control Engineering (ICISCE), 2016 3rd International Conference on*, pages 439–443. IEEE.

[Daly et al., 2008] Daly, M., Siewerdsen, J., Cho, Y., Jaffray, D., and Irish, J. (2008). Geometric calibration of a mobile c-arm for intraoperative cone-beam ct. *Medical physics*, 35(5):2124–2136.

[De Man and Basu, 2002] De Man, B. and Basu, S. (2002). Distance-driven projection and backprojection. In *Nuclear Science Symposium Conference Record, 2002 IEEE*, volume 3, pages 1477–1480. IEEE.

[De Man and Basu, 2004] De Man, B. and Basu, S. (2004). Distance-driven projection and backprojection in three dimensions. *Physics in Medicine & Biology*, 49(11):2463.

[De Molina et al., 2014] De Molina, C., Pascau, J., Desco, M., and Abella, M. (2014). Calibration of a c-arm x-ray system for its use in tomography. In *XIII Mediterranean Conference on Medical and Biological Engineering and Computing 2013*, pages 245–248. Springer.

[de Molina et al., 2018] de Molina, C., Serrano, E., Garcia-Blas, J., Carretero, J., Desco, M., and Abella, M. (2018). Gpu-accelerated iterative reconstruction for limited-data tomography in cbct systems. *BMC bioinformatics*, 19(1):171.

[Debatin et al., 2013] Debatin, D. S., Stsepankou, D., and Hesser, J. (2013). Ct reconstruction from fewviews by higher order adaptive weighted total variation minimization. In *Proceedings of International Meeting on Fully Three-Dimensional Image Reconstruction in Radiology and Nuclear Medicine (Lake Tahoe, CA, 2013)*.

[Diederich and Wormanns, 2004] Diederich, S. and Wormanns, D. (2004). Impact of low-dose ct on lung cancer screening. *Lung Cancer*, 45:S13–S19.

[Dobbins and McAdams, 2009] Dobbins, J. T. and McAdams, H. P. (2009). Chest tomosynthesis: technical principles and clinical update. *European journal of radiology*, 72(2):244–251.

[Dobbins III and Godfrey, 2003] Dobbins III, J. T. and Godfrey, D. J. (2003). Digital x-ray tomosynthesis: current state of the art and clinical potential. *Physics in medicine & biology*, 48(19):R65.

[Duan et al., 2009] Duan, X., Zhang, L., Xing, Y., Chen, Z., and Cheng, J. (2009). Few-view projection reconstruction with an iterative reconstruction-reprojection algorithm and tv constraint. *IEEE Transactions on Nuclear Science*, 56(3):1377–1382.

[Erdogan and Fessler, 1999] Erdogan, H. and Fessler, J. A. (1999). Ordered subsets algorithms for transmission tomography. *Physics in Medicine & Biology*, 44(11):2835.

[Ergun et al., 1990] Ergun, D. L., Mistretta, C. A., Brown, D. E., Bystrianyk, R., Sze, W., Kelcz, F., and Naidich, D. (1990). Single-exposure dual-energy computed radiography: improved detection and processing. *Radiology*, 174(1):243–249.

[Feldkamp et al., 1984] Feldkamp, L., Davis, L., and Kress, J. (1984). Practical cone-beam algorithm. *JOSA A*, 1(6):612–619.

[Fessler, 2008] Fessler, J. A. (2008). Image reconstruction: Algorithms and analysis. *Under preparation*.

[Fessler and Tutorial, 2006] Fessler, J. A. and Tutorial, I. (2006). Iterative methods for image reconstruction. In *IEEE International Symposium on Biomedical Imaging Tutorial, Arlington Virginia*.

[Fiacco and McCormick, 1990] Fiacco, A. V. and McCormick, G. P. (1990). *Nonlinear programming: sequential unconstrained minimization techniques*, volume 4. Siam.

[Fletcher, 2013] Fletcher, R. (2013). *Practical methods of optimization.* John Wiley & Sons.

[Frikel, 2013] Frikel, J. (2013). Sparse regularization in limited angle tomography. *Applied and Computational Harmonic Analysis*, 34(1):117–141.

[Gallio et al., 2015] Gallio, E., Rampado, O., Gianaria, E., Bianchi, S. D., and Ropolo, R. (2015). A gpu simulation tool for training and optimisation in 2d digital x-ray imaging. *PloS one*, 10(11):e0141497.

[Gaullier et al., 2009] Gaullier, G., Charbonnier, P., and Heitz, F. (2009). Introducing shape priors in object-based tomographic reconstruction. In *Image Processing (ICIP), 2009 16th IEEE International Conference on*, pages 1077–1080. IEEE.

[Goldstein and Osher, 2009] Goldstein, T. and Osher, S. (2009). The split bregman method for l1-regularized problems. *SIAM journal on imaging sciences*, 2(2):323–343.

[Gomi et al., 2012] Gomi, T., Nakajima, M., Fujiwara, H., Takeda, T., Saito, K., Umeda, T., and Sakaguchi, K. (2012). Comparison between chest digital tomosynthesis and ct as a screening method to detect artificial pulmonary nodules: a phantom study. *The British journal of radiology*, 85(1017):e622–e629.

[Gopinath et al., 2012] Gopinath, A., Xu, G., Ress, D., Oktem, O., Subramaniam, S., and Bajaj, C. (2012). Shape-based regularization of electron tomographic reconstruction. *IEEE transactions on medical imaging*, 31(12):2241–2252.

[Grills et al., 2008] Grills, I. S., Hugo, G., Kestin, L. L., Galerani, A. P., Chao, K. K., Wloch, J., and Yan, D. (2008). Image-guided radiotherapy via daily online cone-beam ct substantially reduces margin requirements for stereotactic lung radiotherapy. *International Journal of Radiation Oncology* Biology* Physics*, 70(4):1045–1056.

[Hansen and O'Leary, 1993] Hansen, P. C. and O'Leary, D. P. (1993). The use of the l-curve in the regularization of discrete ill-posed problems. *SIAM Journal on Scientific Computing*, 14(6):1487–1503.

[Heinzerling and Schlindwein, 1980] Heinzerling, J. and Schlindwein, M. (1980). Non-linear techniques in multi-spectral x-ray imaging. *IEEE Transactions on Nuclear Science*, 27(2):961–968.

[Hsieh, 2003] Hsieh, J. (2003). Computed tomography: Principles, design, artifacts, and recent advances (bellingham, wa: Spie optical engineering press). *Google Scholar*.

[Hsieh et al., 2009] Hsieh, J. et al. (2009). Computed tomography: principles, design, artifacts, and recent advances. SPIE Bellingham, WA.

[Huang et al., 2011] Huang, J., Ma, J., Liu, N., Zhang, H., Bian, Z., Feng, Y., Feng, Q., and Chen, W. (2011). Sparse angular ct reconstruction using non-local means based iterative-correction pocs. *Computers in Biology and Medicine*, 41(4):195–205.

[Hubbell and Seltzer, 1995] Hubbell, J. H. and Seltzer, S. M. (1995). Tables of x-ray mass attenuation coefficients and mass energy-absorption coefficients 1 kev to 20 mev for elements z= 1 to 92 and 48 additional substances of dosimetric interest. Technical report, National Inst. of Standards and Technology-PL, Gaithersburg, MD (United States). Ionizing Radiation Div.

[Jaffray et al., 2002] Jaffray, D. A., Siewerdsen, J. H., Wong, J. W., and Martinez, A. A. (2002). Flat-panel cone-beam computed tomography for image-guided radiation therapy. *International Journal of Radiation OncologyâĂć BiologyâĂć Physics*, 53(5):1337–1349.

[Jan, 2005] Jan, J. (2005). *Medical image processing, reconstruction and restoration: concepts and methods*. CRC Press.

[Johnston et al., 2008] Johnston, S. M., Johnson, G. A., and Badea, C. T. (2008). Geometric calibration for a dual tube/detector micro-ct system. *Medical physics*, 35(5):1820–1829.

[Kak and Slaney, 1988] Kak, A. C. and Slaney, M. (1988). *Principles of computerized tomographic imaging*. IEEE press.

[Kazantsev et al., 2014] Kazantsev, D., Lionheart, W. R., Withers, P. J., and Lee, P. D. (2014). Multimodal image reconstruction using supplementary structural information in total variation regularization. *Sensing and imaging*, 15(1):97.

[Korner et al., 2007] Korner, M., Weber, C. H., Wirth, S., Pfeifer, K.-J., Reiser, M. F., and Treitl, M. (2007). Advances in digital radiography: physical principles and system overview. *Radiographics*, 27(3):675–686.

[Kuhlman et al., 2006] Kuhlman, J. E., Collins, J., Brooks, G. N., Yandow, D. R., and Broderick, L. S. (2006). Dual-energy subtraction chest radiography: what to look for beyond calcified nodules. *Radiographics*, 26(1):79–92.

[Lagarias et al., 1998] Lagarias, J. C., Reeds, J. A., Wright, M. H., and Wright, P. E. (1998). Convergence properties of the nelder–mead simplex method in low dimensions. *SIAM Journal on optimization*, 9(1):112–147.

[Lange et al., 1984] Lange, K., Carson, R., et al. (1984). Em reconstruction algorithms for emission and transmission tomography. *J Comput Assist Tomogr*, 8(2):306–16.

[LaRoque et al., 2008] LaRoque, S. J., Sidky, E. Y., and Pan, X. (2008). Accurate image reconstruction from few-view and limited-angle data in diffraction tomography. *JOSA A*, 25(7):1772–1782.

[Lehmann et al., 1981] Lehmann, L., Alvarez, R., Macovski, A., Brody, W., Pelc, N., Riederer, S. J., and Hall, A. (1981). Generalized image combinations in dual kvp digital radiography. *Medical physics*, 8(5):659–667.

[Lewitt, 1992] Lewitt, R. M. (1992). Alternatives to voxels for image representation in iterative reconstruction algorithms. *Physics in Medicine & Biology*, 37(3):705.

[Machida et al., 2010] Machida, H., Yuhara, T., Mori, T., Ueno, E., Moribe, Y., and Sabol, J. M. (2010). Optimizing parameters for flat-panel detector digital tomosynthesis. *Radiographics*, 30(2):549–562.

[Maier et al., 2013] Maier, A., Hofmann, H. G., Berger, M., Fischer, P., Schwemmer, C., Wu, H., Müller, K., Hornegger, J., Choi, J.-H., Riess, C., et al. (2013). ConradâĂŤa software framework for cone-beam imaging in radiology. *Medical physics*, 40(11).

[Mainprize et al., 2006] Mainprize, J. G., Bloomquist, A. K., Kempston, M. P., and Yaffe, M. J. (2006). Resolution at oblique incidence angles of a flat panel imager for breast tomosynthesis. *Medical physics*, 33(9):3159–3164.

[Matenine et al., 2015] Matenine, D., Goussard, Y., and Després, P. (2015). Gpu-accelerated regularized iterative reconstruction for few-view cone beam ct. *Medical physics*, 42(4):1505–1517.

[Molina Gómez et al., 2012] Molina Gómez, C. d. et al. (2012). *Corrección del artefacto de endurecimiento de haz (beam hardening) para imágenes obtenidas con tomógrafo de rayos X de pequeños animales*. PhD thesis.

[Nocedal and Wright, 2006] Nocedal, J. and Wright, S. J. (2006). *Sequential quadratic programming*. Springer.

[Noo et al., 2000] Noo, F., Clackdoyle, R., Mennessier, C., White, T. A., and Roney, T. J. (2000). Analytic method based on identification of ellipse parameters for scanner calibration in cone-beam tomography. *Physics in Medicine & Biology*, 45(11):3489.

[Osher et al., 2005] Osher, S., Burger, M., Goldfarb, D., Xu, J., and Yin, W. (2005). An iterative regularization method for total variation-based image restoration. *Multiscale Modeling & Simulation*, 4(2):460–489.

[Otsu, 1979] Otsu, N. (1979). A threshold selection method from gray-level histograms. *IEEE transactions on systems, man, and cybernetics*, 9(1):62–66.

[Park et al., 2007] Park, J. M., Franken Jr, E. A., Garg, M., Fajardo, L. L., and Niklason, L. T. (2007). Breast tomosynthesis: present considerations and future applications. *Radiographics*, 27(suppl_1):S231–S240.

[Rantala et al., 2006] Rantala, M., Vanska, S., Jarvenpaa, S., Kalke, M., Lassas, M., Moberg, J., and Siltanen, S. (2006). Wavelet-based reconstruction for limited-angle x-ray tomography. *IEEE transactions on medical imaging*, 25(2):210–217.

[Rockmore and Macovski, 1977] Rockmore, A. and Macovski, A. (1977). A maximum likelihood approach to transmission image reconstruction from projections. *IEEE Transactions on Nuclear Science*, 24(3):1929–1935.

[Rosety-Rodríguez et al., 2013] Rosety-Rodríguez, M., Fornieles, G., Rosety, I., Díaz, A. J., Rosety, M. A., Camacho-Molina, A., Rodriguez-Pareja, A., Tejerina, A., Alvero-Cruz, J. R., and Ordonez, F. J. (2013). Central obesity measurements predict metabolic syndrome in a retrospective cohort study of postmenopausal women. *Nutricion hospitalaria*, 28(6).

[Rougee et al., 1993] Rougee, A., Picard, C. L., Trousset, Y. L., and Ponchut, C. (1993). Geometrical calibration for 3d x-ray imaging. In *Medical Imaging 1993: Image Capture, Formatting, and Display*, volume 1897, pages 161–170. International Society for Optics and Photonics.

[Rudin et al., 1992] Rudin, L. I., Osher, S., and Fatemi, E. (1992). Nonlinear total variation based noise removal algorithms. *Physica D: nonlinear phenomena*, 60(1-4):259–268.

[Sawyer, 2007] Sawyer, A. (2007). *Bone densitometry in growing patients*. Springer Science & Business Media.

[Schafer et al., 2012] Schafer, S., W Stayman, J., Zbijewski, W., Schmidgunst, C., Kleinszig, G., and H Siewerdsen, J. (2012). Antiscatter grids in mobile c-arm cone-beam ct: Effect on image quality and dose. *Medical physics*, 39(1):153–159.

[Servent, 2013] Servent, J. C. (2013). *Using state-of-the-art inverse problem techniques to develop reconstruction methods for fluorescence diffuse optical*. PhD thesis, Universidad Carlos III de Madrid.

[Setzer et al., 2010] Setzer, S., Steidl, G., and Teuber, T. (2010). Deblurring poissonian images by split bregman techniques. *Journal of Visual Communication and Image Representation*, 21(3):193–199.

[Shkumat et al., 2007] Shkumat, N., Siewerdsen, J., Dhanantwari, A., Williams, D., Richard, S., Paul, N., Yorkston, J., and Van Metter, R. (2007). Optimization of image acquisition techniques for dual-energy imaging of the chest. *Medical physics*, 34(10):3904–3915.

[Sidky et al., 2006] Sidky, E. Y., Kao, C.-M., and Pan, X. (2006). Accurate image reconstruction from few-views and limited-angle data in divergent-beam ct. *Journal of X-ray Science and Technology*, 14(2):119–139.

[Sievänen et al., 1993] Sievänen, H., Kannus, P., Oja, P., and Vuori, I. (1993). Precision of dual energy x-ray absorptiometry in the upper extremities. *Bone and mineral*, 20(3):235–243.

[Siewerdsen et al., 2005] Siewerdsen, J., Moseley, D., Burch, S., Bisland, S., Bogaards, A., Wilson, B., and Jaffray, D. (2005). Volume ct with a flat-panel detector on a mobile, isocentric c-arm: Pre-clinical investigation in guidance of minimally invasive surgery. *Medical physics*, 32(1):241–254.

[Siewerdsen et al., 2004] Siewerdsen, J., Waese, A., Moseley, D., Richard, S., and Jaffray, D. (2004). Spektr: A computational tool for x-ray spectral analysis and imaging system optimization. *Medical physics*, 31(11):3057–3067.

[Sisniega Crespo, 2013] Sisniega Crespo, A. (2013). Contributions to the improvement of image quality in cbct and cbμct and application in the development of a cbμct system.

[Snyder et al., 1993] Snyder, D. L., Hammoud, A. M., and White, R. L. (1993). Image recovery from data acquired with a charge-coupled-device camera. *JOSA A*, 10(5):1014–1023.

[Snyder et al., 1995] Snyder, D. L., Helstrom, C. W., Lanterman, A. D., Faisal, M., and White, R. L. (1995). Compensation for readout noise in ccd images. *JOSA A*, 12(2):272–283.

[Tanabe, 1971] Tanabe, K. (1971). Projection method for solving a singular system of linear equations and its applications. *Numerische Mathematik*, 17(3):203–214.

[Van der Vorst, 1992] Van der Vorst, H. A. (1992). Bi-cgstab: A fast and smoothly converging variant of bi-cg for the solution of nonsymmetric linear systems. *SIAM Journal on scientific and Statistical Computing*, 13(2):631–644.

[Vanderplaats and Moses, 1973] Vanderplaats, G. N. and Moses, F. (1973). Structural optimization by methods of feasible directions. *Computers & Structures*, 3(4):739–755.

[Vaquero et al., 2008] Vaquero, J. J., Redondo, S., Lage, E., Abella, M., Sisniega, A., Tapias, G., Montenegro, M. S., and Desco, M. (2008). Assessment of a new high-performance small-animal x-ray tomograph. *IEEE transactions on nuclear science*, 55(3):898–905.

[Velikina et al., 2007] Velikina, J., Leng, S., and Chen, G.-H. (2007). Limited view angle tomographic image reconstruction via total variation minimization. In *Medical Imaging 2007: Physics of Medical Imaging*, volume 6510, page 651020. International Society for Optics and Photonics.

[Venter, 2010] Venter, G. (2010). Review of optimization techniques. *Encyclopedia of aerospace engineering*.

[Vikgren et al., 2008] Vikgren, J., Zachrisson, S., Svalkvist, A., Johnsson, A. A., Boijsen, M., Flinck, A., Kheddache, S., and BaÌŁth, M. (2008). Comparison of chest tomosynthesis and chest radiography for detection of pulmonary nodules: human observer study of clinical cases. *Radiology*, 249(3):1034–1041.

[Wang et al., 2014] Wang, D., He, J., Qiao, H., Song, X., Fan, Y., and Li, D. (2014). High-performance fluorescence molecular tomography through shape-based reconstruction using spherical harmonics parameterization. *PloS one*, 9(4):e94317.

[Whiting et al., 2001] Whiting, B., Montagnino, L., and Politte, D. (2001). Modeling x-ray computed tomography sinograms.

[Whiting, 2002] Whiting, B. R. (2002). Signal statistics in x-ray computed tomography. In *Medical Imaging 2002: Physics of Medical Imaging*, volume 4682, pages 53–61. International Society for Optics and Photonics.

[Whiting et al., 2006] Whiting, B. R., Massoumzadeh, P., Earl, O. A., O'Sullivan, J. A., Snyder, D. L., and Williamson, J. F. (2006). Properties of preprocessed sinogram data in x-ray computed tomography. *Medical physics*, 33(9):3290–3303.

[Yang et al., 2007] Yang, W. T., Carkaci, S., Chen, L., Lai, C.-J., Sahin, A., Whitman, G. J., and Shaw, C. C. (2007). Dedicated cone-beam breast ct: Feasibility study with surgical mastectomy specimens. *American Journal of Roentgenology*, 189(6):1312–1315.

[Yao et al., 2015] Yao, J., Shaw, C., Lai, C., Rong, J., Wang, J., and Liu, W. (2015). Cone beam ct for determining breast cancer margin: an initial experience and its comparison with mammography and specimen radiograph. *International journal of clinical and experimental medicine*, 8(9):15206.

[Yin et al., 2008] Yin, W., Osher, S., Goldfarb, D., and Darbon, J. (2008). Bregman iterative algorithms for l1-minimization with applications to compressed sensing: Siam journal on imaging sciences, 1 (1), 143–168. *CrossRef Google Scholar*.

[Zhang et al., 2016] Zhang, H., Wang, L., Yan, B., Li, L., Cai, A., and Hu, G. (2016). Constrained total generalized p-variation minimization for few-view x-ray computed tomography image reconstruction. *PloS one*, 11(2):e0149899.

[Zhang and Navab, 2003] Zhang, X. and Navab, N. (2003). Coded visual markers for tracking and camera calibration in mobile computing systems. US Patent App. 10/262,693.

[Zhao et al., 2014] Zhao, J., Xu, Y., and Dong, F. (2014). An lq–lp optimization framework for image reconstruction of electrical resistance tomography. *Measurement Science and Technology*, 25(12):125402.